UNIVERSITY OF CALIFORNIA, SAN DIEGO

Nonequilibrium phase transitions to collective behavior in stochastic spatially extended systems

A dissertation submitted in partial satisfaction of the
requirements for the degree
Doctor of Philosophy

in

Chemistry and Physics

by

Kevin B. Wood

Committee in charge:

Professor Katja Lindenberg, Chair
Professor Henry Abarbanel, Co-Chair
Professor Daniel Arovas
Professor Andrew McCammon
Professor Jeffrey Rabin

2007

The dissertation of Kevin B. Wood is approved, and it is acceptable in quality and form for publication on microfilm:

_____

_____

_____

_____
Co-Chair

_____
Chair

University of California, San Diego

2007

For Jimmy, who would certainly get a good laugh from this all. . .

Anyone who attempts to generate random
numbers by deterministic means is, of
course, living in a state of sin.
—John von Neumann

TABLE OF CONTENTS

LIST OF FIGURES

LIST OF TABLES

ACKNOWLEDGEMENTS

I am afforded here–in a space that could easily grow to many times the length of the following dissertation–the opportunity to thank those who made this work possible. There is a part of me that wishes such dedications were not so common, that I might appeal to something beyond cliche for the mentors, friends, and family supporting me. Nevertheless, I hope the following all-too-brief sentiments might echo some of the originality I have found in their love and guidance; even where I fail to equal in sentence form the sincerity of their support, I hope the readers–particularly those mentioned here– can sense the authenticity beneath my words.

I will start first where this thesis began, with Katja–my advisor and mentor–who guided me at every scientific turn with an amiable mix of rigor, freedom, tremendous insight, and unwavering encouragement. I cannot speak statistically to the typical advisor-student relationship, but I am happily convinced without mathematical justification of my good fortunes in finding her and developing such an enriching friendship. Science can be taught in many forms, and I am grateful that I learned it to be an honest and delightful pursuit, where the lines between mentor and family can be blurred in the most joyous of ways.

Secondly, I want to thank Henry Abarbanel, who several years ago shepherded my transfer from Neuroscience to Physics. While my faulty memory precludes a perfect quotation, I remember vividly the sentiment Henry shared with me when I walked, without clear scientific focus, into his office to ask for guidance over four years ago. A truly good scientist, he intimated, must sometimes focus his/her efforts towards the younger student, that the next generation might benefit from today's successes. Certainly, he did so for me by offering invaluable advice–both scientific and personal–during my transfer and throughout my graduate career; for such kindness and support I will always be indebted.

I want to also thank Christian van den Broeck, who stands among the most creative and unique thinkers I have known. I am thankful for our sometimes brief, but always fruitful, collaborations, both in San Diego and abroad, and this dissertation bears his fingerprints throughout. In a similar spirit, I want to express gratitude to Ryoichi Kawai, a frequent collaborator whose careful judgment and wealth of computational

knowledge proved invaluable throughout the evolution of my thesis projects. Despite the distance separating us for much of the last few years, Christian and Ryoichi provided me with steadfast support and an inspiring combination of measured reasoning and liberal thought.

In addition, I want to thank two other collaborators, Javier Buceta and Francisco Cao. Javi offered me my first taste of life in Katja's lab by opening my eyes to many aspects of stochastic and noise-induced phenomena when I originally joined the group. I continue to appreciate the time and wisdom he shared with me, and I am grateful for our numerous collaborations. In particular, Javi played a major role in conceiving the problem analyzed in Chapter 8 as well as in guiding the project through numerous ups and downs. Similarly, Fran provided much needed insight into several projects–most notably, he recognized the necessity of a large K expansion for exploring relaxational dynamics–and this realization resurrected previously unsuccessful attempts at a Gaussian ansatz and multiscale treatment of the time-dependent problem presented in Chapter 9. I am grateful for the efforts of both Javi and Fran and thankful for both the opportunities their guidance afforded me as well as the results which followed.

It is safe to say that I have been blessed with a wealth of intelligent, kind, and generous collaborators. Without these individuals, the work presented in my dissertation would doubtlessly be hollow and uninteresting, and I hope the reader will always keep in mind the efforts of those who collectively marshaled this work to its current state.

In addition, I would like to thank the two people who first introduced me to laboratory science as an undergraduate: Scott Britz-Cunningham and Sidney Altman. Scott served as my first research advisor and chaperoned me through an exciting summer of molecular biology and, well, a great deal of broken glassware. Without his patience and encouragement, I am certain my life would not have taken the fortunate turn towards pure science. Sidney Altman served as my second research advisor and remains, to this day, a source of inspiration, not merely for his scientific accomplishments, but also because of his generosity and the faith he showed in me.

Finally, I want to thank all of the members of my committee, whose time, flexibility, and optimism are greatly appreciated. In particular, Dr. Rabin offered a number of suggestions to improve the text, and his careful reading is much appreciated.

Before I move on to a few personal acknowledgments, let me first give more

credit where it is due. First, it should be noted that this work was partially supported by the National Science Foundation under Grant No. PHY-0354937.

Chapter 2 contains material which appears, in part, in K. Wood, C. Van den Broeck, R. Kawai, and K. Lindenberg, Phys. Rev. Lett. **96**, 145701 (2006); K. Wood, C. Van den Broeck, R. Kawai, and K. Lindenberg, Phys. Rev. E **74**, 031113 (2006); and K. Wood, C. Van den Broeck, R. Kawai, and K. Lindenberg, in preparation (2007).

Chapter 3 contains material which appears, in part, in K. Wood, C. Van den Broeck, R. Kawai, and K. Lindenberg, Phys. Rev. Lett. **96**, 145701 (2006); K. Wood, C. Van den Broeck, R. Kawai, and K. Lindenberg, Phys. Rev. E **74**, 031113 (2006); and K. Wood, C. Van den Broeck, R. Kawai, and K. Lindenberg, in preparation (2007).

Chapter 4 contains material which appears, in part, in K. Wood, C. Van den Broeck, R. Kawai, and K. Lindenberg, Phys. Rev. E 75 , 041107 (2007).

Chapter 5 contains material which appears, in part, in K. Wood, C. Van den Broeck, R. Kawai, and K. Lindenberg, in preparation (2007).

Chapter 7 contains material which appears, in part, in K. Wood, J. Buceta, and K. Lindenberg, Phys. Rev. E **73**, 022101 (2006).

Chapter 8 contains material which appears, in part, in J. Buceta, K. Wood, and K. Lindenberg, Phys. Rev. E **73**, 042101 (2006).

Chapter 9 contains material which appears, in part, in F. Cao, K. Wood, and K. Lindenberg, cond-mat/0702524 (submitted for publication) (2007).

I cannot, of course, conclude any acknowledgments section without recognizing my friends and family, who have always played an integral role in my life.

While there are simply too many friends to mention in detail, I want to give special thanks to Jon Shlens, my roommate for the past 5 years. Jon once told me that his friends, while diverse, share one commonality: they each possess an attribute that he admires. In the same spirit, I can say that if one's admirable qualities define a friend, Jon is perhaps the best I have ever known. With humility, compassion, and thoughtfulness, he served as a daily role model to me, and no doubt to many others. When it comes to living this life commendably, well, some people simply do it better than the rest of us. I am honored to call Jon a friend and beyond grateful for the impact he continues to have on my scientific and personal life.

I want to also thank my older (but still young) sister, Carmen, and my younger

(but getting old) brother, Kris. Both Kris and Sis are passionate workers, and I have always found it inspiring to watch them match their considerable talents with ardent and unwavering discipline. It is a genuine pleasure to look both ways in time and find myself looking up.

I owe probably the greatest debt of gratitude to my parents, whose unshakable support serves as the cornerstone of any successes I might encounter. While their ever-present encouragement makes even towering ambitions seem attainable, my parents provide–more importantly–a gentle love to accompany any failures along the way.

Finally, I want to offer my love and thanks to Sarah, whose optimism affords a buoyant foundation for all that lies ahead. . .

VITA

1979	Born, Georgetown, Kentucky
2001	B. S., Centre College
2007	Ph. D., University of California, San Diego

PUBLICATIONS

Wood, K., Buceta, J., Lindenberg, K., *Comprehensive Study of Pattern Formation in Relaxational Systems*, Phys. Rev. E, **73**, 022101, 2006.

Buceta, J., **Wood, K.**, Lindenberg, K., *Noise-induced Oscillatory Behavior in Field-Dependent Relaxational Dynamics*, Phys. Rev. E, **73**, 042101, 2006.

Wood, K., Van den Broeck C., Kawai R., Lindenberg, K., *The Universality of Synchrony: Critical Behavior in a Discrete Model of Stochastic Phase Coupled Oscillators*, Phys. Rev. Lett., **96**, 145701, 2006.

Wood, K., Van den Broeck C., Kawai R., Lindenberg, K., *Critical Behavior and Synchronization of Discrete Stochastic Phase Coupled Oscillators*, Phys. Rev. E, **74**, 031113, 2006.

Wood, K., Van den Broeck C., Kawai R., Lindenberg, K., *Effects of Disorder on Synchronization of Discrete Phase-Coupled Oscillators*, Phys. Rev. E, **75**, 041107, 2007.

Wood, K., Van den Broeck C., Kawai R., Lindenberg, K., *Fluctuation Theorem for the Effusion of an Ideal Gas with Momentum Transfer*, Phys. Rev. E, **75**, 061116, 2007.

Cao, F. J., **Wood, K.**, Lindenberg, K., *Noise-induced phase transitions in field-dependent relaxational dynamics: The Gaussian ansatz*, cond-mat/0702524 (submitted for publication), 2007.

Wood, K., Van den Broeck C., Kawai R., Lindenberg, K., *Continuous and discontinuous phase transitions in Stochastic Phase Coupled Oscillators*, (in preparation, to be submitted shortly), 2007.

ABSTRACT OF THE DISSERTATION

Nonequilibrium phase transitions to collective behavior in stochastic spatially extended systems

by

Kevin B. Wood
Doctor of Philosophy in Chemistry and Physics

University of California San Diego, 2007

Professor Katja Lindenberg, Chair
Professor Henry Abarbanel, Co-Chair

We explore nonequilibrium collective behavior in large, spatially extended stochastic systems. In Part I, we present a model of discrete, active, noisy phase oscillators sufficiently simple to be characterized in complete detail in a host of diverse settings. In Chapter 2, we introduce the model and detail its utility for the study of both continuous and discontinuous phase transitions to macroscopic oscillations. In Chapter 3 we analyze a locally coupled version of the model undergoing a continuous transition and provide strong evidence that the inherently nonequilibrium system shows qualitative and quantitative characteristics of a known class of equilibrium phase transitions. Chapter 4 offers an analysis of the discrete model in the face of quenched transition rate disorder, where synchronization still occurs and depends on the degree of disorder in the population. The final chapter of Part I, Chapter 5, details the microscopic underpinnings of synchronization above threshold, including the counterintuitive relationship between time-averaged frequency and the mean field oscillations. The second part of the dissertation begins with an introduction to generic relaxational models with field-dependent kinetic coefficients, highlighting in particular the role of this class of models in the study of noise-induced phase transitions. Using these systems as prototypical models of noise-induced phenomena in spatially extended systems, we offer a comprehensive study of static pattern formation in Chapter 7, while Chapter 8 provides a numerical study of

coherent oscillatory dynamics induced purely by noise. Finally, Chapter 9 details an analytical framework for studying the dynamics of these systems which is capable of approximately describing both static and time-dependent phases associated with the nonequilibrium transitions in these relaxational models.

1

Introduction

Natural systems occurring in physical, chemical, biological, and social settings often consist of a large number of interacting components. Whether composed of, for example, reactive molecules, living cells, entire organisms or magnetic dipoles, these populations serve as a battleground of sorts for the competition between the dynamics of individual entities and the large scale cooperation favored in many cases by the nature of their mutual interactions. This competition underlies a host of equilibrium phase transitions where, generically speaking, independent thermal fluctuations oppose energetically favorable macroscopic order–for example, the aligning of magnetic dipoles. But such an interplay exists far beyond the traditional jurisdiction of equilibrium statistical physics and applies to intrinsically nonequilibrium scenarios where cooperative phenomena may be time-dependent and significantly more complex than their equilibrium counterparts. In fact, while diverse mathematical abstractions facilitate the study of these systems, it is worthwhile to recognize a single intuitively appealing and readily recognizable commonality: the emergence of macroscopic order which arises despite the potentially disruptive tendencies of a system's many degrees of freedom.

In this dissertation, we examine the large-scale cooperative behaviors–specifically, the phase transitions–which occur in two fundamentally non-equilibrium settings. Part I contains a detailed analysis of the nonequilibrium phase transition to synchronous oscillations in large populations of stochastic, discrete, active phase oscillators. By introducing a novel and simple phenomenological model of a generic noisy oscillator, we provide evidence of the striking similarities between the emergence of time-dependent

synchronous cooperativity in these systems and a class of equilibrium phase transitions. In addition, our model offers a conceptually simple paradigm for exploring a number of collective phenomena observed in these ubiquitous systems, including synchronization in the face of quenched disorder and the existence of both continuous and discontinuous phase transitions. Part II describes the ordering role of fluctuations in a prototypical class of nonequilibrium relaxational models. In particular, we explore via extensive numerical simulations and mean field analysis the counterintuitive role of noise in these spatially-extended systems, highlighting especially its constructive role in static spatial pattern formation as well as time-dependent oscillatory dynamics. In addition, we provide an analytical framework capable of approximately describing the dynamics of both the static and time-dependent phases associated to the phase transitions in question. While differing in focus, Parts I and II are unified by the shared theme of macroscopic cooperation in large stochastic systems and, taken together, provide detailed characterization of such ordering phenomena in two general and physically relevant nonequilibrium settings.

Part I

Synchronization

2

Macroscopic Synchronization: A New Approach

2.1 Introduction

The role of dissipative structures and self-organization in systems far from equilibrium in the description of real and observable physical phenomena has been undisputed since the experiments with the Belusov-Zhabotinsky reactions in the early 1960's. The breaking of time translational symmetry has since become a central and typical theme in the analysis of nonlinear nonequilibrium systems. It is somewhat surprising that in the later studies of spatially distributed systems, most of the interest shifted to pattern forming instabilities, and little attention was devoted to the phenomenon of bulk oscillation and the required spatial frequency and phase synchronization, especially in view of the intense interest generated in the scientific and even broader community by the emergence of phase synchronization in populations of globally coupled phase oscillators [1], with the synchronous firing of fireflies being one of the most visible and spectacular examples. Because intrinsically oscillating units with slightly different eigenfrequencies underlie the macroscopic behavior of an extensive range of biological, chemical, and physical systems, a great deal of literature has focused on the mathematical principles governing the competition between individual oscillatory tendencies and synchronous cooperation [2, 3, 4]. Many studies have focused on globally coupled units, leading to a mature understanding

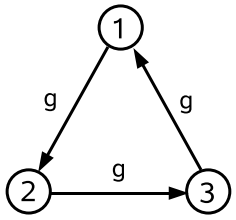

Figure 2.1: Single three state unit with generic transition rates g. From [9, 10, 11].

of the mean field behavior of several models, most notably the paradigmatic Kuramoto oscillator. However, even the simplest models of coupled oscillators are typically based on a large system of coupled nonlinear differential equations which become analytically intractable and computationally extravagant following the inclusion of stochastic fluctuations. For practical purposes, many models are rendered unmanageable for even a modest number of units, and numerical studies of large, noisy systems are practically nonexistent. As a result, the description of emergent synchrony has largely been limited to small-scale and/or globally-coupled deterministic systems [5, 6], despite the fact that the dynamics of the physical systems in question likely reflect a combination of stochasticity and large system sizes with finite range forces.

Here we introduce a far more tractable model consisting of *discrete* phase-coupled oscillators. The simple structure renders it amenable to an extensive range of studies, including detailed numerical analysis of the continuous phase transition (Chapter 3), in addition to providing a conceptually appealing approach to some synchronization phenomena in disordered populations (Chapter 4) and systems above threshold (Chapter 5). Furthermore, the phase discretization reduces many of the typical mean field problems to matrix algebra, eliminating the need for a continuous functional space in describing large populations of oscillators.

The use of such minimal models is common in statistical physics, where microscopic details can often be disregarded in favor of phenomenological macroscopic variables. As Landau theory [7] reminds us, macroscopically observable changes (those that occur on length and time scales encompassing a magnificently large number of degrees of freedom) occur without reference to microscopic specifics. In a sense, the distinguishing features of even highly diverse systems become irrelevant for the description of coop-

erative behavior at the level of a phase transition; instead, the underlying statistical similarities give rise to classes of universal behavior whose members differ greatly at the microscopic level. In the spirit of this universality, simple toy models have been devised in hopes of capturing the essential qualitative features of phase transitions without concern for the microscopic structure of the problem. With this in mind, we construct the simplest model that exhibits global phase synchrony and contains the physical ingredients listed above, namely, stochastic variation within individual units and roughly time-periodic dynamics. The simplicity of the model allows for relatively fast numerical simulation and thus an extensive description of the phase transition in question (Chapter 3), as well as a simplified analytical approach to a number of problems in the mean field limit (Chapters 4, 5).

2.2 The Model

Our starting point is a three-state unit [8] governed by transition rates g, as shown in Fig. 2.1. We interpret the state designation as a generalized (discrete) phase, and the transitions between states, which we construct to be unidirectional, as a phase change and thus an oscillation of sorts. The probability of going from the current state i to state $i+1$ in an infinitesimal time dt is gdt, with $i = 1, 2, 3$. We take $i + 1 = 1$ when $i = 3$; note that the unit steps unidirectionally among states in a semi-periodic, probabilistic fashion, e.g. $1 \to 2 \to 3 \to 1...$, where here the integers designate the state. For a single unit, g is simply a constant that sets the oscillator's intrinsic frequency; for many units coupled together, we will allow g for a given oscillator to depend on the states of the other oscillators to which it is coupled. The choice of coupling, specified below, is not unique, and different choices allow the model to be used in a host of settings [9, 10, 11], as we shall see.

For a single unit we write the linear evolution equation

$$\frac{\partial}{\partial t}P(t) = MP(t) \tag{2.1}$$

where

$$P(t) = \begin{pmatrix} P_1(t) \\ P_2(t) \\ P_3(t) \end{pmatrix}, \tag{2.2}$$

$P_i(t)$ is the probability of being in state i at time t, and

$$M = \begin{pmatrix} -g & 0 & g \\ g & -g & 0 \\ 0 & g & -g \end{pmatrix}. \tag{2.3}$$

The system clearly reaches a steady state for $P_1^* = P_2^* = P_3^* = 1/3$. The transitions $1 \to 2$, $2 \to 3$, $3 \to 1$ occur with a rough periodicity determined by g. The time evolution of our simple model thus qualitatively resembles that of the discretized phase of a generic noisy oscillator.

We are interested in the behavior that emerges when a large number of individual units are coupled to one another by allowing the transition probability of a given unit to depend on the states of the unit's nearest neighbors in the spatial grid. The phase at a given site is compared with those of its neighbors, and the phase of the given site is adjusted so as to facilitate phase coherence. The expectation is to capture the physical nature of synchronization. It is further expected that within certain restrictions (e.g., the coupling must surely be nonlinear), the specific nature of the coupling is not important so long as we ultimately observe a transition to global synchrony at some finite value of the coupling parameter. To say this another way, we are concerned with observable macroscopic behavior without particular regard to the microscopic underpinnings, so long as these underpinnings produce the appropriate long wavelength features (e.g. a continuous or discontinuous phase transition in a large population). We settle upon a particular exponential form below, Eq. (2.4), though we allow some flexibility by leaving unspecified the real coefficients (U, V, W) which completely determine the phase-coupling. Our choice of an exponential function is in no way unique, though it does maintain a superficial similarity to the Arrhenius prototype transition rate constant from chemical kinetics and, much more importantly, it provides a sufficiently strong nonlinearity to induce large-scale cooperativity. As we shall see, linear stability analysis confirms the existence of a Hopf bifurcation in the mean field limit

for appropriate choices (U, V, W). Particularly striking is the fact that (U, V, W) can be chosen to give either supercritical or subcritical Hopf bifurcations, indicating that the model can be used to study both continuous and discontinuous phase transitions. This is reminiscent of several recent generalized models of phase synchronization [12, 13, 14], though it appears here in a much more transparent analytical and numerical context. In what follows, we make specific choices (U, V, W) for particular studies–and there are both benefits and drawbacks to each–but the flexibility renders the model highly useful for uncovering several aspects of synchronization [9, 10, 11].

More concretely, we specify that each unit may transition to the state ahead or remain in its current state in a manner that depends on the states of the other units to which it is coupled. For unit μ, which we take to be in state i, we choose the transition rate to state $i+1$ as follows:

$$g_i = g \exp\left[\frac{a(UN_{i+1} + VN_{i-1} + WN_i)}{n}\right], \tag{2.4}$$

where $i = 1, 2, 3$ (and again $i+1 = 1$ when $i = 3$), a is the adjustable coupling parameter, g is the transition rate parameter, n is the number of oscillators to which the unit in question is coupled, and N_k is the number of units among the n that are in state k. Each unit may transition to the state ahead or remain in its current state, and the propensity for such a change depends on the states of its nearest neighbors. For now, we focus on globally coupled arrays ($n = N-1$), though we later include the study of locally coupled oscillators as well (Chapter 3).

For a population of $N \to \infty$ identical units in the mean field (globally coupled) version of this model we can replace $N_k/(N-1)$ with the probability P_k, thereby arriving at a nonlinear equation for the mean field probability,

$$\partial \boldsymbol{P}(t)/\partial t = M[\boldsymbol{P}(t)]\boldsymbol{P}(t), \tag{2.5}$$

with

$$M[\boldsymbol{P}(t)] = \begin{pmatrix} -g_1 & 0 & g_3 \\ g_1 & -g_2 & 0 \\ 0 & g_2 & -g_3 \end{pmatrix}. \tag{2.6}$$

Normalization allows us to eliminate $P_3(t)$ and obtain a closed set of equations for $P_1(t)$ and $P_2(t)$. We can then linearize about the fixed point $(P_1^*, P_2^*) = (1/3, 1/3)$, yielding a

Jacobian $A(a, g, U, V, W)$ with a set of complex conjugate eigenvalues which determine the stability of this asynchronous state. Specifically, we find that

$$\lambda_{\pm} = C\big(-9 + 3a\Delta_{UW} \pm i\sqrt{3}(3 + a(U + W - 2V))\big), \tag{2.7}$$

where $C \equiv ge^{a(U+V+W)/3}/6$ is a nonzero constant for all finite U, V, and W and we introduce the abbreviation $\Delta_{mn} \equiv m - n$. The eigenvalues cross the imaginary axis at

$$a_c = 3/\Delta_{UW}, \tag{2.8}$$

yielding

$$\lambda^*_{\pm} = \pm i\omega(U, V, W) \tag{2.9}$$

with

$$\omega(U, V, W) \equiv g\sqrt{3}(e^{a(U+V+W)/\Delta_{UW}})\frac{\Delta_{UV}}{\Delta_{UW}}. \tag{2.10}$$

For $\Delta_{UW} \neq 0$ and $\omega(U, V, W) \neq 0$ (that is, $\Delta_{UV} \neq 0$ and $g \neq 0$), a_c represents a Hopf bifurcation point, indicating the emergence of macroscopic oscillations indicative of synchronization. Furthermore, we require that $\Delta_{UW} > 0$ to ensure the bifurcation happens at a positive value of a. We note that in later chapters we will use $(U, V, W) = (1, -1, 0)$, yielding $a_c = 3$ and $\omega = 2g\sqrt{3}$, and $(U, V, W) = (1, 0, -1)$, yielding $a_c = 1.5$ and $\omega = g\sqrt{3}/2$. In addition, we stress that while a range of models may prove useful for exploring the phase transition behavior near threshold (see, for example, [9, 10] and Chapter 3), only models with $W = 0$ provide physically appealing characteristics far above threshold (see, for example, [11] and Chapter 4). Specifically, only for $W = 0$ does the frequency of a perfectly synchronized set of oscillators maintain a nonzero, finite value (g) as coupling is increased. Below we explore in more detail the nature of the Hopf bifurcation associated with the class of models described by the permitted values (U, V, W). We will come back to these points in later chapters.

2.3 First and Second Order Transitions to Synchrony

In the mean field limit, the order of the phase transition to synchrony is closely tied to the nature of the Hopf bifurcation. Specifically, a subcritical Hopf bifurcation corresponds to a discontinuous, first-order phase transition, while a supercritical Hopf

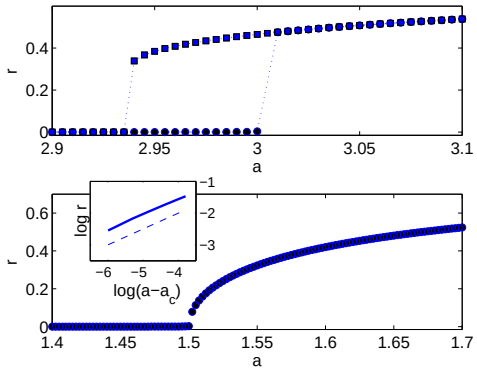

Figure 2.2: In a single population of globally coupled oscillators, two physically distinct Hopf transitions can be observed depending on the choices of U, V, and W. The top panel represents $(U, V, W) = (1, -2, 0)$ and clearly shows characteristics of a first order transition, including hysteresis. Squares represent solutions starting from ordered (mostly synchronized) initial conditions, while circles represent solutions starting from disordered (random) initial conditions. The bottom panel represents $(U, V, W) = (2, -1, 0)$ and displays a second order transition with critical exponent β given by the classical value $1/2$. The inset shows a log-log plot near the critical point. For comparison, a dashed line with a slope of $1/2$ is shown along with the order parameter curve (solid line) to verify this scaling relation. The order parameter r is a measure of synchronization and is defined in Eq. 3.4.

bifurcation indicates a continuous, second-order transition. As such, we place special emphasis in this manuscript on the sign of l_1, the first Lyapunov coefficient, which provides information on the nature of the Hopf bifurcation and, by extension, on the order of the phase transition.

In general, l_1 can be calculated using the projection technique given in [15], which relies on a multivariate Taylor expansion of the vector field describing the dynamics in question about an equilibrium point. For a general n-dimensional dynamical system $\dot{x} = f(x, \epsilon)$ with an equilibrium point $x = x^H$ undergoing a Hopf bifurcation at parameter value $\epsilon = \epsilon^H$, l_1 is given by [15]

$$\begin{aligned} l_1 = \frac{1}{2\omega}\mathrm{Re}(&\langle p, C(q,q,\bar{q})\rangle - 2\langle p, B(q, A^{-1}B(q,\bar{q}))\rangle \\ &+ \langle p, B\left(\bar{q}, (2i\omega I - A)^{-1}B(q,q)\right)\rangle), \end{aligned} \tag{2.11}$$

where $\langle ., . \rangle$ is the typical complex scalar product, I is the identity matrix, and p and q are right and left eigenvectors of the Jacobian $A = \frac{\partial f}{\partial x}\big|_{x=x^H}$ given by

$$\begin{aligned} Aq &= i\omega q \\ A^T p &= -i\omega p. \end{aligned} \tag{2.12}$$

Furthermore, p is chosen so that $\langle p, q\rangle = 1$, and $B(x, y)$ and $C(x, y, z)$ are multilinear, n-dimensional vector functions corresponding to the lowest order nonlinear coefficients in the Taylor expansion of the vector field. That is,

$$\begin{aligned} B(u,v) &= \sum_{j,k=1}^{n} \frac{\partial^2 f(\psi, \epsilon^H)}{\partial\psi_j \partial\psi_k}\bigg|_{\psi=x^H} u_j v_k, \\ C(u,v,w) &= \sum_{j,k,l=1}^{n} \frac{\partial^3 f(\psi, \epsilon^H)}{\partial\psi_j \partial\psi_k \partial\psi_l}\bigg|_{\psi=x^H} u_j v_k w_l, \end{aligned} \tag{2.13}$$

with x^H indicating the equilibrium point of the vector field around which we expand and ϵ^H the bifurcation parameter, ϵ, evaluated at the bifurcation point.

2.3.1 First and Second Order Transitions in a Single Population of Identical Oscillators

For the case of a single population of oscillators described by Eqs. (2.4,2.6), l_1 can be analytically calculated using the technique outlined above. Specifically, we set

$g = 1$ (without loss of generality) and consider the equilibrium point $\boldsymbol{P} = (1/3, 1/3)$ at $\epsilon^H \equiv a_c$ and find q and p to be

$$\begin{aligned} q &= \left(-\frac{1}{2} + \frac{i\sqrt{3}}{2}, 1 \right), \\ p &= \left(\frac{i - \sqrt{3}}{3i + \sqrt{3}}, \frac{2i}{3i + \sqrt{3}} \right), \end{aligned} \tag{2.14}$$

independent of U, V, and W. Then, calculating the multivariable functions $B(u, v)$ and $C(u, v, w)$ with Eq. (2.13) and using ω as defined in Eq. (2.10) along with Eqs. (2.11,2.14), we find after simplification that

$$l_1 = -\frac{9\sqrt{3}(U + V - 2W)}{4\Delta_{UW}}. \tag{2.15}$$

As a result, the nature of the Hopf bifurcation depends on the choices U, V, and W. Specifically, if we assume $U > V$, we have

$$\begin{aligned} l_1 &< 0 \text{ for } W < \frac{U + V}{2}; \\ l_1 &> 0 \text{ for } W > \frac{U + V}{2}. \end{aligned} \tag{2.16}$$

A similar result holds for $U < V$, but we shall here restrict ourselves to the intuitively reasonable models positing $U \geq 0$ and $V \leq 0$; that is, the oscillators one state ahead of the one in question can only increase (or not affect) the transition rate and those behind can only decrease (or not affect) the transition rate. To verify these predictions, we show numerical solutions to the mean field equations in Fig. 2.2; the top panel represents an example in the subcritical regime ($(U, V, W) = (1, -2, 0)$) while the bottom panel shows an example in the supercritical regime ($(U, V, W) = (2, -1, 0)$). The order parameter r shown in the figures is defined and discussed in later chapters (see Eq. (3.4)), but for now it is sufficient to consider it a measure of phase synchronzation. A clear distinction can be made in the neighborhood of the critical point. We also note that the continuous transition is characterized by the classical mean field exponent $\beta = 1/2$, which quantifies the scaling of the order parameter near criticality. We return to these ideas in later chapters.

We further observe that the choice $(U, V, W) = (1, 0, -1)$ leads to $l_1 = -27\sqrt{3}/4 \approx -11.69$, indicating a supercritical Hopf bifurcation and rendering the model applicable

to studies of continuous phase transitions [9, 10]. With universality in mind, we stress that any choice of parameters (U, V, W) yielding a supercritical bifurcation should show similar critical behavior. On the other hand, the choice $(U, V, W) = (1, -1, 0)$, while physically appealing above threshold (see Chapter 4), falls at a singular point separating the subcritical and supercritical cases ($l_1 = 0$). The flexibility inherent in the choice of coefficients U, V, and W speaks to the richness of our generic three-state oscillator and highlights its utility in studying synchronization in both supercritical (see [9, 10]) and subcritical regimes.

2.4 Discussion

We have developed a simple, discrete model for stochastic phase-coupled oscillators. While providing certain analytical and numerical simplification to the study of macroscopic synchronization in large populations of oscillators, our model retains sufficient flexibility to capture complexities seen in a number of more complicated models as well as experimental settings. At the same time, the simplifications arising from incorporating noise and periodicity in a discrete model allow us to characterize synchronization in a detailed and transparent way, often providing results unattainable in more complicated models. Most notably, our model provides flexibility to study both continuous phase transitions [9, 10] as well as discontinuous transitions exhibiting hysteresis, a characterstic seen in detailed theoretical models of, e.g., coupled Josephson junctions [14] but only observed in significantly more complex coupled oscillator models [12, 13, 14]. In what follows we study the model in three settings, yielding insight into the universal behavior of the continuous transition to synchrony (Chapter 3), the complexity of synchronization in disordered arrays of oscillators (Chapter 4), and finally, the nature of phase synchronization above threshold (Chapter 5).

Acknowledgements

Chapter 2 contains material which appears, in part, in K. Wood, C. Van den Broeck, R. Kawai, and K. Lindenberg, Phys. Rev. Lett. **96**, 145701 (2006); K. Wood, C. Van den Broeck, R. Kawai, and K. Lindenberg, Phys. Rev. E **74**, 031113 (2006); and

K. Wood, C. Van den Broeck, R. Kawai, and K. Lindenberg, in preparation (2007).

References

[1] S. H. Strogatz, *Nonlinear Dynamics and Chaos* (Westview Press, 1994).

[2] A. T. Winfree, J. Theor. Biol. **16**, 15 (1967).

[3] Y. Kuramoto, *Chemical Oscillations, Waves, and Turbulence* (Springer, Berlin, 1984).

[4] S. H. Strogatz, Physica D **143**, 1 (2000).

[5] H.Hong, H. Park, M. Choi, Phys. Rev. E **71**, 054204 (2004).

[6] A. Pikovsky, M. Rosenblum, J. Kurths, *Synchronization: A Universal Concept in Nonlinear Science* (Cambridge University Press, Cambridge, 2001).

[7] N. Goldenfeld, *Lectures on Phase Transitions and the Renormalization Group* (Westview Press, 1992).

[8] T. Prager, B. Naundorf, and L. Schimansky-Geier, Physica A **325**, 176 (2003).

[9] K. Wood, C. Van den Broeck, R. Kawai, and K. Lindenberg, Phys. Rev. Lett. **96**, 145701 (2006).

[10] K. Wood, C. Van den Broeck, R. Kawai, and K. Lindenberg, Phys. Rev. E **74**, 031113 (2006).

[11] K. Wood, C. Van den Broeck, R. Kawai, and K. Lindenberg, Phys. Rev. E **75**, 041107 (2007).

[12] H. Daido. Physica D **91**, 24 (1996).

[13] F. Giannuzzi, D. Marinazzo, G. Nardulli, M. Pellicoro, and S. Stramaglia. Phys. Rev. E **75**, 051104 (2007).

[14] G. Filatrella, N. F. Pedersen, and K. Wiesenfeld. Phys. Rev. E **75**, 017201 (2007).

[15] Y.A. Kuznetsov, *Elements of Applied Bifurcation Theory*, 2nd ed. (Springer, New York, 1998).

3

The Universality of Synchrony

3.1 Introduction

As mentioned in Chapter 2, the breaking of time translational symmetry has been a critical theme in the analysis of nonlinear nonequilibrium systems for several decades, in no small part because it represents the prototype of a nonequilibrium phase transition. While the theory of equilibrium critical phenomena is founded on the notion of universality in large systems exhibiting most typically a change in symmetry of static macroscopic phases, the emergence of cooperative synchronization in collections of active coupled oscillators represents the breaking of an inherently time-dependent symmetry. Specifically, in the nonsynchronous phase, many individual oscillators exhibit essentially independent behavior, meaning that macroscopic properties of the system (e.g. the amplitude of collective oscillations) remain invariant under excursions along the time axis. On the other hand, when the intrinsic interactions within the system are chosen to facilitate long-wavelength cooperativity–that is, when macroscopic oscillations emerge in a collection of oscillators–the thermodynamic-like synchronized phase exhibits a periodicity that breaks the completely free translational symmetry in time apparent for independent oscillators. Thus, even as large populations of interacting, oscillating entities appear in a range of natural and physical settings [1, 2, 3, 4], such systems also provide an illustrative and fundamental example of symmetry-breaking in an inherently non-equilibrium setting.

Because of the widespread occurence of large scale synchronization phenomena

in nature, it is not surprising that many studies have centered on populations of coupled units. However, relatively little concerted effort has focused on the locally coupled regime [5, 6, 7], where the analogy with an equilibrium phase transition is most clear. In fact, models of locally coupled oscillators typically involve a prohibitively large collection of interdependent nonlinear differential equations, thus preventing any extensive characterization of the phase transition to phase synchrony. As discussed in Chapter 2, the description of emergent synchrony has largely been limited to small-scale and/or globally-coupled deterministic systems [8, 9], although the relevant physical systems are perhaps better treated in a stochastic framework incorporating finite range forces. Two recent studies by Risler et al. [10, 11] represent notable exceptions to this trend. Using an elegant renormalization group approach, they provide analytical evidence that identical locally-coupled noisy oscillators belong to the XY universality class–at least in terms of classical critical exponents and upper and lower critical dimensions–and we here provide the first empirical verification, numerical or otherwise, of their predictions.

Inspired by Landau theory [12], or perhaps more appropriately, by the wealth of physical insight gleaned from toy models built upon the premise that macroscopically observable changes occur without reference to microscopic specifics, we examine the model introduced in Chapter 2 as a model of a nonequilibrium phase transition. To be explicit, we have constructed the simplest model that exhibits large scale phase synchrony and contains the physical ingredients most relevant to the macroscopic phenomena, namely, stochastic variation within individual units and local coupling. Our interest here is twofold. First, we provide the first numerical evidence that noisy, coupled oscillators–which constitute a highly ubiquitous physical system–undergo a phase transition marked by signatures of a specific class of phase transitions. Second, we show that this fundamentally nonequilibrium phase transition shows a host of similarities with equilibrium phase transitions, including diverging correlation lengths, large scale fluctuations near criticality, and critical scaling as given by classical exponents β and ν.

The organization of the chapter is as follows. In Sec. 3.2 we briefly review the model of a single unit as well as the coupling scheme between units. Section 3.3 presents numerical results confirming linear stability analysis in the mean field limit, and Sec. 3.4 contains the finite-size scaling analysis that unveils the critical behavior of the locally-coupled model. We conclude with a summary in Sec 3.5.

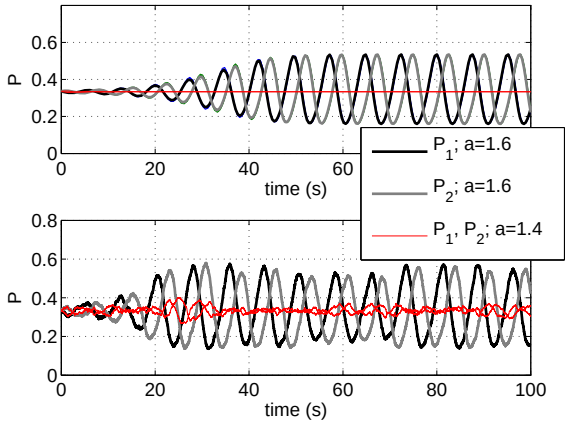

Figure 3.1: Simulations with 5000 globally coupled units (bottom panel) agree well with the numerical solution of the mean field equations (top panel). As predicted by linearization, a Hopf bifurcation occurs near $a = 1.5$.

3.2 Three State Model

We begin with the three state model Eq. (2.1) introduced in Chapter 2. As before, we allow transitions between states in a unidirectional, probabilistic manner, hence preserving the analogy with the discretized phase of a generic active oscillator. We specify here that each unit may transition to the state ahead or remain in its current state depending on the states of its nearest neighbors. For unit μ, which we take to be in state i, we choose the transition rate to state $i+1$ as follows:

$$g_i = g \exp\left[\frac{a(N_{i+1} - N_i)}{n}\right], \tag{3.1}$$

where a is the coupling parameter,N_k is the number of nearest neighbors in state k, and n is the total number of units to which the unit in question is coupled. For locally coupled oscillators, which will be the focus of this chapter, $n = 2d$ in d dimensions. The transition rate is thus determined by the number of nearest neighbors of unit μ that are one state ahead and in the same state as unit μ. We note that this corresponds to $(U, V, W) = (1, 0, -1)$ in Eq. (2.4), a choice which guarantees a supercritical Hopf bifurcation in the mean field limit. Specifically, for globally coupled units ($n = N - 1$)

in the $N \to \infty$ limit, Eq. (2.8) yields

$$a_c = 3/\Delta_{UW} = 3/2. \tag{3.2}$$

The nature of the Hopf bifurcation is given by Eq. (2.15)

$$l_1 = -\frac{9\sqrt{3}(U+V-2W)}{4\Delta_{UW}} = -27\sqrt{3}/4. \tag{3.3}$$

Table I shows the explicit transition rates in one dimension. While these rates are somewhat distorted by their assumed independence of the number of nearest neighbors in state $i-1$ (e.g. in one dimension the transition rate from state i to state $i+1$ is the same if both nearest neighbors are in state $i-1$ and if one is in state i and the other in $i+1$), the form does lead to a continuous phase transition. We settle on our choice (3.1) for two reasons. First, and most importantly, it provides the requisite supercritical Hopf bifurcation indicative of a continuous transition. Second, the phase transition we seek occurs for a relatively small value of the coupling constant a, and therefore numerical simulations can be run with larger time steps. We note in passing that we have also explored coupling with a sigmoidal function, which shows similar qualitative behavior (that is, a supercritical Hopf bifurcation in the mean field limit and an apparent synchronization transition in locally coupled simulations), but this again occurs for a higher value of a, making simulations more cumbersome. We stress again that universality suggests that such microscopic details should not substantially alter the qualitative picture of the phase transition as long as the coupling is sufficiently nonlinear and favors synchronization via a continuous bifurcation.

3.3 Mean-Field Theory Simulations

The globally coupled regime has been used to verify analytically the presence of a supercritical Hopf bifurcation as a eclipses a_c, indicating that the model breaks time translational symmetry via a continous bifurcation for the coupling chosen, Eq. (3.1). These predictions can be verified by numerically solving the mean field Eqs. (2.5, 2.6) with coupling given by Eq. (3.1) in the mean field ($N_j/(N-1) \to P_j$) limit. In addition, these solutions agree well with direct lattice simulations of the multiple unit model

Table 3.1: Transition rates in one dimension.

Neighbors	Transition Rate
$i-1,\, i-1$	g
$i-1,\, i$	$g\exp(-a/2)$
$i-1,\, i+1$	$g\exp(a/2)$
$i,\, i-1$	$g\exp(-a/2)$
$i,\, i$	$g\exp(-a)$
$i,\, i+1$	g
$i+1,\, i-1$	$g\exp(a/2)$
$i+1,\, i$	g
$i+1,\, i+1$	$g\exp(a)$

characterized by Eq. (3.1) if we consider all-to-all coupling rather than merely nearest-neighbor coupling (Fig. 3.1). As such, the mean field equations accurately capture the behavior of the nearest neighbor model in the high (spatial) dimensional limit. We note that, similar to the examples shown in Chapter 2, our choice of coupling produces a bifurcation which is clearly continuous and lacks hysteresis effects.

We have shown through both analytical arguments and numerical simulations that our model indeed produces the desired macroscopic synchronization in the mean field limit. In what follows, we characterize the breakdown of the mean field description as spatial dimension is decreased, and characterize the phase transitions observed with nearest-neighbor coupling.

3.4 Critical behavior of the locally coupled model

We now follow with a study of the locally coupled model. We perform simulations in continuous time on d-dimensional cubic lattices of various sizes. For all simulations, we implement periodic boundary conditions. Time steps dt are taken to be 10 to 100 times smaller than the fastest possible local average transition rate, that is, $dt \ll e^{-a}$ (we set $g = 1$ in our simulations). This estimate is actually quite conservative, particularly because the fastest possible transition corresponds to a single unit in state i

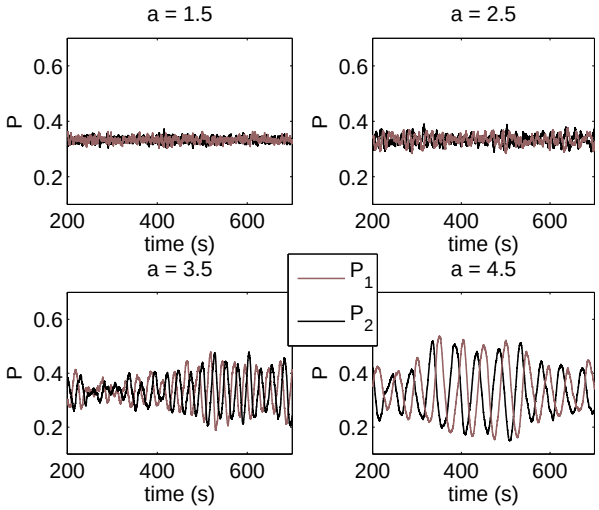

Figure 3.2: Absence of synchronization in $2D$. Top left: $a = 1.5$. Top right: $a = 2.5$. Bottom left: $a = 3.5$. Bottom right: $a = 4.5$. $L = 100$ for all plots. Even for very large values of the coupling, highly synchronous oscillatory behavior is not present. As discussed in the text and shown in the next figure, the intermittent oscillations apparent for high values of a result from finite size effects.

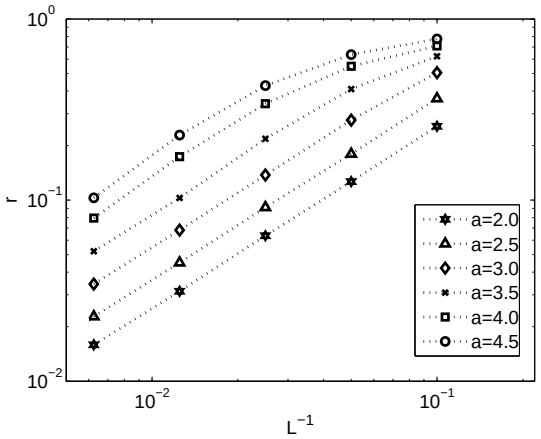

Figure 3.3: Log-log plot of r vs L^{-1} for $d = 2$. The order parameter r tends to 0 as system size increases, verifying the absence of a transition in two dimensions. Even for large values of the coupling, synchronous oscillations die away in the limit of infinite system size.

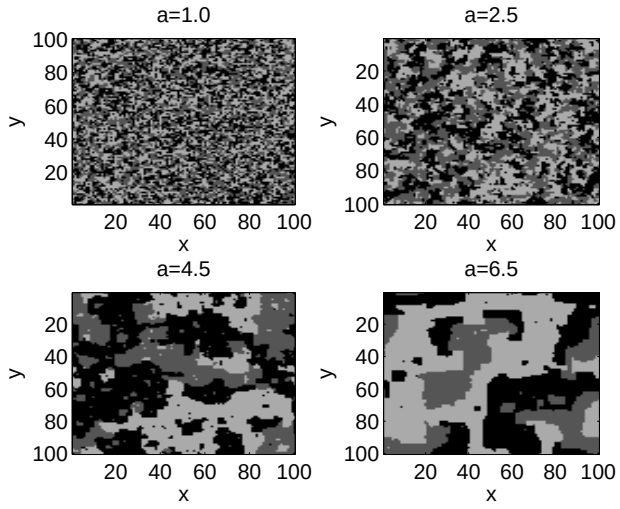

Figure 3.4: Snapshots of the system in $d = 2$ are shown for $a = 1$, $a = 2.5$, $a = 4.5$, and $a = 6.5$. Upon close inspection, one can discern vortex-like structures, particularly for the higher values of a. The three shades of gray represent units in the three possible states.

with all $2d$ nearest neighbors in state $i+1$, a scenario which certainly does not dominate the macroscopic dynamics. We have ascertained that differences between these simulations and others run at much smaller time steps (500 to 1000 times smaller than e^{-a}) are very small. All simulations were run until an apparent steady state was reached. Furthermore, we start all simulations from random initial conditions, and we calculate statistics based on 100 independent trials. Although the simplicity of the model allows for efficient numerical simulation, our results nevertheless represent a modest computational achievement; simulations required approximately 5 weeks on a 28-node dual processor cluster.

To characterize the emergence of phase synchrony, we introduce the order parameter [8]

$$r = \langle R \rangle, \qquad R \equiv \frac{1}{N} \left| \sum_{j=1}^{N} e^{i\phi_j} \right|. \tag{3.4}$$

Here ϕ is a discrete phase, taken to be $2\pi(k-1)/3$ for state $k \in \{1, 2, 3\}$ at site j. The brackets represent an average over time in the steady state and an average over all independent trials. A nonzero value of r in the thermodynamic limit signifies the

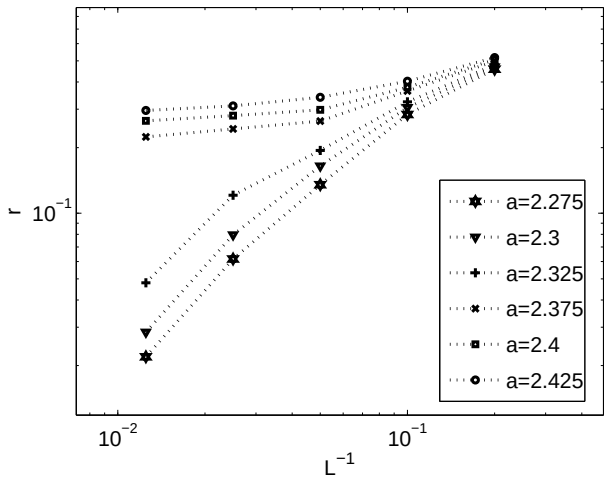

Figure 3.5: Log-log plots of r vs L^{-1} for $d = 3$. For $a > a_c$, the order parameter r approaches a finite value, even as the system size increases indefinitely. For $a < a_c$, r approaches zero in the thermodynamic limit.

presence of synchrony. We also make use of the corresponding generalized susceptibility

$$\chi = L^d[\langle R^2\rangle - \langle R\rangle^2]. \tag{3.5}$$

We begin by considering the model in two spatial dimensions. Here, as shown in Fig. 3.2, we do not see the emergence of global oscillatory behavior. Instead, we observe intermittent oscillations (for very large values of a) that decrease drastically with increasing system size. In fact, as depicted in Fig. 3.3, r approaches zero in the thermodynamic limit, even for very large values of a. We conclude that the phase transition to synchrony cannot occur for $d = 2$. Interestingly, snapshots of the system reveal increased spatial clustering as a is increased as well as the presence of defect structures, perhaps indicative of Kosterlitz-Thouless-type phenomena (Fig. 3.4) [12]. Furthermore, the local clustering of synchronous activity invites comparisons with the localized excitations seen in arrays of localized laser oscillators [13].

In contrast to the $d = 2$ case, which serves as the lower critical dimension, a clear thermodynamic-like phase transition occurs in three spatial dimensions. We see the emergence of global oscillatory behavior, which persists in the limit of large system size, as a increases past a critical value a_c (Figs. 3.5 and 3.6). This is consistent with

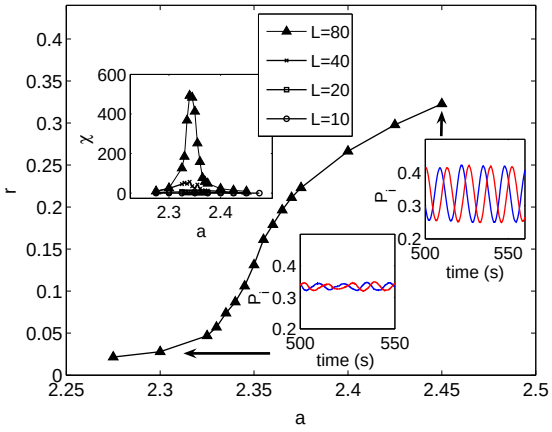

Figure 3.6: Onset of synchronization in $d = 3$. Global oscillatory behavior emerges as a is increased beyond a_c, as indicated by the increasing value of r. The system size is $L = 80$. Upper left inset: Fluctuations peak near the critical point, giving an estimation of $a_c = 2.345 \pm 0.005$. Right insets: P_1 and P_2 undergo smooth temporal oscillations for large a (upper right), while a lower value of a decreases temporal coherence (lower left).

the predictions of the mean field theory. For $a < a_c$, r approaches zero as system size is increased, and a disordered phase persists in the thermodynamic limit. As expected, for $a > a_c$ the steady state dynamics of P_1 and P_2 exhibit smooth temporal oscillations (see the lower insets in Fig. 3.6) similar to the mean field case beyond the Hopf bifurcation point. In addition, Fig. 3.6 shows the behavior of the order parameter as a is increased for the largest system studied ($L = 80$); the upper left inset shows the peak in χ at $a = 2.345 \pm 0.005$, thus providing an estimate of the critical point a_c where fluctuations are largest. Strictly speaking, we must extrapolate this peak to obtain a result in the limit of infinite system size, but we see no change in the value a_c at which the peak occurs as system size is increased beyond $L = 40$, indicating that finite size effects are small in the determination of a_c in systems beyond this size. At any rate, such finite size effects are within the range of our estimation. We tried to apply the Binder cumulant crossing method [14] for determining a_c more precisely, but residual finite size effects and statistical uncertainties in the data prevent us from determining the crossing point with more precision than that stated above. In any case, we are only interested in determining the critical point with sufficient accuracy to determine the universality class

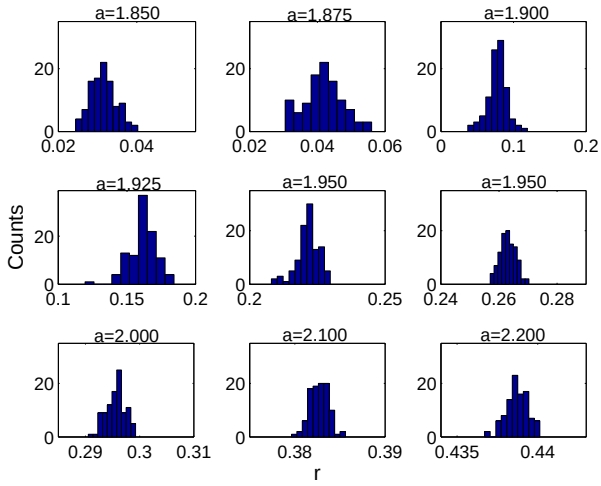

Figure 3.7: Lack of multistability in $d = 4$: Histograms over all independent trials show only single peaks of varying widths, consistent with the expectations for a second order phase transition.

of the transition. For this, as we show below, our current estimation suffices in three dimensions as well as in higher dimensions. In addition, we note that the transition to synchrony appears to be a smooth, second order phase transition. To rule out potential multistability (and thus a discontinuous first order transition), we show histograms of r for $d = 4$ given over all independent trials in Fig. 3.7. The histograms show no evidence whatsoever of multiple peaks beyond the statistical fluctuations expected for the relatively small sample size, and thus we can safely rule out a discontinuous transition, in agreement with the findings of the mean field analysis. Similarly peaked histograms are found in $d = 3$ (less sharply peaked but distinctly unimodal) and $d = 5$ (more sharply peaked).

To further characterize this transition, we use a systematic finite size scaling analysis. We start by assuming the standard form for r in a finite system,

$$r = L^{-\frac{\beta}{\nu}} F[(a - a_c)L^{\frac{1}{\nu}}], \tag{3.6}$$

where $F(x)$ is a scaling function that approaches a constant as $x \to 0$. This ansatz suggests that near the critical point we should plot $rL^{\frac{\beta}{\nu}}$ vs. $(\frac{a}{a_c} - 1)L^{\frac{1}{\nu}}$, and data from

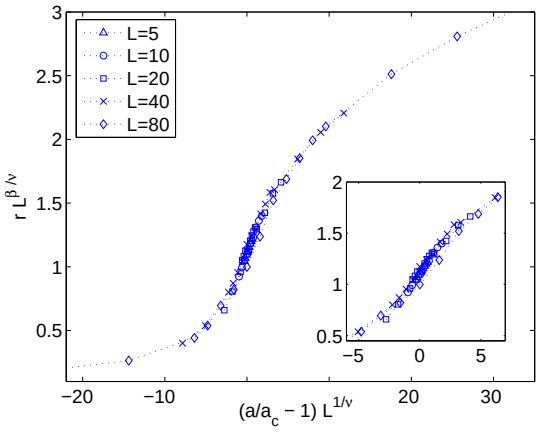

Figure 3.8: Exponents in $d = 3$: Data collapse of $rL^{\frac{\beta}{\nu}}$ vs $(a/a_c - 1)L^{\frac{1}{\nu}}$. With $a_c = 2.345$, we show the data collapse using the theoretical XY exponents in $3D$. The collapse is excellent, suggesting that the model is in the XY universality class. The insets show a closer view near the critical point.

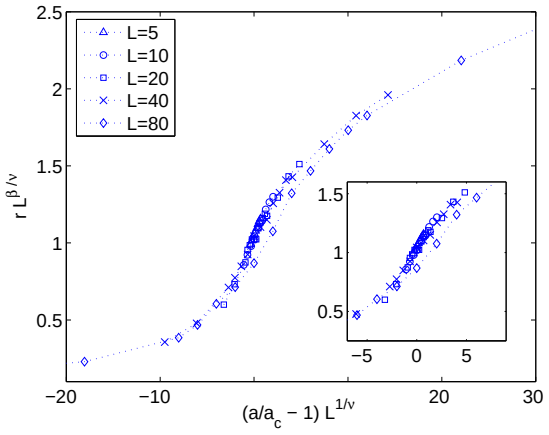

Figure 3.9: Exponents in $d = 3$. Data collapse of $rL^{\frac{\beta}{\nu}}$ vs $(a/a_c - 1)L^{\frac{1}{\nu}}$. With $a_c = 2.345$, we show the data collapse using theoretical Ising 3D exponents. The collapse is reasonably good, but still poor compared with that seen with exponents from the XY class. Insets show a closer view near the critical point.

different system sizes should collapse onto a single curve. To test our numerical data against different universality classes we choose the appropriate critical exponents for each, recognizing that there are variations in the reported values of these exponents. For the XY universality class we use the exponents reported in [15] ($\beta = 0.34$ and $\nu = 0.66$). For the Ising exponents we use those given in [16] ($\beta = 0.31$ and $\nu = 0.64$). In Fig. 3.8, we see quite convincingly a collapse when exponents from the XY class are used. For comparison, we also show the data collapse when 3D Ising exponents are used (Fig. 3.9). Our data suggests that the model falls within the XY universality class, though the very small differences between XY and Ising exponents makes it impossible to entirely rule out Ising-like behavior. We should point out that while some reported values of the Ising critical exponents differ from the XY values by more than those used above, others differ by less (see [17] for an exhaustive collection of estimates). Note that this scaling procedure was attempted for many values a_c within the stated range of accuracy. In all cases where a distinction could be made, the XY exponents provided a better collapse than the corresponding Ising exponents.

To complete the analogy with the equilibrium phase transition, we explore spatial correlations in $d = 3$. Specifically, we calculate $C(l)$, the spatial correlation function, given by

$$C(l) = \langle \sum_{j=1}^{N} \sum_{n=1}^{3} \exp(i\phi_j) \exp(-i\phi_{j+l_n}) \rangle - r^2. \tag{3.7}$$

Here ϕ_j again indicates the discrete phase of the oscillator at site j, and l_n denotes the Cartesian components in the x, y, and z directions at distance l from site j. The correlation function depends only on this distance. As seen in Fig. 3.10, correlations develop for values of a near the critical point, while this correlation is absent away from a_c. The functional form of $C(l)$ as a approaches a_c is similar to that seen in equilibrium transitions. Indeed, the lower inset is at the critical point ($a = 2.345$) and explicitly shows power law decay of the correlation function. The upper inset is far from the critical point ($a = 1.8$) and shows exponential decay.

In four spatial dimensions we also see a transition to synchrony characterized by large fluctuations at the critical point. Here we estimate the transition coupling to be $a_c = 1.900 \pm 0.025$ by again considering the peak in χ (see Figs. 3.11 and 3.12).

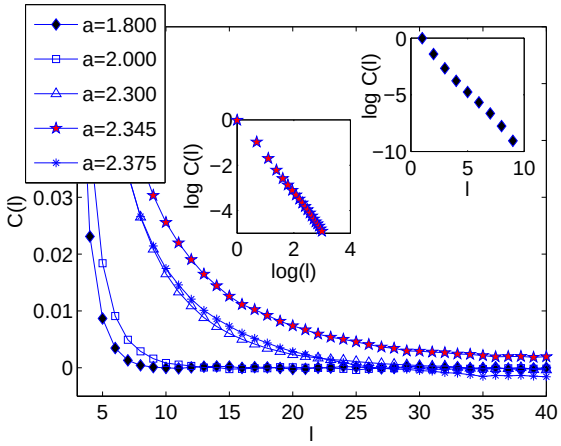

Figure 3.10: Spatial correlations in $d = 3$. As a approaches the critical value a_c, evidence of long range correlations develops, indicative of a diverging correlation length at the critical point. The lower inset shows the power law decay of the correlation function at the critical point, while the upper inset shows that the correlation function decays exponentially far from the critical point.

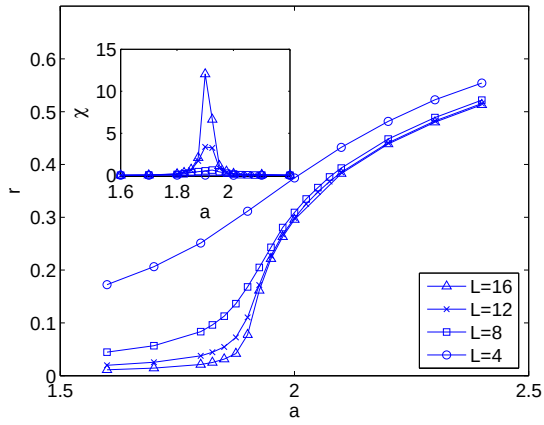

Figure 3.11: Transition in $d = 4$: The behavior of the order parameter near the transition point is shown for various system sizes. The inset shows the generalized susceptibility, χ, which peaks at $a = 1.900 \pm 0.025$, giving an estimation of a_c.

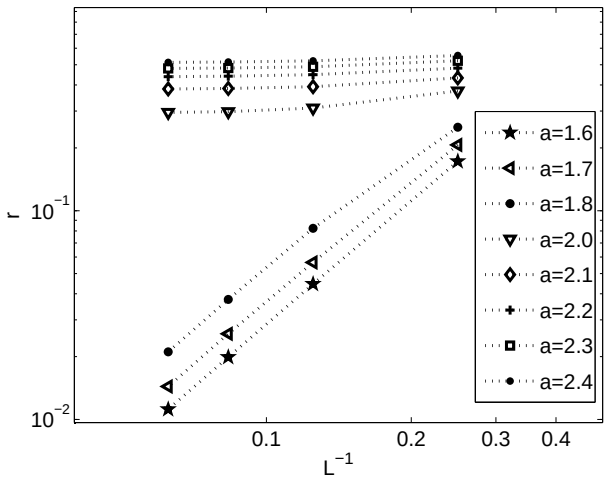

Figure 3.12: Log-log plots of r vs L^{-1} for $d = 4$. The order parameter r clearly approaches a finite, nonzero value for $a > a_c$ and approaches 0 for $a < a_c$.

Because we expect $d = 4$ to be the upper critical dimension in accordance with XY/Ising behavior, we anticipate a slight breakdown of the scaling relation (3.6). An alternate scaling ansatz valid at d_{uc} is given by (3.6) with the transformation $L \to ln(L)L^{1/4}$ [18]. A priori it is not clear how strongly (3.6) will be violated in $d = 4$, nor is it clear that the modified ansatz will better serve our purposes; therefore, we will use both forms of scaling in testing for the mean field exponents $\nu = 1/2$ and $\beta = 1/2$.

As shown in Fig. 3.13, the data collapse is very good with the mean field exponents regardless of which scaling ansatz is used. As such, our simulations suggest that $d = 4$ serves as the upper critical dimension; additionally, it appears that corrections to finite-size scaling at $d = 4$ are not substantial, though a much more precise study would be needed to investigate such corrections in greater detail.

To further support the claim that $d_{uc} = 4$, we consider the case $d = 5$. We see a transition to synchrony which occurs at $a_c = 1.750 \pm 0.015$ (see Figs. 3.14 and 3.15). As expected, this value for a_c is considerably closer than the critical coupling in four dimensions to the value $a_c = 1.5$ calculated by linear stability analysis in mean field theory.

Finally, it is interesting to test the suggestion of Jones and Young [18] that

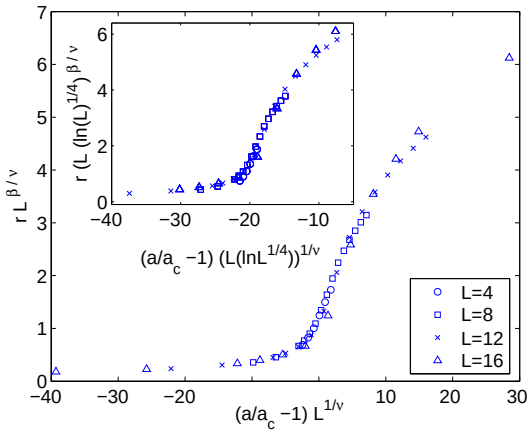

Figure 3.13: Exponents in $d = 4$: Data collapse of original ansatz (3.6) with mean field exponents. Inset: Data collapse with modified scaling ansatz $r(\ln(L)L^{1/4})^{\frac{\beta}{\nu}}$ vs $(\frac{a}{a_c} - 1)(\ln(L)L^{1/4})^{\frac{1}{\nu}}$ with mean field exponents.

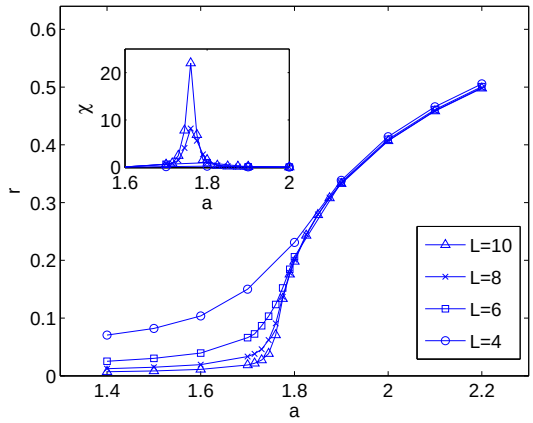

Figure 3.14: Transition in $d = 5$: The behavior of the order parameter near the transition point is shown for various system sizes. The inset shows the generalized susceptibility, χ, which peaks at $a = 1.750 \pm 0.015$, giving an estimation of a_c.

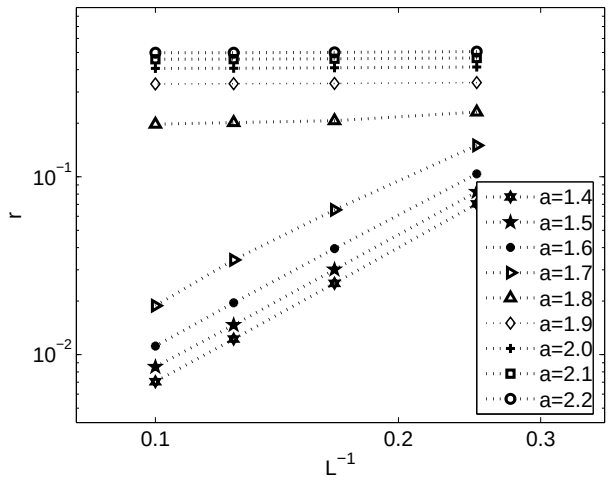

Figure 3.15: Log-log plots of r vs L^{-1} in $d = 5$. The order parameter r clearly approaches a finite, nonzero value for $a > a_c$ and approaches 0 for $a < a_c$. The value of a_c appears to fall between $a = 1.8$ and $a = 1.7$.

above the critical dimension, $d \geqslant d_{uc}$, it is appropriate to modify the finite size scaling ansatz (3.6) by the transformation $L \to L^{d/4}$. We test this suggestion for $d = 5$. As indicated in Fig. 3.16, the data collapse is excellent for both the original scaling and the modified form of the ansatz. The collapse of the data with mean field exponents seems slightly better using the modified ansatz, though a much more precise study would be required to accurately capture the form of the modified scaling in $d > d_{uc}$. In any case, our data suggest that the model exhibits mean field behavior in $d = 5$, verifying that $d = 4$ serves as the upper critical dimension.

3.5 Discussion

We have introduced a simple discrete model for studying phase coherence in spatially distributed populations of noisy coupled oscillators. This model lends itself to numerical study even in the case of nearest neighbor coupling because each oscillator is a simple three-state system rather than one of the usual continuum choices. The coupled system is therefore much simpler than the usual set of coupled nonlinear differential equations.

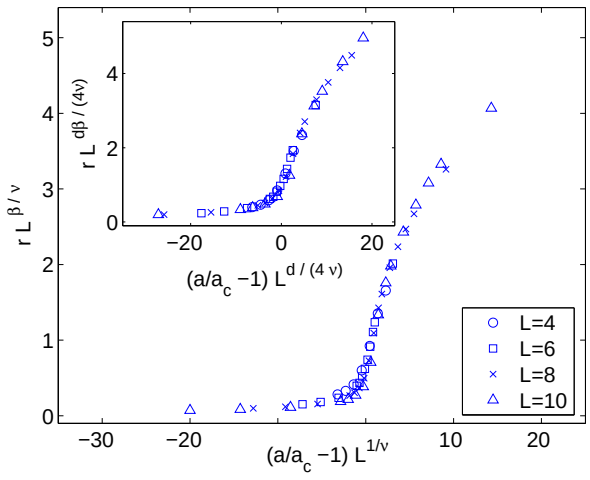

Figure 3.16: Exponents in $d = 5$: Data collapse of original ansatz (3.6) with mean field exponents. Inset: Data collapse of $rL^{\frac{d\beta}{4\nu}}$ vs. $(a/a_c - 1)L^{\frac{d}{4\nu}}$ with mean field exponents. The collapse of the data is quite convincing when the exact mean field exponents are used.

A mean field treatment combined with linear stability analysis shows that the globally coupled model undergoes a supercritical Hopf bifurcation to macroscopic synchrony as the coupling parameter a is increased. We are able to determine the mean field critical coupling constant analytically. For locally coupled units, numerical solution of the system shows the emergence of a thermodynamic synchronous phase for $d > 2$, indicating that the lower critical dimension is $d_{lc} = 2$. As d is increased, the numerically established critical value a_c approaches that predicted by the mean field treatment of the model. For $d = 3$, we give strong numerical evidence that the model falls into the 3D XY universality class, while for $d = 4$ the critical exponents are those predicted by mean field theory. The exponents in $d = 5$ also take on the mean field values, thus verifying that $d = 4$ corresponds to the upper critical dimension d_{uc}.

While nonequilibrium phase transitions have a much wider diversity in universality classes than equilibrium ones [19], it is remarkable that the prototype of a nonequilibrium transition, namely, a phase transition that breaks the symmetry of translation in time, is described, at least for the critical exponents investigated in this paper, by an equilibrium universality class. In particular, the Mermin-Wagner theorem, stating

that continuous symmetries can not be broken in dimension two or lower, appears to apply. Furthermore, the XY model is known to display a Kosterlitz-Thouless transition, in which, beyond a critical temperature, vortex pairs can unbind into individual units creating long range correlations. Preliminary results indicate that a similar transition occurs in our model, though a detailed study is still beyond our reach. Finally, a note of caution concerning the discreteness of the phase is in order. We first note that microscopic models often feature discrete degrees of freedom. For example, our model is reminiscent of the triangular reaction model introduced by Onsager [20], on the basis of which he illustrated the concept of detailed balance as a characterization of equilibrium. Continuous phase models appear in a suitable thermodynamic limit. We stress that the breaking of time translational symmetry can occur independently of whether the phase is a discrete or continuous variable. It is, however, not evident whether continuous and discrete phase models belong to the same universality class. The results found here seem to support the latter thesis, but a renormalization calculation confirming this hypothesis would be welcome.

Acknowledgements

Chapter 3 contains material which appears, in part, in K. Wood, C. Van den Broeck, R. Kawai, and K. Lindenberg, Phys. Rev. Lett. **96**, 145701 (2006); K. Wood, C. Van den Broeck, R. Kawai, and K. Lindenberg, Phys. Rev. E **74**, 031113 (2006); and K. Wood, C. Van den Broeck, R. Kawai, and K. Lindenberg, in preparation (2007).

References

[1] S. H. Strogatz, *Nonlinear Dynamics and Chaos* (Westview Press, 1994).

[2] A. T. Winfree, J. Theor. Biol. **16**, 15 (1967).

[3] Y. Kuramoto, *Chemical Oscillations, Waves, and Turbulence* (Springer, Berlin, 1984).

[4] S. H. Strogatz, Physica D **143**, 1 (2000).

[5] H. Sakaguchi, S. Shinomoto, and Y. Kuramoto, Prog. Theor. Phys. **77**, 1005 (1987); H. Daido, Phys. Rev. Lett. **61**, 231 (1988); S. H. Strogatz and R. E. Mirollo, J. Phys. A **21**, L699 (1988); *idem*, Physica D **31**, 143 (1988); H. Hong, H. Park, and M. Choi, Phys. Rev. E **71**, 054204 (2004).

[6] D. Walgraef, G. Dewel, and P. Borckmans, J. Chem. Phys. **78**, 3043 (1983).

[7] M. Malek Mansour, J. Dethier, and F. Baras, J. Chem. Phys. **114**, 9265 (2001).

[8] H.Hong, H. Park, M. Choi, Phys. Rev. E **71**, 054204 (2004).

[9] A. Pikovsky, M. Rosenblum, J. Kurths, *Synchronization: A Universal Concept in Nonlinear Science* (Cambridge University Press, Cambridge, 2001).

[10] T. Risler, J. Prost, F. J ulicher. Phys. Rev. Lett. **93**, 175702 (2004).

[11] T. Risler, J. Prost, and F. J ulicher, Phys. Rev. E **72**, 016130 (2005).

[12] N. Goldenfeld, *Lectures on Phase Transitions and the Renormalization Group* (Westview Press, 1992).

[13] F. Rogister and R. Roy, Phys. Rev. Lett. **98**, 104101 (2007).

[14] K. Binder, Z. Phys. B **43**, 119 (1981).

[15] A. P. Gottlob and M. Hasenbusch, Nucl. Phys. B Suppl. **30**, 838 (1993).

[16] K. Huang, *Statistical Mechanics* Second Edition (Wiley, New York, 1988).

[17] A. Pelissetto and E. Vicari, Phys. Rep. **368**, 549 (2002).

[18] J. Jones and A. Young, Phys. Rev. B **71**, 174438 (2005).

[19] See, e.g., J. Marro and R. Dickman, *Nonequilibrium Phase Transitions in Lattice Models* (Cambridge University Press, Cambridge, 1999) and references therein; V. Privman, *Nonequilibrium Statistical Mechanics in One Dimension* (Cambridge University Press, Cambridge, 1997).

[20] L. Onsager, Phys. Rev. **37**, 405; *ibid*, Phys. Rev. **38** 2265(1931).

4

Effects of Disorder on Synchronization of Discrete Phase-Coupled Oscillators

4.1 Introduction

Starting with Kuramoto's canonical model of nonlinear oscillators, simple, phenomenological models of synchronization have proven useful in a variety of contexts [1, 2, 3, 4, 5, 6, 7, 8, 9], including the characterization of emergent synchronization as a nonequilibrium phase transition (see Chapter 3). We have seen [8, 9] in Chapters 2 and 3 that a model of three-state identical phase-coupled stochastic oscillators is ideally suited for studying the nonequilibrium phase transition to synchrony in locally-coupled systems, owing in large part to its numerical simplicity. The utility of these studies rests on the well-established notion of universality, that is, on the contention that microscopic details do not determine the universal properties associated with the breaking of time-translational symmetry that leads to a macroscopic phase transition. Statistical mechanics is thus enriched by simplistic, phenomenological models (the Ising model being the most ubiquitous example) whose microscopic specifics are known to be, at best, substantial simplifications of the underlying quantum mechanical nature of matter, but whose critical behavior captures that of more complex real systems. In this spirit, our

simple tractable model captures the principal features of the synchronization of phase-coupled oscillators. In the globally coupled (mean field) case our model undergoes Hopf bifurcation which can be either subcritical or supercritical. With appropriately chosen nearest neighbor coupling, we have shown that the array undergoes a continuous phase transition to macroscopic synchronization marked by signatures of the XY universality class [10, 11], including the correct classical exponents β and ν, and lower and upper critical dimensions 2 and 4 respectively.

In this chapter we focus on globally coupled arrays and expand our earlier studies to the arena of transition rate disorder. We start with our three state model (Eq. (2.1)), in which identical synchronized units are governed by the same transition rates as individual uncoupled units. Then, in the spirit of the original Kuramoto problem [3], we explore the occurrence of synchronization when there is more than one transition rate and perhaps even a distribution of transition rates among the phase-coupled oscillators. In particular, we explore the conditions (if any) that lead to a synchronization transition in the face of a transition rate distribution, discuss the relation between the frequency of oscillation of the synchronized array and the transition rates of individual units, and explore whether or not the existence of units of different transition rates in the coupled array may lead to more than one phase transition.

The chapter is organized as follows. In Sec. 4.2 we describe the model, including our choice of coupling coefficients (U, V, W) (see Eq. (2.4)) and the associated rationale, for an array of identical units. In Sec. 4.3 we present results for a dimer composed of two units of different intrinsic transition rates. While there is of course no phase transition in this system, it is instructive to note that there is a probability of synchronization of the two units that increases with increasing coupling strength. Section 4.4 introduces disorder of a particular kind, useful for a number of reasons that include some analytical tractability. Here our oscillators can have only one of $\mathcal{N}$ distinct transition rates, where $\mathcal{N}$ is a small number. We pay particular attention to the dichotomous case, $\mathcal{N} = 2$. This simple disordered system reveals some important general signatures of synchronization. We also consider the cases $\mathcal{N} = 3$ and $\mathcal{N} = 4$, but find that the $\mathcal{N} = 2$ case already exhibits most of the interesting qualitative consequences of a distribution of transition rates. In particular, we are able to infer the important roles of the mean and variance of the distribution. In Sec. 4.5 we generalize further to a uniform finite-width distribution

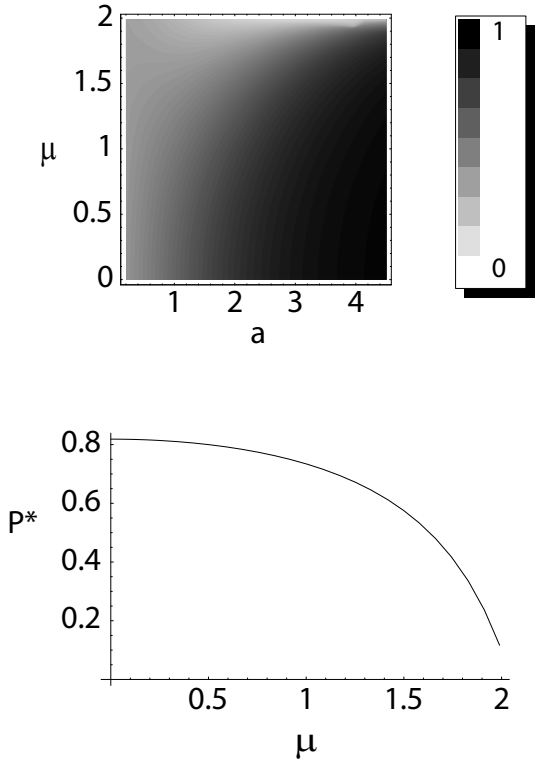

Figure 4.1: The steady state probability $\mathcal{P}_A^*$ that both units of a dimer are in the same state for a range of μ and a. Top: contour image. Bottom: a single curve for $a = 2.2$. In the latter case, it is clear that as μ rises, synchronization rapidly decreases.

of transition rates and explore this inference in more detail. Section 4.6 summarizes our results and poses some questions for further study.

4.2 The Model

Our point of departure is once again a stochastic three-state model governed by transition rates g (see Fig. 2.1), where each state may be interpreted as a discrete phase [8, 9]. The unidirectional, probabilistic nature of the transitions among states assures a qualitative analogy between this three-state discrete phase model and a noisy phase oscillator.

To study coupled arrays of these oscillators, we couple individual units by

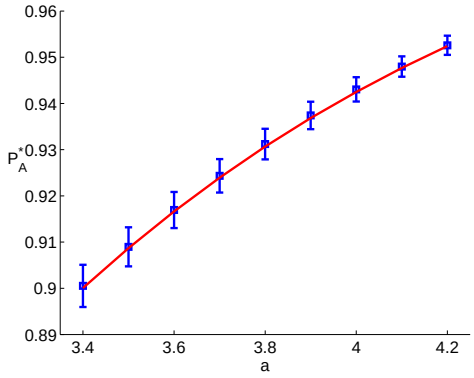

Figure 4.2: The steady state probability $\mathcal{P}_A^*$ that both units of a dimer are in the same state for $(\gamma_1, \gamma_2) = (0.5, 1.5)$ as a is increased. The points represent simulation results averaged over 75 independent realizations, where $\mathcal{P}_A^*$ is measured as the fraction of time that both units are fully synchronized. The error bars represent $\pm$ one standard deviation over these realizations. The solid line is the analytical result.

allowing the transition rates of each unit to depend on the states of the units to which it is connected. Specifically, for N identical units we choose the transition rate of a unit ν from state i to state $i+1$ as

$$g_i = g \exp\left[\frac{a(N_{i+1} - N_{i-1})}{n}\right], \tag{4.1}$$

where a is the coupling parameter, g is the transition rate parameter, n is the number of oscillators to which unit ν is coupled, and N_k is the number of units among the n that are in state k. Note that this corresponds to Eq. (2.4) with $(U, V, W) = (1, -1, 0)$. Each unit may thus transition to the state ahead or remain in its current state in a manner dependent on the states of the remaining units to which it is coupled. In early chapters we have considered the globally coupled system, $n = N - 1$, and also nearest neighbor coupling in square, cubic, or hypercubic arrays, $n = 2d$ (d = dimensionality). Here we focus on the globally coupled array. We are led to the familiar set of mean field equations given by Eqs. (2.5, 2.6) containing a coupling specified by Eq. (4.1). We remind the reader that this model undergoes a Hopf bifurcation at a critical coupling of $a_c = 3$.

Our previous chapter used a different form of the coupling, with $(U, V, W) = (1, 0, -1)$, which guaranteed a continuous phase transition. That earlier choice was

also numerically advantageous because it led to a phase transition at a lower critical value a_c of the coupling constant ($a_c = 1.5$ in the globally coupled array) than other choices. A lower coupling in turn facilitates numerical integration of equations of motion because the time step that one needs to use near the phase transition must be sufficiently small, $dt \ll e^{-a}/g$. However, that previous coupling choice brought with it a result that is undesirable in our present context (but was of no consequence before, where we only dealt with behavior near criticality). In our earlier model, as the units become increasingly synchronized above the transition point, the average transition rate of a cluster becomes substantially dependent on the value of a; specifically, the transitions and cluster oscillation frequency slow as a is increased due to an exponential decrease in the transition probability. To cite an explicit example, consider a small subsystem composed of units which are all in the same state at time t (that is, a cluster of units which are perfectly synchronized). The previous form of the coupling yields an exponentially small transition rate in this case, and hence the oscillation frequency of this microscopic cluster approaches zero for high values of a. In fact, a similar problem arises for any coupling with $W \neq 0$, indicating that these models are not appropriate for studies far above threshold owing to an anomalous (and exponential) slowing down or speeding up of oscillators.

Since here we specifically wish to analyze the effects of transition rate disorder, it is desirable to deal with a model in which the average transition rate of identical synchronized units depends only on their intrinsic transition rate parameter and not on coupling strength. The form (4.1)–and in fact any choice with $W = 0$–reduces simply to the constant g when the coupled units are perfectly synchronized, meaning our model retains a finite, nonzero frequency in the strongly coupled limit. On the other hand, the critical coupling in this new version is higher than in our earlier model and hence it is numerically less efficient. In addition, the Lyapunov coefficient l_1 vanishes for this choice of coupling, so we can not be assured of a continuous phase transition. In fact, we will see below that in certain cases the nature of the phase transition depends on the level of disorder within the population. With that exception, we focus our attention in this chapter on the requirements for macroscopic cooperativity, not the nature of the corresponding transition.

4.3 Dimer

Consider first the simplest "disordered array," namely, a mutually coupled dimer where one unit is characterized by $g = \gamma_1$ and the other by $g = \gamma_2$. In terms of the states (phases) S_1 and S_2 of units 1 and 2, there are 9 possible dimer states, $(S_1, S_2) = (1,1), (1,2), \ldots, (3,3)$, but it is not necessary to seek the ensemble distributions for all of these states in order to decide whether or not the two units are synchronized. We can directly write an exact reduced linear evolution equation for the 3 states A, B, and C, where A corresponds to any situation where both units are in the same state [that is, $(S_1, S_2) = (1,1), (2,2)$, and $(3,3)$], state B corresponds to a situation where unit 1 is one state "ahead" [$(S_1, S_2) = (2,1), (3,2)$, and $(1,3)$], and state C corresponds to a situation where unit 2 is one state "ahead" [$(S_1, S_2) = (1,2), (2,3)$, and $(3,1)$]. The evolution equation for these states is the closed linear set

$$\partial \boldsymbol{\mathcal{P}}(t)/\partial t = \mathcal{A}\boldsymbol{\mathcal{P}}(t), \tag{4.2}$$

with $\boldsymbol{\mathcal{P}}(t)$ the time dependent probability column vector $(\mathcal{P}_A(t)\ \mathcal{P}_B(t)\ \mathcal{P}_C(t))^T$ and

$$\mathcal{A} = \begin{pmatrix} -\gamma_1 - \gamma_2 & b\gamma_2 & b\gamma_1 \\ \gamma_1 & -b^{-1}\gamma_1 - b\gamma_2 & b^{-1}\gamma_2 \\ \gamma_2 & b^{-1}\gamma_1 & -b\gamma_1 - b^{-1}\gamma_2 \end{pmatrix}, \tag{4.3}$$

and where we have introduced the abbreviation

$$b \equiv e^a. \tag{4.4}$$

This evolution equation is easy to derive from the definition of the coupling, Eq. (4.1). For example, when the system is in state A, it can either go to state B, which happens when unit 1 jumps ahead with transition rate γ_1, or it can go to state C, which happens when unit 2 jumps ahead with transition rate γ_2. Similarly, when the system is in state B, it can either jump to state A (when the lagging unit transitions forward) with transition rate $b\gamma_2$ or jump to state C (when the leading unit transitions forward) with transition rate $b^{-1}\gamma_1$.

With normalization, Eq. (4.2) becomes a 2-dimensional equation having steady

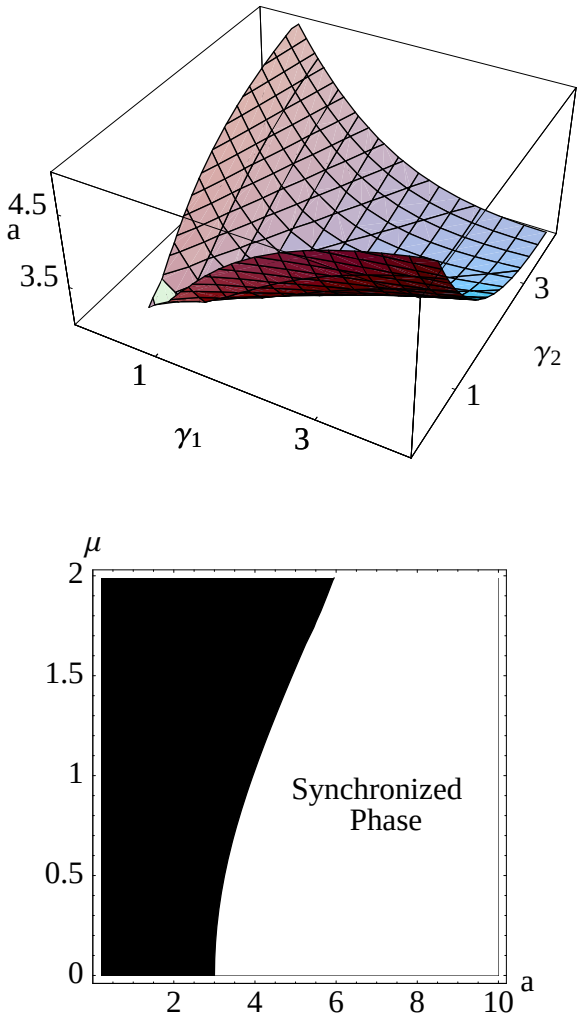

Figure 4.3: Upper panel: Stability boundary for the dichotomously disordered system. The contour $\mathrm{Re}\lambda_+ = 0$ is plotted in (γ_1, γ_2, a) space. This contour indicates the critical point, where the Hopf bifurcation occurs and the disordered solution becomes unstable. The region above the contour represents the synchronized phase. Lower panel: Stability boundary in terms of relative width parameter.

state solution

$$\begin{aligned} \mathcal{P}_A^* &= \frac{b(\gamma_1^2 + b^2\gamma_1\gamma_2 + \gamma_2^2)}{(1+b+b^2)(\gamma_1^2+\gamma_2^2) + (2+b^3)\gamma_1\gamma_2}, \\ \mathcal{P}_B^* &= \frac{b^2\gamma_1^2 + \gamma_2(\gamma_1+\gamma_2)}{(1+b+b^2)(\gamma_1^2+\gamma_2^2) + (2+b^3)\gamma_1\gamma_2}. \end{aligned} \tag{4.5}$$

The eigenvalues of the two-dimensional matrix obtained from $\mathcal{A}$ after implementing normalization have negative real parts for all positive values of the parameters a, γ_1, and γ_2, indicating that the fixed points given by Eq. (4.5) are stable. Hence, the system asymptotically tends to this steady state solution. We are particularly interested in $\mathcal{P}_A^*$, the probability for the system to be synchronized. In terms of the single relative width parameter width/mean,

$$\mu \equiv \frac{2|\gamma_1 - \gamma_2|}{(\gamma_1+\gamma_2)} \tag{4.6}$$

$(0 \leq \mu \leq 2)$, this probability is

$$\mathcal{P}_A^* = \frac{b}{(2+b)} \left(\frac{1 + \mu^2 \frac{(2-b^2)}{4(2+b^2)}}{1 + \mu^2 \frac{b(2+2b-b^2)}{4(2+b^2)(2+b)}} \right). \tag{4.7}$$

The probability of synchronization for a dimer of identical units ($\mu = 0$) is thus $\mathcal{P}_A^* = b/(2+b) = e^a/(2+e^a)$, which increases with increasing coupling. This is the maximal synchronization; it is easy to ascertain that $\mathcal{P}_A^*$ decreases with increasing μ, as one would anticipate. The full behavior of $\mathcal{P}_A^*$ as a function of the various parameters is shown in Figs. 4.1-4.2. The gradual increase in synchronization probability with increasing coupling turns into a sharp transition as a function of a in the infinite systems to be considered below. The decreased synchronization probability when the frequencies of the two units become more dissimilar (increasing μ) will also be reflected in the dependence of the critical coupling on transition rate parameter disorder.

4.4 $\mathcal{N}$ Different Transition Rates

Next we consider globally coupled arrays of oscillators that can have one of $\mathcal{N}$ different transition rate parameters, $g = \gamma_u$, $u = 1, \ldots, \mathcal{N}$. To arrive at a closed set of mean field equations for the probabilities we again go to the limit of an infinite number of oscillators, $N \to \infty$. However, we must do so while preserving a finite density of each

of the $\mathcal{N}$ types of oscillators. The probability vector is now $3\mathcal{N}$-dimensional, $\boldsymbol{P}(t) = (P_{1,\gamma_1}\ P_{2,\gamma_1}\ P_{3,\gamma_1}\ \cdots\ P_{1,\gamma_\mathcal{N}}\ P_{2,\gamma_\mathcal{N}}\ P_{3,\gamma_\mathcal{N}})^T$. The added subscript on the components of $\boldsymbol{P}(t)$ keeps track of the transition rate parameter. Explicitly, the component P_{i,γ_u} is the probability that a unit with transition rate parameter $g = \gamma_u$ is in state i. The mean field evolution for the probability vector is the set of coupled nonlinear differential equations $\partial \boldsymbol{P}(t)/\partial t = M_\mathcal{N}[\boldsymbol{P}(t)]\boldsymbol{P}(t)$, with

$$M_\mathcal{N}[\boldsymbol{P}(t)] = \begin{pmatrix} \mathcal{M}_{\gamma_1} & 0 & \dots & 0 \\ 0 & \mathcal{M}_{\gamma_2} & \dots & 0 \\ \vdots & \vdots & \vdots & \vdots \\ 0 & \dots & 0 & \mathcal{M}_{\gamma_\mathcal{N}} \end{pmatrix}. \tag{4.8}$$

Here

$$\mathcal{M}_{\gamma_u} = \begin{pmatrix} -g_1(\gamma_u) & 0 & g_3(\gamma_u) \\ g_1(\gamma_u) & -g_2(\gamma_u) & 0 \\ 0 & g_2(\gamma_u) & -g_3(\gamma_u) \end{pmatrix}, \tag{4.9}$$

and

$$g_i(\gamma_u) = \gamma_u \exp\left[a \sum_{k=1}^{\mathcal{N}} \varphi(\gamma_k) \left(P_{i+1,\gamma_k} - P_{i-1,\gamma_k} \right) \right]. \tag{4.10}$$

The function $\varphi(\gamma_k)$ is the fraction of units which have a transition rate parameter $g = \gamma_k$.

We focus on uniform distributions $\varphi(\gamma_k) = 1/\mathcal{N}$, but subsequently take note of the consequences of relaxing this assumption. For uniform distributions, probability normalization again allows us to reduce this to a system of $2\mathcal{N}$ coupled ordinary differential equations. It is interesting to compare this setup with that of the original Kuramoto problem with noise, where a continuous frequency distribution is introduced and the governing equation is a nonlinear partial differential equation [the Fokker-Planck equation for the density $\rho(\theta, \omega, t)$] [12]. The discretization of phase in our model results instead in a set of $2\mathcal{N}$ coupled nonlinear ordinary differential equations.

While it is nevertheless still difficult to solve these equations even for small $\mathcal{N}$, we can linearize about the disordered state $\boldsymbol{P}(t) = (1/3\ 1/3\ \dots\ 1/3)^T$ and arrive at a

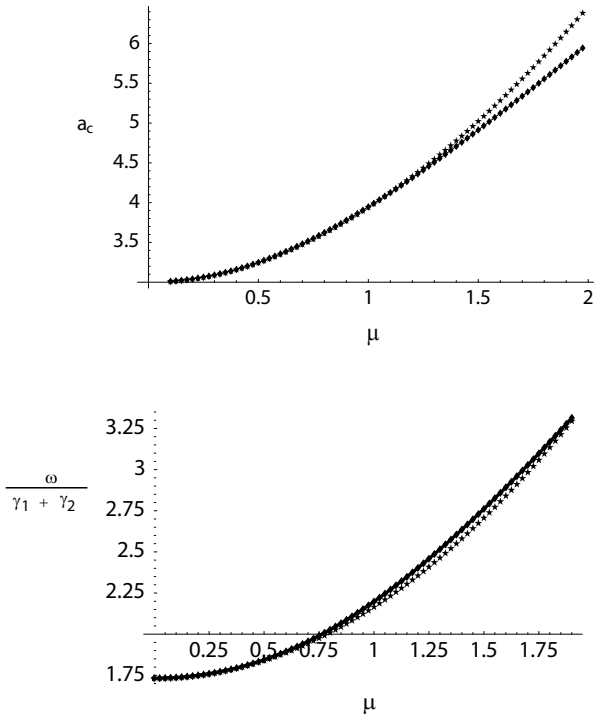

Figure 4.4: Upper panel: Critical coupling a_c as a function of μ for a dichotomous ($\mathcal{N} = 2$) array of globally coupled oscillators. The two curves represent the exact relationship (lower curve) and the small μ approximation (upper curve), respectively. Lower panel: The frequency of synchronous oscillation at the transition point. Lower curve is the approximation as predicted by $\mathrm{Im}\lambda_+$, upper curve is the exact result.

$2\mathcal{N} \times 2\mathcal{N}$ Jacobian of the block matrix form

$$J = \begin{pmatrix} \mathcal{J}_1(\gamma_1) & \mathcal{J}_2(\gamma_1) & \mathcal{J}_2(\gamma_1) & \dots & \mathcal{J}_2(\gamma_1) \\ \mathcal{J}_2(\gamma_2) & \mathcal{J}_1(\gamma_2) & \mathcal{J}_2(\gamma_2) & \dots & \mathcal{J}_2(\gamma_2) \\ \vdots & \vdots & \vdots & \vdots & \vdots \\ \vdots & \vdots & \vdots & \vdots & \vdots \\ \mathcal{J}_2(\gamma_N) & \mathcal{J}_2(\gamma_N) & \dots & \mathcal{J}_2(\gamma_N) & \mathcal{J}_1(\gamma_N) \end{pmatrix}. \tag{4.11}$$

The blocks $\mathcal{J}_1(g)$ and $\mathcal{J}_2(g)$ are given by:

$$\mathcal{J}_1(g) = \begin{pmatrix} -2g & -g - ag/N \\ g + ag/N) & -g + ag/N \end{pmatrix} \tag{4.12}$$

and

$$\mathcal{J}_2(g) = \begin{pmatrix} 0 & -ag/N \\ ag/N & ag/N \end{pmatrix}. \tag{4.13}$$

While we explore this in more detail below only for small $\mathcal{N}$, we note that in general the Jacobian (4.11) has $\mathcal{N}$ pairs of complex conjugate eigenvalues, only *one pair of which seems to have a real part that becomes positive* with increasing coupling constant a. This implies that there is a *single* transition to synchrony even in the presence of the transition rate disorder that we have introduced here. We go on to confirm this behavior for $\mathcal{N} = 2$, 3, and 4.

4.4.1 Two transition rate parameters

For the $\mathcal{N} = 2$ case, the four eigenvalues $(\lambda_+, \lambda_+^*, \lambda_-, \lambda_-^*)$ of the Jacobian can be determined analytically. We find

$$\begin{aligned} \frac{\mathrm{Re}\lambda_\pm}{\gamma_1 + \gamma_2} &= \frac{1}{8}\left[a - 6 \pm B(a,\mu)\cos\left(C(a,\mu)\right)\right], \\ \frac{\mathrm{Im}\lambda_\pm}{\gamma_1 + \gamma_2} &= \frac{1}{8}\left[\sqrt{3}(a+2) \pm B(a,\mu)\sin\left(C(a,\mu)\right)\right], \end{aligned} \tag{4.14}$$

where

$$\begin{aligned} B(a,\mu) &\equiv \sqrt{2}\left[a^4 - 6a^2\mu^2 + 3\mu^4(a^2+3)\right]^{1/4}, \\ C(a,\mu) &\equiv \frac{1}{2}\tan^{-1}\left(\frac{-\sqrt{3}(a^2 - (a+3)\mu^2)}{a^2 + 3(a-1)\mu^2}\right). \end{aligned} \tag{4.15}$$

Aside from an overall factor $(\gamma_1 + \gamma_2)$, Eqs. (4.14) depend only on the relative width variable as defined in Eq. (4.6), and therefore the critical coupling a_c depends only on μ. As illustrated in the upper panel of Fig. 4.12, one pair of eigenvalues acquires a positive real part (i.e., crosses the imaginary axis) at a critical value $a = a_c$, but the other pair shows no qualitative change as a is varied. While this figure shows only the particular transition rate parameter values $(\gamma_1, \gamma_2) = (1, 3)$, the qualitative features of these eigenvalues remain similar for the entire range of positive parameters. The upper panel of Fig. 4.3 depicts the contour $\mathrm{Re}\lambda_+ = 0$ in (γ_1, γ_2, a) space; this contour represents the critical surface and thus separates the synchronous and disordered phases.

The critical coupling is the value of a at which $\mathrm{Re}\lambda_+ = 0$ ($\mathrm{Re}\lambda_-$ does not vanish for any a). It is easy to ascertain that $\mathrm{Im}\lambda_+$ does not vanish at a_c, so that the critical point is a Hopf bifurcation. Furthermore, it is clear from Eq. (4.14) that a_c depends only on the relative width parameter μ, and it is also straightforward to establish that a_c increases with increasing μ, that is, a stronger coupling is necessary to overcome increasingly different values of γ_1 and γ_2 (see lower panel of Fig. 4.3). Note, however, that the dependence on μ implies that it is not just the difference in transition rates but the *relative* difference or percent difference relative to the mean transition rate that is the determining factor in how strong the coupling must be for synchronization to occur. A small-μ expansion leads to an estimate of a_c to $O(\mu^2)$,

$$a_c \approx \frac{1}{8}\left(12 + 3\mu^2 + \sqrt{3}\sqrt{(12+\mu^2)(4+3\mu^2)}\right), \tag{4.16}$$

a result that exhibits these trends explicitly. The upper panel in Fig. 4.4 shows that this estimate is remarkably helpful even when μ^2 is not so small.

The frequency of oscillation of the synchronized system at the transition is given by $\omega = \lim_{a\to a_c}\mathrm{Im}\lambda_+$. From Eq. (4.14) it follows that ω depends on $(\gamma_1 + \gamma_2)$ as well as μ. The small-μ expansion leads to the estimate

$$\omega = Im(\lambda_\pm)|_{a\to a_c} \approx \frac{1}{4}\sqrt{3}(\gamma_1 + \gamma_2)(4 + \mu^2), \tag{4.17}$$

which works exceedingly well up to $\mu \sim 1$ (see Fig. 4.4).

To check the predictions of our linearization procedure, we numerically solve the nonlinear $\mathcal{N} = 2$ mean field equations. In agreement with the structure of the linearized eigenvalues, all components of $\boldsymbol{P}(t)$ synchronize to a common frequency as the phase

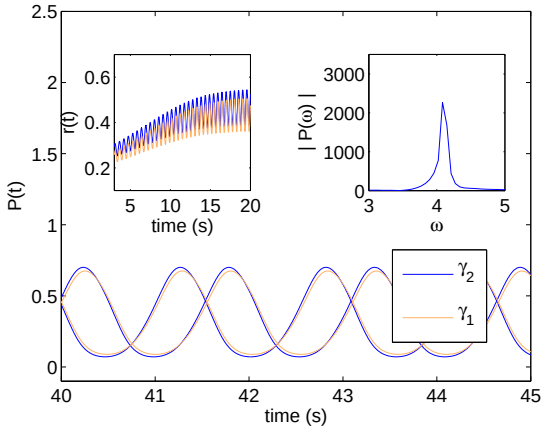

Figure 4.5: The components P_{1,γ_1} and P_{2,γ_1}(two lighter or brown curves), and P_{1,γ_2} and P_{2,γ_2}(two darker or blue curves), of the vector $\boldsymbol{P}(t)$ vs time for $\gamma = 1$, $\Delta = 0.125$, with $a = 3.15$, which is above the critical value $a_c \approx 3.02$ predicted by linearization. The left inset shows the order parameter $r(t)$ as it approaches its long-time limit. The right inset shows the frequency spectrum of a component of $\boldsymbol{P}(t)$. The spectrum has a dominant peak near $\omega \approx 4$, and is expected to approach the frequency $\omega \approx 3.5$ predicted by linearization as we approach the transition point $a \to a_c$.

boundary in (μ, a)-space) is crossed. Interestingly, the numerical solutions also give us insight into the amplitude of the oscillations; that is, they allow us to explore the relative "magnitude" of synchronization within the two populations. As we will see, the two populations indeed oscillate with the same frequency, but with amplitudes and "degrees of synchronization" that can be markedly different. Consider the order parameter $r(t)$ given by

$$r(t) \equiv \frac{1}{N}\left|\sum_{\nu=1}^{N} e^{i\phi_\nu}\right|. \tag{4.18}$$

Here ϕ_ν is the discrete phase $2\pi(k\text{-}1)/3$ for state $k \in \{1, 2, 3\}$ at site ν. For phase transition studies, one would likely average this quantity over time in the long time limit, and also over independent trials. For our purposes here, though, we find the time-dependent form more convenient. In the mean field case, where we solve for probabilities to be in each state, the order parameter is easily calculated by writing the average in Eq. (4.18) in terms of these probabilities rather than as a sum over sites. Specifically,

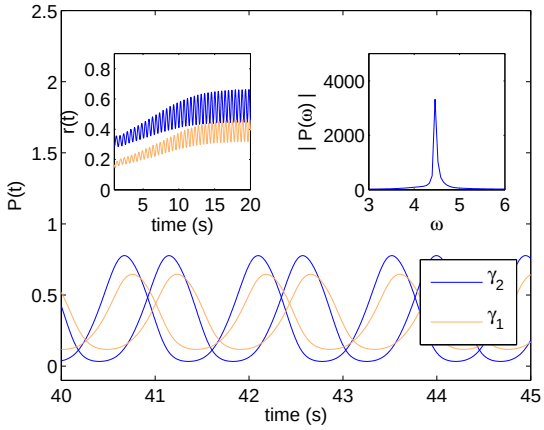

Figure 4.6: The components P_{1,γ_1} and P_{2,γ_1}(two lighter or brown curves), and P_{1,γ_2} and P_{2,γ_2}(two darker or blue curves), of the vector $\boldsymbol{P}(t)$ vs time for $\gamma = 1,\ \Delta = 0.625$, with $a = 3.5$, which is above the critical value $a_c \approx 3.39$ predicted by linearization. The left inset shows the order parameter $r(t)$ as it approaches its long-time limit. The right inset shows the frequency spectrum of a component of $\boldsymbol{P}(t)$. The spectrum has a dominant peak near $\omega \approx 4.4$, and is expected to approach the frequency $\omega \approx 3.8$ predicted by linearization as we approach the transition point $a \to a_c$.

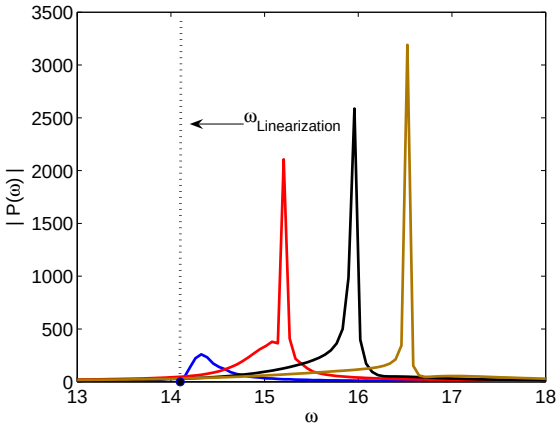

Figure 4.7: The frequency ω of macroscopic oscillations approaches the value predicted by linearization as $a \to a_c$. Here we have used $\gamma_1 = 3.5$ and $\gamma_2 = 4.5$ so that $\gamma = 4$ and $\Delta = 1$. The critical coupling constant is $a_c = 3.06$. From darkest or blue to lightest or brown: $a = 3.07$, 3.10, 3.15, and 3.20.

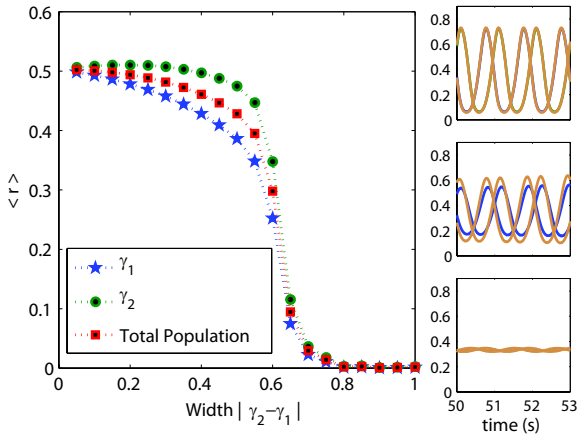

Figure 4.8: Time-averaged order parameter r in the long-time limit vs Δ for the individual oscillator populations characterized respectively by the transition rate parameter γ_1 (stars) and γ_2 (circles), and for the entire mixed array (squares). The insets show the time evolution of the probability vector components P_{1,γ_1} and P_{2,γ_1} (lighter or brown curves) and P_{1,γ_2} and P_{2,γ_2} (darker or blue curves) for widths 0.05 (upper inset), 0.5 (middle inset), and 0.9 (lower inset). Some of the curves are not visible because they are so perfectly superimposed. While the degree of synchronization varies within each population, the critical width for de-synchronization is the same for both, as predicted by linearization. The coupling constant for all cases is $a = 3.2$ and the average transition rate parameter $\gamma = 1.5$.

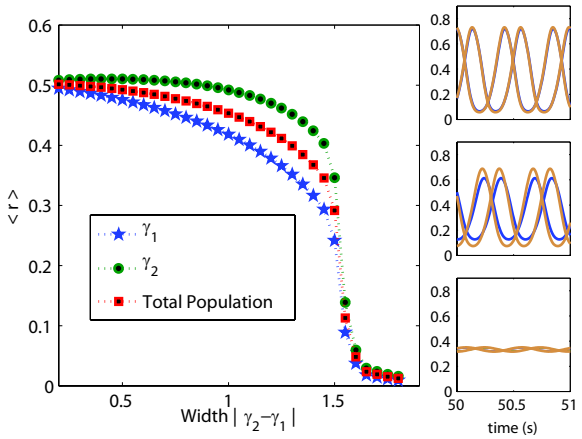

Figure 4.9: Same as Fig. 4.8 but with $\gamma = 3.5$ and widths 0.1 (upper inset), 1.3 (middle), and 1.8 (lower).

we have

$$r = \left((\sum_{i=1}^{3} P_i \cos\phi_i)^2 + (\sum_{i=1}^{3} P_i \sin\phi_i)^2 \right)^{1/2} \tag{4.19}$$

In subsequent figure captions we introduce the notation $\gamma \equiv (\gamma_1 + \gamma_2)/2$ (average transition rate parameter), and the difference $\Delta \equiv |\gamma_2 - \gamma_1|$ (note that $\mu = \Delta/\gamma$). As shown in Figs. 4.5-4.9, the predictions of linearization accurately describe the onset of macroscopic synchronization and provide an estimation of the frequency of these oscillations near threshold (see Fig. 4.7). Specifically, Figs. 4.5 and 4.6 show the macroscopic oscillations for coupling a above threshold. All the oscillators, regardless of their intrinsic transition rate parameter, oscillate in phase, but the degree of synchronization is greater in the population with the larger γ_i (here γ_2), as evidenced by the unequal amplitude of the components of $\boldsymbol{P}(t)$ for the two populations. The "greater degree of synchronization" is also apparent in the order parameter $r(t)$ shown in the insets, which is larger for the oscillators with the higher intrinsic transition rate. These results support the notion that populations with higher transition rate parameters in some sense synchronize more readily. We explore this behavior in more detail in Chapter 5. The figures also show the frequency spectrum of any component of $\boldsymbol{P}(t)$. The peak occurs at the frequency of oscillation of the synchronized array. As $a \to a_c$ this frequency approaches the value $\mathrm{Im}\lambda_+$ predicted by linearization, as shown in Fig. 4.7.

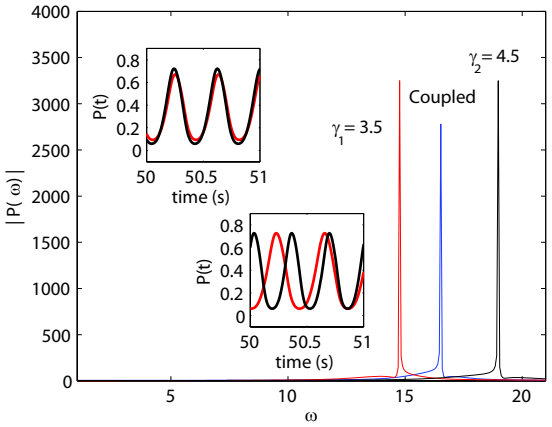

Figure 4.10: Frequency spectra of the numerical solutions to the mean field equations ($\mathcal{N} = 2$) show that above critical coupling, $a = 3.2 > a_c = 3.06$, synchronization occurs at a frequency closer to the lower of the two population frequencies. Top left inset: $P_{1,\gamma_1=3.5}$ and $P_{1,\gamma=4.5}$ when all units are globally coupled. Bottom right inset: the same curves for populations that are uncoupled from one another (but still globally coupled *within* each population).

Figures 4.8 and 4.9 illustrate the sudden de-synchronization (at fixed a and γ) accompanying an increase in the difference Δ. This behavior is reminiscent of that of the original Kuramoto oscillators, which become disordered as the width of the frequency distribution characterizing the population exceeds some critical value. The insets show the components of $P(t)$ and confirm that both populations undergo the de-synchronization transition at the same critical value of the difference Δ. Comparing the two figures, we see that the system with a higher average transition rate parameter (Fig. 4.9) can withstand a larger difference Δ before de-synchronization, again confirming our earlier observations.

One last point to consider is the relation between the frequency of oscillation of the synchronized array above a_c and the frequencies of oscillation of the two populations if they were decoupled from one another. As coupling increases, the oscillation frequency ω moves closer to that of the population with the lower transition rate parameter. This is illustrated in Fig. 4.10 for the same parameters used in Fig. 4.7.

Finally, a visually helpful illustration of these behaviors is obtained via a direct

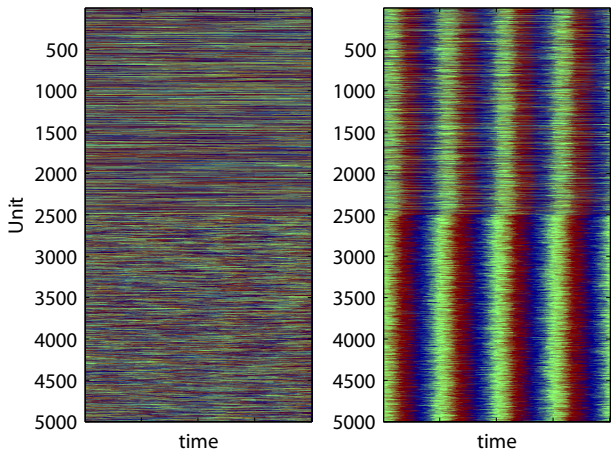

Figure 4.11: Long-time snapshots of a globally coupled system above and below threshold. In both cases, $(\gamma_1, \gamma_2) = (0.5, 1.5)$. On the left, $a = 3.5 < a_c$ while on the right, $a = 4.1 > a_c$. In both cases, all units are globally coupled. For visualization purposes, the plot is arranged so that population γ_1 consists of the first 2500 units (the top), while population γ_2 consists of the second 2500 units (the bottom). Global synchrony emerges for $a > a_c$. In addition, the population with the higher transition rate parameter is more synchronized.

simulation of an array with a dichotomous population of oscillators. Since our oscillators are globally (all-to-all) coupled, the notion of a spatial distribution is moot, and for visualization purposes we are free to arrange the populations in any way we wish. In Fig. 4.11 we display an equal number of γ_1 and γ_2 oscillators and arrange the total population of $N = 5000$ so that the first 2500 have transition rate parameter γ_1 and the remaining 2500 have transition rate parameter γ_2. In this simulation we have chosen $\gamma_1 = 0.5$ and $\gamma_2 = 1.5$, so that $\gamma = \Delta = 1$. Although $N = 5000$ is not infinite, it is large enough for this array to behave as predicted by our mean field theory. The left panel shows snapshots of the phases (each phase is indicated by a different color) when $a < a_c$ and the phases are random. The right panel shows the synchronized array when $a > a_c$. Clearly, all units are synchronized in the right panel, but the population with the higher transition rate parameter (lower half) shows a higher degree of synchronization (higher $P(t)$) as indicated by the intensity of the colors or the gray scale.

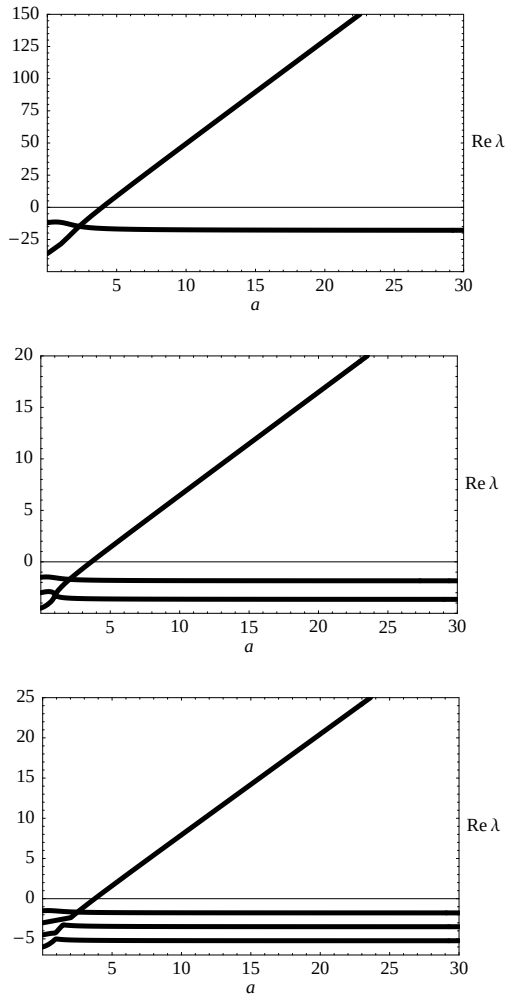

Figure 4.12: Real parts of the complex eigenvalues for $\mathcal{N} = 2$ (upper panel), $\mathcal{N} = 3$ (middle panel), and $\mathcal{N} = 4$ (lower panel) showing that in each case the real parts of only a single pair of eigenvalues becomes positive, numerically tested up to very large coupling constants ($a \leq 30$). Upper panel: $(\gamma_1, \gamma_2) = (1, 3)$; middle panel: $(\gamma_1, \gamma_2, \gamma_3) = (1, 2, 3)$; lower panel: $(\gamma_1, \gamma_2, \gamma_3, \gamma_4) = (1, 2, 3, 4)$.

4.4.2 $\mathcal{N} = 3$ and $\mathcal{N} = 4$

We can carry out this analysis, albeit not analytically (at least in practice), for any $\mathcal{N}$. We have explored the cases $\mathcal{N} = 3$ and 4. In both cases there appears to be only one pair of eigenvalues whose real parts can become positive, suggesting that synchronization occurs all at once and not in one population at a time (middle and lower panels of Fig. 4.12). This occurs no matter the distribution of the 3 or 4 transition rate parameters. For example, in the $\mathcal{N} = 4$ case we have compared in some detail the cases where the four transition rates are equidistant and where they are pairwise much closer than the separation between the highest and lowest. In both cases there is a single transition to synchrony, albeit not at exactly the same value of a_c, indicating a more complex dependence on the transition rate parameter distribution than just via its mean and width. Furthermore, the basic trends of the dichotomous case broadly carry over, mainly in that the critical value a_c increases when the width of the distribution increases relative to the mean (as one would expect). On the other hand, the inclusion of more transition rates within a given range leads to a lowering of the critical coupling. Thus, for example, the mean transition rate γ and the width Δ are the same in the cases shown in the upper and middle panels of Fig. 4.12 ($\gamma = \Delta = 2$), and yet a_c is higher in the former (3.95 for $\mathcal{N} = 2$) than in the latter (3.6 for $\mathcal{N} = 3$). Still, the mean and width of the distribution provide a rough qualitative assessment of the behavior, particularly for the case of a continuous uniform distribution, which we study in the next section.

In this analysis we have focused on disorder with a uniform distribution, that is, each of the $\mathcal{N}$ frequency parameters is represented by a fraction $1/\mathcal{N}$ of the population of oscillators. How robust are our results to a change in this distribution? In particular, if the frequency parameters are not equally represented, will there still be a single transition to synchronization? Will the mean and width of the distribution still be the principal measures of the qualitative behavior of the system? While we leave most of this analysis to future work, we are willing to make a conjecture about the generalization of the principal finding of this work: that there will still be a *single* transition to synchronization regardless of the distribution. In fact, we conjecture that the strongest "conflict" for the system is posed by a uniform distribution, since any other will have majority populations that are more likely to be more determinant of the behavior of the

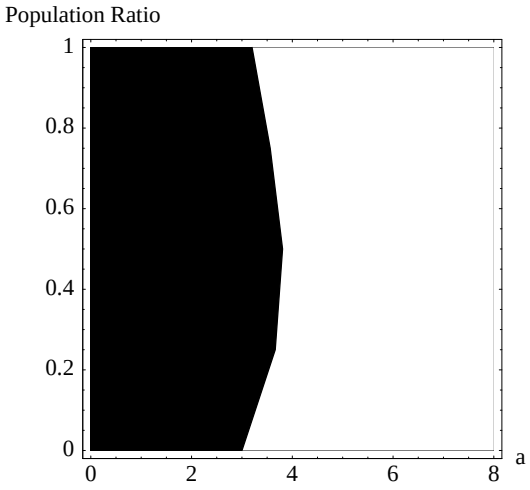

Figure 4.13: Stability boundary in terms of population ratios $\varphi(\gamma_1)/\varphi(\gamma_2)$ of oscillators with frequency parameters $\gamma_1 = 1$ and $\gamma_2 = 2$.

system. To support this conjecture, we present in Figs. 4.13 and 4.14 illustrative results for nonuniform dichotomous populations. In Fig. 4.13 we show the stability boundary for varying population ratios as a function of the coupling parameter. In Fig. 4.14 we show the real parts of each of the two pairs of eigenvalues with increasing coupling for a number of population ratios, as detailed in the caption. Again, only the real parts of one pair of eigenvalues crosses from negative to positive, indicating a single transition to synchronization for the entire system. Note that the critical coupling approaches $a_c = 3$ at each population extreme (consistent with the fact that a_c in an array of identical oscillators is independent of the frequency parameter [8, 9]), and that, as conjectured, the strongest coupling is required for synchronization when the two populations are equally represented. While Figs. 4.13 and 4.14 only show results for $(\gamma_1, \gamma_2) = (1, 2)$, we obtain similar results for other pairs of frequency parameters within the range of values used in other figures in this chapter.

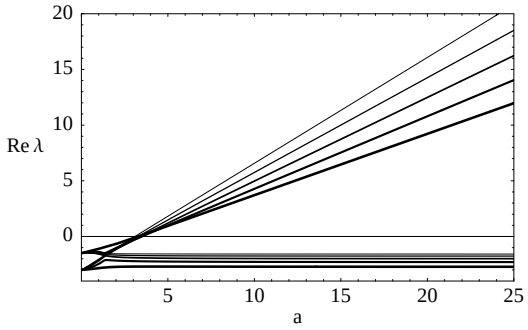

Figure 4.14: Real parts of the complex eigenvalues for two populations of oscillators with frequency parameters $\gamma_1 = 1$ and $\gamma_2 = 2$. The population ratios $\varphi(\gamma_1)/\varphi(\gamma_2)$ are 99/1, 3/1, 1/1 (the case analyzed in detail in the paper), 1/3, and 1/99.

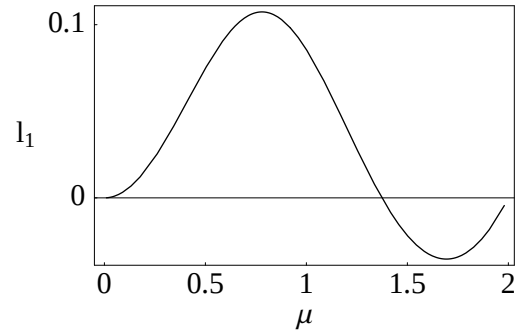

Figure 4.15: The first Lyapunov coefficient l_1 is shown for Hopf bifurcations taking place at $\epsilon^H = (a_c(\mu), \mu)$. The bifurcation can be either subcritical and supercritical depending on the relative width variable.

4.4.3 First and Second Order Transitions in a Dichotomously Disordered Population

Before continuing on to the more general case of a uniform distribution, we return to the question of the nature of the bifurcation for the $\mathcal{N} = 2$ dichotomously disordered case. Interestingly, the dichotomously disordered system corresponding to Eqs. (4.8) can undergo either a subcritical or supercritical bifurcation depending on the value of μ characterizing the individual transition rates. The transition to synchrony occurs at a single value of the coupling $a_c(\mu)$ dependent on the relative width parameter, as shown in Section 4.4.1. As such, a and μ are not truly independent parameters, and we can in principle eliminate a and consider μ to be the bifurcation parameter of interest. Then, using the machinery discussed in Section 2.3, it is a straightforward but tedious exercise to numerically evaluate the first Lyapunov coefficient $l_1(\mu)$ corresponding to the Hopf bifurcation occurring at $(\mu, a(\mu))$. As shown in Fig. 4.15, the sign of l_1 varies depending on the relative width parameter (which in turn determines the critical coupling a_c). Hence, the phase transition to synchrony can appear continuous or discontinuous depending on the relative difference between the transition rate parameters in the two populations.

To verify these predictions, we solve the mean field equations numerically in both the subcritical ($\mu = 3/4$) and supercritical ($\mu = 7/4$) regimes. In the former case, we consider the case $\gamma_1 = 2.5$, $\gamma_2 = 5.5$. Fig. 4.16 clearly indicates that the transition to synchrony is marked by a discontinuous change in the order parameter r (here time averaged in the steady state) as a eclipses $a_c \approx 3.55$. In addition, a small region of marked hysteresis appears just below threshold. Remarkably, this indicates that a stable disordered solution coexist with a stable, synchronized solution (the stable limit cycle) just before threshold.

By contrast, the case $\mu = 7/4$ corresponds to a supercritical Hopf bifurcation reminiscent of a continuous phase transition. As shown in Fig 4.17, the transition is characterized by a continuously increasing order parameter; no hysteresis is evident. We note also that the order parameter displays a power law increase near the onset of the bifurcation marked by the mean field critical exponent $\beta = 1/2$. This is expected both from the Hopf bifurcation theorem, which prescribes the $(a - a_c)^{1/2}$ dependence of the

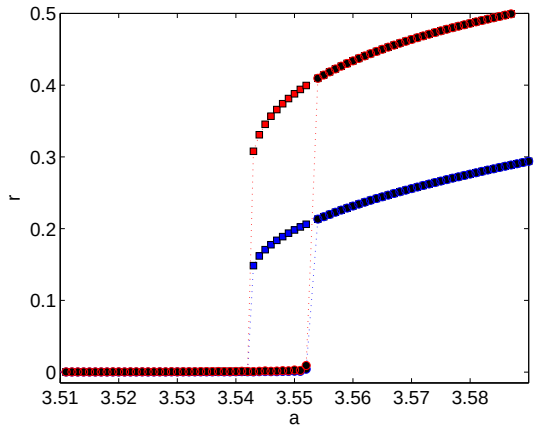

Figure 4.16: A subcritical Hopf bifurcation occurs for $\mu = 3/4$. Squares represent solutions starting from ordered (mostly synchronized) initial conditions, while circles represent solutions starting from disordered (random) initial conditions. Blue points correspond to population one, $\gamma_1 = 2.5$, and red points to population two, $\gamma_2 = 5.5$. The transition is clearly discontinuous as a eclipses $a_c \approx 3.55$. In addition, a region of multistability and corresponding hysteresis exists just below threshold. Solid and dashed lines are drawn to guide the eye.

limit cycle radius (closely related to r, the order parameter) near the onset of synchrony, and also because of the analogy with phase transitions in an infinite-dimensional space (see [8, 9]). Again, we note that the degree of synchronization–as measured by r–is different in the two populations. We further specify the microscopic underpinnings of this difference in Chapter 5.

Interestingly, these results indicate that the degree of spatial disorder may fundamentally alter the nature of the phase transition to synchrony. In both the subcritical and supercritical cases, synchronization is marked by the destabilization of the non-synchronous state at a single value of a_c, giving rise to emergent oscillations in a macroscopic variable (for example, $P_{1,\gamma_i}(t)$). As such, both cases retain the qualitative features of synchronization in disordered populations discussed in this chapter; however, the details of the onset of such cooperation distinguish the two cases. Again we note that this behavior is reminiscent of that seen in a significantly more complicated setting, that of Daido's generalized continuous oscillators [13], where disorder can alter the continuity of the transition.

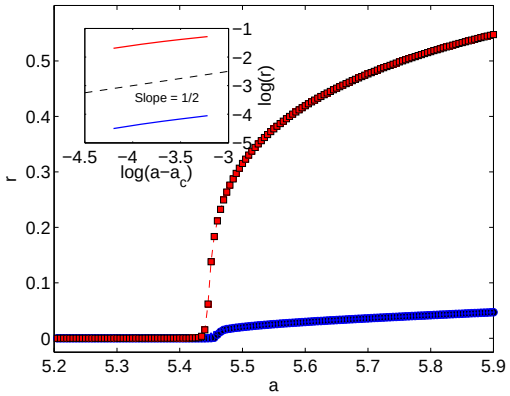

Figure 4.17: A supercritical Hopf bifurcation occurs for $\mu = 7/4$. Squares represent solutions starting from ordered (mostly synchronized) initial conditions, while circles represent solutions starting from disordered (random) initial conditions. Blue points correspond to population one, $\gamma_1 = 0.25$, and red points to population two, $\gamma_2 = 3.75$. The transition is clearly continuous as a eclipses $a_c \approx 5.44$, and there is a noticeable absence of hysteresis. Solid and dashed lines are drawn to guide the eye. The inset indicates that, in the neighborhood of the critical point, the order parameter follows power law behavior with the correct mean field critical exponent ($\beta = 1/2$).

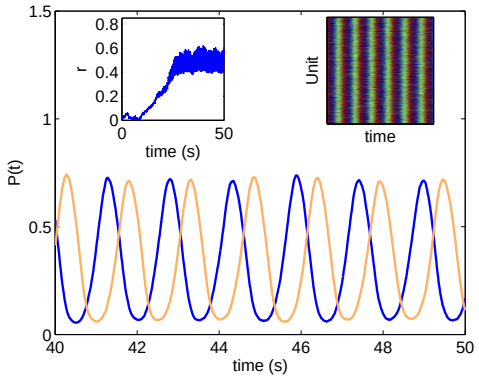

Figure 4.18: The probability that the synchronized array is in state 1 (lighter or brown) and state 2 (darker or blue) as a function of time for a uniform distribution $\varphi(g)$ on the interval $[1.5, 2.5]$ and coupling parameter $a = 3.15$. Insets show the order parameter $r(t)$ as well as time resolved snapshots of the system.

4.5 Uniform Distribution of Transition Rate Parameters

We now turn to globally coupled arrays where the transition rate parameter g for each unit is chosen from a uniform distribution over a finite interval, $\varphi(g)$. While it is difficult to make direct analytical progress in this general case, the earlier dimer analysis and the arrays of $\mathcal{N} = 2, 3, 4$ different populations of units provide a framework for understanding the properties of these more general systems. In particular, the earlier results suggest that this "more disordered" system may also display a single transition to synchronization. To explore these and other features in more detail, we simulate $N = 5000$ globally connected units characterized by the transition rate parameter distribution $\varphi(g)$, and we make several observations. Firstly, we do observe a single transition to macroscopic synchronization. Secondly, as suggested by the dichotomous case, synchronization appears more readily (that is, for a lower value of a) if the distribution $\phi(g)$ has a larger mean and smaller width. When the mean and width are varied independently, the qualitative trends from the dichotomous case are observed here as well. Thirdly, while synchronization in this system is again governed primarily by the mean and width of the distribution $\varphi(g)$, the critical value a_c is considerably lower than that of the finite $\mathcal{N}$ systems with the same mean and width (as expected).

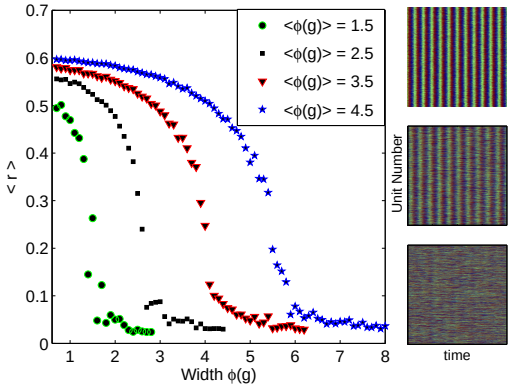

Figure 4.19: As the width of the $\phi(g)$ distribution increases, a critical width is reached beyond which synchronization is destroyed. The coupling is chosen to be $a = 3.2$, and the four curves represent the steady state, time-averaged order parameter for distributions with different means. As the mean of the $\phi(g)$ distribution increases, the transition to disorder occurs at a greater width. The insets at the right show the long-time behavior of an entire population of mean transition rate parameter 3.5 (corresponding to the triangle order parameter data) and widths of 0.6, 4.0, and 6.2.

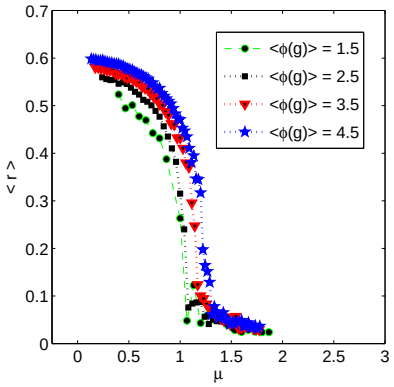

Figure 4.20: The data of Fig. 4.19 against the relative width μ.

Two examples of our simulation results are shown in Figs. 4.18 and 4.19. In Fig. 4.18 we present the first two components of the 3-dimensional vector $\boldsymbol{P}(t)$ whose components $P_i(t)$ represent the probability that all units of the entire synchronized array are in state i. The probabilities $P_1(t)$ and $P_2(t)$ oscillate in time with slightly modulated amplitudes and a constant relative phase, indicating global synchronization. The upper left inset shows the order parameter $r(t)$ and the upper right inset the time resolved snapshot of the system, both indicating a high degree of synchronization. Note that the coupling parameter $a = 3.15$ in the figure is below the critical value $a_c = 3.2$ for the dichotomous case with the same mean and width.

Figure 4.19 shows the steady state time-averaged order parameter r at constant a as the width of the $\phi(g)$ distribution is increased for a fixed mean. Similar to the $\mathcal{N} = 2$ population case, synchronization is destroyed as the width eclipses some critical value, and that value increases as the mean of the distribution increases. In Fig. 4.20 we plot the data from Fig 4.19 as a function of the relative width parameter μ. Recalling that for the dichotomous array as well as for the dimer synchronization at a given a depends only on μ, we might expect that the transition point μ_c (at constant a) is not significantly mean-dependent, even when there is a distribution of transition rate parameters. In fact, we can see that the curves approximately collapse onto one curve, indicating that the relative width μ provides a useful control parameter for predicting synchronization. Hence, the predictions of the linearization analysis for the $\mathcal{N} = 2$ case provide qualitative insight into the behavior of the disordered population.

4.6 Discussion

We have presented a discrete model for globally coupled stochastic nonlinear oscillators with a distribution of transition rate parameters. Our model exhibits a range of interesting dynamical behavior, much of which mimics the qualitative features of the canonical Kuramoto oscillator [3] and even more generalized models [13], but with a mathematically and numerically considerably more tractable model. Since our phase variable is discrete (whereas the phase variable in the canonical problem is continuous), a distribution of $\mathcal{N}$ different transition rates in our array leads to a set of $2\mathcal{N}$ coupled nonlinear *ordinary* differential equations instead of a single *partial* differential equation

for the probability distributions of interest. Linearization of our model around the critical point leads to a problem which at least for small $\mathcal{N}$ (specifically, for the dichotomous disorder case) becomes analytically tractable. Distributions involving a large finite number of transition rate parameters, while not easily amenable to analytic manipulation even upon linearization, reduce to a simple matrix algebra problem. For any distribution of transition rate parameters, even continuous, the model is in any case readily amenable to numerical simulation.

Our most salient conclusion is that such disordered globally coupled arrays of oscillators, even in the face of transition rate parameter disorder, undergo a single transition to macroscopic synchronization marked by a single Hopf bifurcation. This bifurcation can be continuous or discontinuous, but in both cases the asynchronous solution becomes unstable at a single value a_c; that is, there are not multiple bifurcations occurring, for example, within different subpopulations. While the coupling is entirely different in the canonical Kuramoto model and therefore direct comparisons with our model are not straightforward, we note that a single transition involving a single discrete eigenvalue emerging from a continuous spectrum is observed for a continuum of frequencies distributed unimodally and symmetrically [3, 12, 14, 15]. We have also shown that the critical coupling a_c for synchronization in our model depends strongly (but not exclusively) on the width Δ and mean γ of the transition rate parameter distribution, specifically via the relative width $\mu = \Delta/\gamma$. This general feature is already apparent in the synchronization behavior of a dimer of two oscillators with transition rate parameters γ_1 and γ_2. An infinite array of two populations of oscillators, one with transition rate parameter γ_1 and the other with γ_2, displays a Hopf bifurcation, with a_c determined solely by μ. While a quantitative prediction of synchronization on the basis of the relative width is not possible in all cases, it does determine qualitative aspects of the transition for more complex transition rate parameter distributions. We have explored this assertion for arrays with $\mathcal{N} = 2,\ 3$, and 4 and with a uniform distribution of transition rates over a finite interval, and we expect it to be appropriate for other smooth distributions as well. In the Kuramoto model the distribution of frequencies is usually taken to be Lorentzian for analytic tractability, and therefore determined by a single parameter that precludes separate characterization in terms of two parameters (average frequency and width).

In addition, we note the remarkable result that even in the tractable case of $\mathcal{N} = 2$ (dichotomous disorder), the phase transition can switch between continuous and discontinuous depending on the level of disorder. Similar behavior has been seen in generalized continuous oscillators with bimodal frequency distributions [13], hence, it appears our oscillator system produces many complexities seen in significantly more complicated models.

A number of further avenues of investigation based on transition rate disorder in our stochastic three-state phase-coupled oscillator model are in progress. One is the exploration of the effects of transition rate disorder in locally coupled arrays. We have succeeded in fully characterizing such arrays for identical oscillators [8, 9], and would ideally like to extend this full characterization in terms of critical exponents and upper and lower critical dimensions to the case of dichotomous disorder. In the locally coupled system this "simple disorder" scenario is already considerably complicated by the fact that the spatial distribution of the two populations may play a role. In addition, the transition will presumably appear either supercritical or subcritical depending on the distribution of parameters, meaning we can not simply apply the techniques from Chapter 3, which are only appropriate for continuous transitions. In fact, the very nature of critical exponents relies on a continuous scaling of the order parameter near criticality.

Perhaps most importantly, this chapter raises questions regarding the nature of synchronization above threshold. In particular, in the case of dichotomously disordered populations, what exactly is represented–in terms of individual oscillator behavior–by variations in the degree of synchronization between two subpopulations? That is, why does one population show a larger r than the other, given that both are experiencing a coupling greater than a_c required for the Hopf bifurcation? To these questions we turn our attention in Chapter 5. Finally, we note that a two-state version of this model (which of course does not lead to phase synchronization as discussed here) has recently been shown to accurately capture the unique statistics of blinking quantum dots [16]. Such wider applicability of the model, together with its analytic and numerical tractability, clearly opens the door to a number of new directions of investigation.

Acknowledgments

Chapter 4 contains material which appears, in part, in K. Wood, C. Van den Broeck, R. Kawai, and K. Lindenberg, Phys. Rev. E 75 , 041107 (2007).

References

[1] S. H. Strogatz, *Nonlinear Dynamics and Chaos* (Westview Press, 1994).

[2] A. T. Winfree, J. Theor. Biol. **16**, 15 (1967).

[3] Y. Kuramoto, *Chemical Oscillations, Waves, and Turbulence* (Springer, Berlin, 1984).

[4] S. H. Strogatz, Physica D **143**, 1 (2000).

[5] A. Pikovsky, M. Rosenblum, J. Kurths, *Synchronization: A Universal Concept in Nonlinear Science* (Cambridge University Press, Cambridge, 2001).

[6] T. Prager, B. Naundorf, and L. Schimansky-Geier, Physica A **325**, 176 (2003).

[7] H. Sakaguchi, S. Shinomoto, and Y. Kuramoto, Prog. Theor. Phys. **77**, 1005 (1987); H. Daido, Phys. Rev. Lett. **61**, 231 (1988); S. H. Strogatz and R. E. Mirollo, J. Phys. A **21**, L699 (1988); *idem*, Physica D **31**, 143 (1988); H. Hong, H. Park, and M. Choi, Phys. Rev. E **71**, 054204 (2004).

[8] K. Wood, C. Van den Broeck, R. Kawai, and K. Lindenberg, Phys. Rev. Lett. **96**, 145701 (2006).

[9] K. Wood, C. Van den Broeck, R. Kawai, and K. Lindenberg, Phys. Rev. E **74**, 031113 (2006).

[10] T. Risler, J. Prost, F. Jülicher. Phys. Rev. Lett. **93**, 175702 (2004).

[11] T. Risler, J. Prost, and F. Jülicher, Phys. Rev. E **72**, 016130 (2005).

[12] Acebron, J., L. Bonilla, C. Perez Vicente, F. Ritort, and R Spigler. Rev. Mod. Phys. **77**, 137 (2005).

[13] H. Daido. Physica D **91**, 24-66 (1996); Phys. Rev. Lett **73**, 760 (1994).

[14] S. H. Strogatz, R. E. Mirollo, and P. C. Matthews, Phys. Rev. Lett. **68**, 2730 (1992).

[15] N. J. Balmforth and R. Sassi, Physica D **143**, 21 (2000).

[16] S. Bianco, E. Geneston, P. Grigolini, and M. Ignaccolo, arXiv:cond-mat/0611035 (2006).

5

Synchronization Above Threshold in Discrete Phase Coupled Oscillators

5.1 Introduction

Following our analysis of synchronization in a variety of contexts in Chapters 2-4, we conclude this part of the thesis with an analysis of the microscopic underpinnings of synchronization above threshold in collections of globally coupled oscillators. We have seen that macroscopic synchronization–distinguished by the onset of oscillations in a macroscopic quantity (e.g. P_i) owing to a Hopf bifurcation–does not always occur by the same mechanisms. The transition can be continuous or discontinuous, depending on both microscopic features of the model and the level of transition rate disorder in the system. In addition, a value of $r < 1$ indicates that synchronization is not perfect, meaning that all oscillators are not in phase at all times. In this chapter, we explore the microscopic foundations of this suprathreshold synchronization. In particular, we calculate the time-averaged frequencies of individual oscillators and explore the relationship between this quantity and the level of phase synchronization for coupling a above the critical threshold a_c. We do this for a specific model (both in single and dichotomously disordered populations), but the principal results should hold for all U,V, and W that

give a Hopf bifurcation. In fact, only the nature of the bifurcation (near a_c) is affected by the choice (U, V, W), and this chapter primarily deals with oscillators above threshold and beyond any potential regions of hysteresis. That said, we note that as we move far above threshold, other choices (U, V, W) with $W \neq 0$ would lead to an anomalous speeding or slowing of all oscillators, but given that the results of this analysis pertain to slightly above threshold phenomena and furthermore, that this speeding or slowing would affect all oscillators equally, it should in no other way affect the conclusions reached here.

5.2 The Model

We begin by considering a stochastic three-state model governed by transition rates g, where each state may be interpreted as a discrete phase [2, 3, 4]. Because the transitions among states are unidirectional and do not conform to deterministic rate laws, the model retains a qualitative link with a noisy phase oscillator.

Once again we couple individual units by allowing the transition rates of each unit to depend on the states of the units to which it is connected. In this chapter, for N identical units we choose the transition rate of a unit ν from state i to state $i+1$ as

$$g_i = g \exp\left[\frac{a(N_{i+1} - N_{i-1})}{n}\right], \tag{5.1}$$

where $i = 1, 2, 3$ and $i+1 = 1$ with $i = 3$, a is the coupling parameter, g is the transition rate parameter, n is the number of oscillators to which unit ν is coupled, and N_k is the number of units among the n that are in state k. As in Chapter 4, we choose a model corresponding to $(U, V, W) = (1, -1, 0)$ to prevent the physically unrealistic speeding or slowing of macroscopic oscillations as we move farther from threshold. Each unit may thus transition to the state ahead or remain in its current state, and the propensity for such a change depends on the states of the units to which it is coupled. Here we focus entirely on globally coupled arrays, $n \to N - 1$, with N sufficiently large that $N_j/(N-1) \to P_j$.

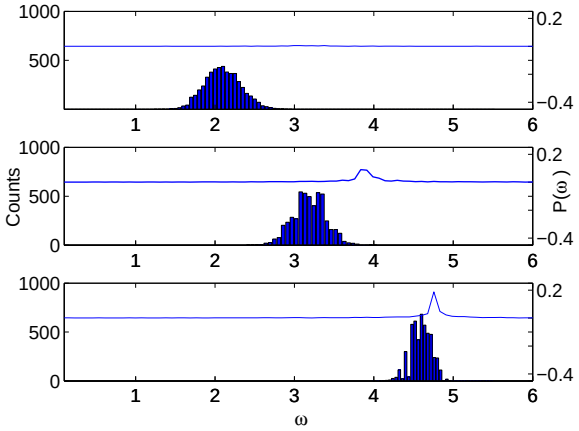

Figure 5.1: Each plot shows a histogram of time-averaged frequencies (in the steady state), where the vertical axis represents the number of units (out of $N = 3500$ total units) having the frequency $\bar{\omega}$. The power spectrum of P_{1,γ_1} (blue) overlays each histogram. The top panel is below synchronization threshold ($a = 2.65$), the while the middle ($a = 3.05$) and lower panels ($a = 3.45$) are both above threshold.

5.3 Microscopic Underpinnings of Synchronization

Having shown that synchronization might arise via both continuous and discontinuous transitions, we now explore in detail the microscopic subtleties underlying synchronization above threshold. As detailed in [2, 3, 4] and mentioned above, synchronization occurs in the mean field limit via the destabilization of a nonsynchronous fixed point. Specifically, a single pair of complex conjugate eigenvalues corresponding to the linearized fixed point cross the imaginary axis at a_c, giving rise to stable oscillations in the macroscopic variables characterizing the system (in our case, the components of $\boldsymbol{P}(t)$). While the onset of this behavior is dependent on the choice (U, V, W) and also the degree of disorder within the system (see Chapters 2 and 4), the qualitative features of the synchronized state remain identical above threshold in both the subcritical and supercritical cases, so long as we do not approach the infinite coupling limit. Hence, we limit our attention to several illustrative cases, but note that our results hold also for the supercritical case (and in fact the entire range of μ). Specifically, in what follows, we take $(U, V, W) = (1, -1, 0)$ and consider a single population as well as a dichotomously disordered population with $\mu = 3/4$.

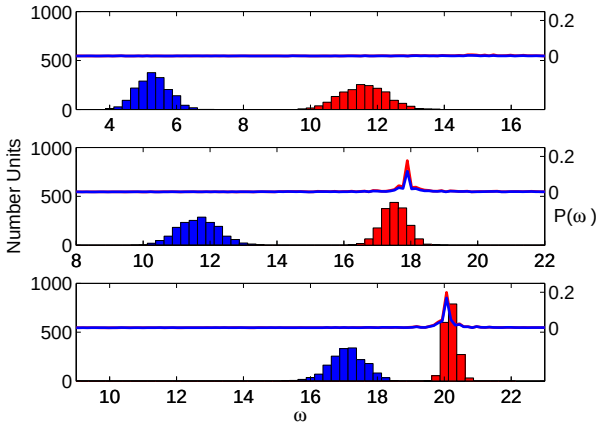

Figure 5.2: Each plot shows a histogram of time-averaged frequencies (in the steady state), where the vertical axis represents the number of units (out of $N = 3500$ total units) having the frequency $\bar{\omega}$. Population one, characterized by $\gamma_1 = 2.5$, is represented by a dark shade (blue), while population two, characterized by $\gamma_2 = 5.5$, is represented by a light shade (red). Power spectra of P_{1,γ_1} (dark or blue) and P_{1,γ_2} (light or red) overlay the histograms. The top panel is below synchronization threshold ($a = 3.20$), while the middle ($a = 3.60$) and lower panels ($a = 3.86$) are just above threshold. For esthetic purposes, the horizontal range is not chosen identically for all three panels, but the size of the range remains the same in each plot.

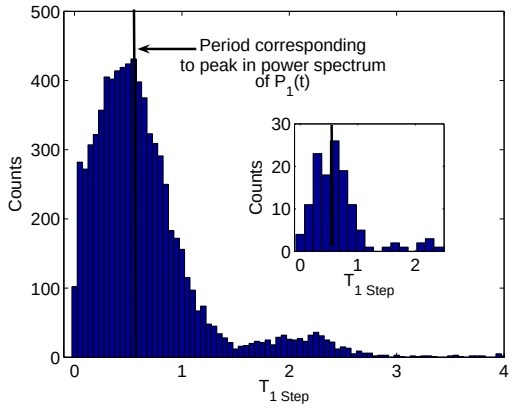

Figure 5.3: The central figure shows a histogram of step times T_{1step} for a sampling of $N = 60$ units once the steady state has been reached. The vertical black line indicates the step time corresponding to the peak in the power spectrum of $P_1(t)$ (that is, the step time corresponding to the frequency of the macroscopic oscillations). The insets show similar histograms for a single unit $a = 3.05$ (above threshold), $\gamma = 1$ in all plots.

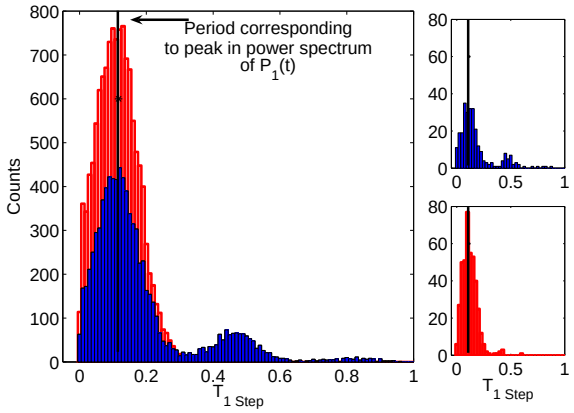

Figure 5.4: The central figure shows a histogram of step times T_{1step} for a sampling of $N = 30$ units from each population once the steady state has been reached. The light shade (blue) represents population one, while the light shade (red) represents population 2. The vertical black line indicates the step time corresponding to the peak in the power spectrum of $P_1(t)$ (that is, the step time corresponding to the frequency of the macroscopic oscillations). The insets show similar histograms for single units; the top histogram is for a unit from population one, the bottom from population two. $a = 3.60$ (above threshold), $\gamma_1 = 2.5$, and $\gamma_2 = 5.5$ in all plots.

In particular, threshold a_c is marked by the onset of coherent temporal oscillations in the components of $\boldsymbol{P}(t)$. We characterize the microscopic underpinnings of these oscillations by considering $\bar{\omega}_i$, the time-averaged frequency of oscillator i in the steady state. We perform simulations on globally coupled lattices of $N = 3500$ units of a single population with $\gamma = 1$ and also of a dichotomously disordered population with $\gamma_1 = 2.5$ and $\gamma_2 = 5.5$. As shown in Figs. 5.1, 5.2, the distribution of frequencies $\bar{\omega}_i$ clusters around the values prescribed by γ (or γ_1 and γ_2 for populations one and two, respectively) far below threshold (top panels). Specifically, for a deterministic oscillator with transition rate γ, $\bar{\omega}_i$ is given by $2\pi\gamma/3$; when $\gamma = 1$ (or $\gamma_1 = 2.5$ and $\gamma_2 = 5.5$), this gives the central peak of the histogram for the relevant population. As threshold is eclipsed (middle panels), a peak arises in the power spectrum of the macroscopic variable P_{1,γ_i}, though the frequency of this peak does not correspond with the individual $\bar{\omega}_i$'s of oscillators constituting the population. In the dichotomous case, this peak only roughly corresponds with the time averaged frequencies from population two and completely exceeds even the maximum $\bar{\omega}_i$ characterizing population one. As a is further increased, the discrepancy between the time-averaged frequency histograms and the macroscopic oscillation frequencies decreases. In addition, in the disordered case, the histograms for the two populations become increasingly narrow and closer to one another (bottom panel). We note that as a becomes tremendously large, the histograms become extremely narrow and begin to overlap at a frequency determined by the frequency of the macroscopic oscillations, as expected (indicative of perfect synchronization). Nonetheless, the behavior for finite, intermediate a is quite counterintuitive and points to a rich microscopic dynamics underlying the cooperative behavior.

To further explore these trends, we consider the stochastic variable $T_{1\ step}$, the waiting time in a single state for an individual oscillator. $T_{1\ step}$ represents the time the oscillator spends in a single state i before transitioning to the subsequent state $i + 1$. For computational efficiency, we record $T_{1\ step}$ for a representative subpopulation of 60 units (30 units from each population, one and two, in the disorder case). Figs 5.3, 5.4 show histograms of the variable $T_{1\ step}$ taken over this representative subpopulation once steady state was reached. Clearly, all relevant subpopulations consist of oscillators whose steps most often correspond to the frequency of the macroscopic oscillation (shown by the solid vertical line). That is, the peak of the histograms occur at a value T

comensurate with the frequency peak in the power spectrum of the components of $\boldsymbol{P}(t)$. However, Fig 5.3 shows that the distribution of $T_{1\ step}$ is bimodal, with a significant peak occurring at $T_{1\ step} \approx 2.2$ which downward biases the time-averaged frequencies ω_i of individual units. We note that as coupling a increases significantly above threshold, the distribution becomes unimodal with a peak at $T_{1\ step}$ corresponding to the frequency of macroscopic oscillation. In the disordered case, only population one, characterized by significantly lower time-averaged $\bar{\omega}$'s, shows a bimodal distribution with a significant peak at $T_{1\ step} \approx 0.45$. In fact, these long wait times–while not the dominant macroscopic behavior–pervade the microscopic dynamics in such a way that the time-averaged frequencies become downward biased and no longer accurately represent the macroscopic dynamics. Interestingly, population two has become sufficiently synchronized that the second peak is effectively nonexistent, and thus the frequencies overlap more closely with the macroscopic "mean field" frequency. The right insets of Figs 5.3, 5.4 show histograms for single units chosen from the populations (or subpopulations). Again, the unit chosen from the single population case shows a bimodal distribution with significant "anomalous" peaks near $T_{1\ step} \approx 2.2$. In the disordered case, the unit from population one shows a bimodal waiting time distribution characterized by occasional wait times in the neighborhood of $T \approx 0.45$ in addition to those corresponding to the macroscopic oscillations. Finally, in Fig 5.5, we show the time evolution of the subpopulations along with the macroscopic variable P_{1,γ_i} for each population. At any given point in time, the majority of oscillators in each population are synchronized, leading to the smooth oscillations of the macroscopic variable. However, isolated single units are prone to long waiting times, particularly in the less synchronized population (population one, left panel, in this example). These anamolously long waiting times, which serve to bias the time averaged frequencies $\bar{\omega}_i$ of each individual unit, nevertheless do not substantially disrupt the macroscopic oscillations, largely because the occurence of coincident long waits is fairly uncommon. That is, the long waiting times do not appear in any significantly correlated way among individual constituents of the population.

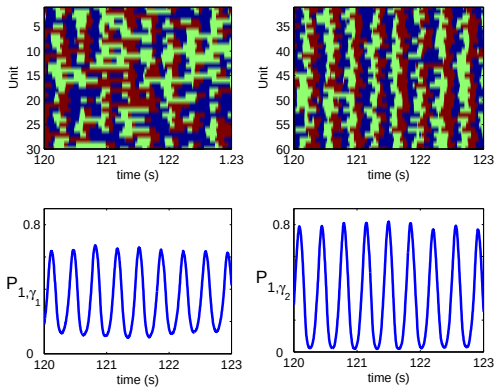

Figure 5.5: The top panels show the evolution of a representative sub-system ($N = 30$ units of each population). The three shades of color (blue, green, and red) represent states 1,2, and 3, respectively. The bottom panels show the macroscopic variable P_{1,γ_i} for each population. The left panels show correspond to population one ($\gamma_1 = 2.5$), while the right panels correspond to population two ($\gamma_2 = 5.5$). $a = 3.60$ (above threshold) for all plots.

5.4 Discussion

In this concluding chapter of Part I, we study the microscopic basis of phase synchronization above threshold. It is initially counterintuitive that phase synchronization, defined in terms of the Hopf bifurcation and temporal oscillations in the macroscopic variable $\boldsymbol{P}(t)$ (and measured in the order parameter r), is not contingent upon the existence of overlapping distributions of $\bar{\omega}_i$. That is, our results regarding the discrete oscillator model highlight the complexity of microscopic dynamics underlying macroscopic cooperation and point to a potentially misleading subtlety. Whereas phase synchronization is often considered a stronger condition than frequency entrainment–defined using an order parameter built upon the notion that a fraction of units display identical time-averaged frequencies in the oscillator population–we here report subtle microscopic features which distinguish the two without establishing a clear hierarchy. For example, Hong et al [6] show that for disordered populations of Kuramoto oscillators, the lower critical dimension for frequency entrainment is lower than that for phase synchronization in locally coupled oscillators, indicating the relative ease with which frequency entrain-

ment is achieved. They note that the two transitions coincide in the case of globally coupled units. Contrast that with our dichotomously disordered population, for which phase synchronization occurs without any overlap in the frequency distributions: that is, no oscillator from population one has the same frequency as any oscillator from population two. While a direct comparison is not plausible owing to the specific differences between models and order parameters, we stress that any order parameter related to time-averaged measurements of frequencies would be misleading and provide, for our model, potentially counterintuitive results. The emergence of a nonzero r, which measures phase synchronization, corresponds with the loss of stability of the asynchronous fixed point (the Hopf bifurcation). This does not guarantee similar distributions of time-averaged frequencies in the two populations; in fact, we can readily see that synchronization occurs while the frequency distributions are entirely distinct. Furthermore, the frequency of the macroscopic oscillations of the mean field does not always coincide with the time-averaged frequencies of the oscillators constituting the population (or any subpopulation). Only when coupling is sufficiently large to substantially reduce the anamolously long waiting times which bias $\bar{\omega_i}$ will the frequency distributions begin to overlap one another and coincide with the frequency of the mean field oscillations. Because these long waiting times appear more readily in the population with the smaller γ_i, the time-averaged frequencies of the two populations are disproportionately affected, meaning that the populations will appear to behave quite differently in terms of average frequency. This in fact underlies the stark differences in the degree of synchronization between two populations as measured by the order parameter r (see Chapter 4 for examples), and provides an intuitive description capable of explaining this discrepancy. Our previous results show that completely disordered populations show qualitative similarities with the dichotomously disordered case [4]; hence, we are led to cautiously speculate that wholly disordered populations are also characterized by waiting times $T_{1\ step}$ distributed with long tails, and hence time-averaged frequencies become downwardly biased, meaning that the order parameter for frequency entrainment, in the typical sense, will not accurately reflect the macroscopic cooperation. Further studies along these lines are currently in progress.

Finally, the results of this chapter raise the following question: how dependent is the above phenomenon on the choice of a discrete phase model? Would similarly

counterintuitve results arise in continous phase oscillators? In fact, a recent study by Rosenblum and Pikovsky [7] suggests that a similar–though not identical–state of partial synchronization arises in continous oscillators coupled in a highly nonlinear fashion. Specifically, they find that in globally coupled oscillators, phases exist in which certain subpopulations are characterized by time-averaged frequencies which are not commensurate with the oscillations of the mean field–that is, they are not locked with the macroscopic oscillations induced in the population. While once again the differences between the models make direct comparison difficult, it is nevertheless clear that measurements of time-averaged frequencies provide potentially counterintuitive results, even in globally coupled arrays. In the case of our stochastic discrete oscillators, the behvavior is quite transparent once viewed in terms of $T_{1\ step}$, though it is not clear whether a similar mechanism underlies the phenomenon in the continous phase model. Uncovering the relationship between the superthreshold phase in our model and that in the continous oscillator model of [7] remains an open question, but even the superficial similarities between the results motivate continued efforts along these lines.

Acknowledgments

Chapter 5 contains material which appears, in part, in K. Wood, C. Van den Broeck, R. Kawai, and K. Lindenberg, in preparation (2007).

References

[1] H. Daido. Physica D **91**, 24-66 (1996); Phys. Rev. Lett **73**, 760 (1994).

[2] K. Wood, C. Van den Broeck, R. Kawai, and K. Lindenberg, Phys. Rev. Lett. **96**, 145701 (2006).

[3] K. Wood, C. Van den Broeck, R. Kawai, and K. Lindenberg, Phys. Rev. E **74**, 031113 (2006).

[4] K. Wood, C. Van den Broeck, R. Kawai, and K. Lindenberg Phys. Rev. E 75 , 041107 (2007).

[5] Yu. A. Kuznetsov, *Elements of Applied Bifurcation Theory*, 2nd ed. (Springer, New York, 1998).

[6] H. Hong, H. Park, and M. Choi, Phys. Rev. E **71**, 054204 (2004); H. Hong, H. Park, and M. Choi, Phys. Rev. E **72**, 036217 (2005).

[7] M. Rosenblum and A. Pikovsk. Phys. Rev. Lett **98**, 064101 (2007).

Part II

Noise-Induced Phase Transitions

6

Noise-induced Phase Transitions and Relaxational Models

6.1 Introduction

In Part I of this thesis, we have studied collective behavior in large populations of coupled oscillators, paying particular attention to the role of temporal dynamics and the analogy with nonequilibrium phase transitions. We have seen that coupling between individual oscillators can be made sufficiently strong so as to overcome the inherent randomness in their individual dynamics and even quenched disorder within the population itself. We now turn our attention to a different type of collective behavior in large nonequilibrium systems, that *induced* by stochasticity. While maintaining many parallels with Part I, including the reliance on simple phenomenological models, we distinguish this second Part by its dependence on a common theme: the ordering role of randomness in nonequilibrium spatially extended systems.

6.2 The Order in Randomness

The concept of noise traditionally conjures images of disruption, as it is often regarded as a background pollutant which unravels the natural order afforded by purely deterministic dynamics. In fact, on a mesoscopic scale–where quantum fluctuations can be safely neglected–the very underpinning of stochastic modeling arises from an assumed

ignorance, or perhaps more appropriately, an admitted theoretical defeat, at the hands of a complex dynamical interplay between a large system's many degrees of freedom. While systematically monitoring the dynamics of a physical system's individual constituents becomes quickly intractable with increasing system size, the concept of a thermodynamic limit affords the theoretician the mathematical justification for appealing to statistical concepts, and in some settings one can replace a host of deterministic variables with a manageable set of stochastic, relevant degrees of freedom [1, 2]. The price of such a drastic reduction is the introduction of purely probabilistic noise terms, and the ubiquity of this approach has made popular the further mathematical investigation of the effects these terms have on dynamical systems. Furthermore, the natural physical connection between statistical concepts and many macroscopic systems as elucidated in the classical theories of statistical mechanics and thermodynamics lends credence to the utility of the non-deterministic approach and contributes largely to its wide-spread appeal in modern theoretical physics.

Remarkably, recent studies have highlighted the counterintuitive effect noise can have on nonlinear systems. In particular, many works have pointed to the qualitative changes in dynamical behavior induced purely by conceptually uninteresting "white" noise (see, for example, [3, 4]). Such noise-induced transitions, even those limited to zero-dimensional systems, provide striking evidence that stochasticity, when combined with nonlinearity, offers a rich dynamic phenomenology far exceeding the bland superposition of statistically regular fluctuations upon predictable macroscopic dynamics. When further decorated with spatial degrees of freedom, the interplay between noise and nonlinearity yields the potential for genuine non-equilibrium phase transitions, where extended phases exist and can be characterized using notions and techniques from the corresponding equilibrium theory.

Van den Broeck *et al.* [5] introduced the first example of a purely noise-induced phase transition by positing the existence of a spatially dependent local order parameter, here called $\varphi(\bar{r})$, whose dynamics evolve under the combined influence of a judiciously chosen nonlinearity and multiplicative noise. The spatial and temporal steady state average of the order parameter, taken over the entire system (which is assumed very large), distinguishes between the ordered ($|\langle\varphi\rangle| \neq 0$) and disordered ($\langle\varphi\rangle = 0$) phases. As the intensity of the noise is increased, an instability in the local dynamics creates a tran-

sient, locally-ordered state which, in the presence of sufficiently strong coupling, becomes self-reinforcing and leads to a macroscopically ordered phase. This transition shares commonalities with traditional equilibrium phase transitions, including a diverging correlation length and a peak in fluctuations at the critical noise intensity, but nonetheless relies on a particular mathematical interpretation of the noise and, furthermore, is dynamic in origin; the phase transition cannot be traced back to a nonequilibrium effective potential which is fundamentally altered by tuning the control parameter.

Following this seminal work, Ibanes *et al.* later introduced a class of models whose steady state probability distribution–and hence also the nonequilibrium effective potential–can be found exactly, eliminating the need for a dynamic explanation of the noise-induced phase transition. Inspired by the inverted phase diagrams seen in certain polymer blends, Ibanes *et al.* modify a generic model for the relaxational flow of a field $\varphi(\bar{r})$, here corresponding to a local order parameter, in a potential to include field-dependent kinetic coefficients. Specifically, the dynamics of $\varphi(\bar{r})$ is given by

$$\dot{\varphi}(\bar{r},t) = -\Gamma[\varphi(\bar{r},t)]\frac{\delta\mathcal{F}[\varphi(\bar{r},t)]}{\delta\varphi(\bar{r},t)} + \Gamma[\varphi(\bar{r},t)]^{1/2}\xi(\bar{r},t) \tag{6.1}$$

where we use square brackets to indicate a functional, $\Gamma[\varphi(\bar{r},t)]$ is the field-dependent kinetic coefficient, $\mathcal{F}[\varphi]$ is an energy functional that depends on both a local potential $V[\varphi]$ and subsystem interaction terms, and ξ is zero mean Gaussian white noise with correlation

$$\langle\xi(\bar{r},t)\xi(\bar{r}',t')\rangle = \sigma^2\delta(\bar{r}-\bar{r'})\delta(t-t'). \tag{6.2}$$

σ^2 is a control parameter which measures the intensity of the fluctuations. The form of Eq. (6.1) is dictated by a Fluctuation-Dissipation relation which constrains the form of the multiplicative noise term. The steady state probability distribution $P_{st}[\varphi]$ takes an exponential form

$$P_{st}[\varphi] \propto e^{-2V_{eff}/\sigma^2}, \tag{6.3}$$

where V_{eff} is an effective potential parametrically dependent on both a spatial coupling parameter (which we later introduce and call K) and σ^2. The existence of such a nonequilibrium effective potential and its qualitative change with the varied control parameter–a change which underlies the mechanism of the phase transition–distinguish these noise-induced transitions from those in [5] and liken them to spatially extended analogs of the zero-dimensional transitions.

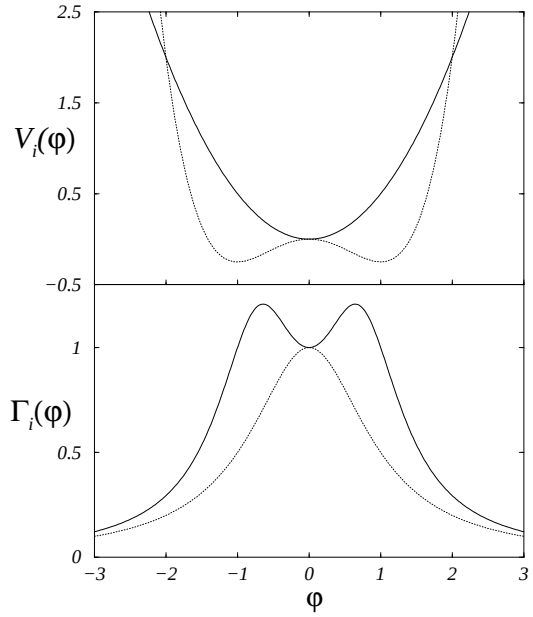

Figure 6.1: Generic local potentials $V_i(\varphi)$ and field-dependent coefficients $\Gamma_i(\varphi)$ as a function of the field φ. Because the asymptotics of these functions is determined by physical constraints, there are only two qualitative forms (represented by $i = 1, 2$) taken by these functions as dictated by the convexity at the origin. The solid lines represent $i = 1$, and the dotted lines $i = 2$. Specifically, the second derivatives (evaluated at the origin) can be either positive or negative for each function. Here we show specific functional examples, but stress that differences in scaling that do not affect the geometry near the origin are of no consequence for the determination of phase diagrams.

6.3 Phase Transitions in Relaxational Models

The relaxational models with field-dependent coefficients such as those in [6] are generalizations of those seen often in the study of dynamic critical phenomena [7]. In addition to the symmetries that underlie universality in static critical phenomena, universal behavior in dynamic quantities such as transport coefficients depends on a host of additional ingredients, including known conservation laws. Many relaxational models in common use offer toy examples embedded with the requisite symmetry and dynamic requirements but otherwise stripped of complex microscopic details which may lead to needlessly complicated relaxation dynamics. Indeed, the models typically rely on the existence of a Lyapanov type functional whose global minima coincide with steady-state dynamics. Relaxational dynamics, including those prescribed in [6], often rely on the simplest possible (gradient) relaxational flow combined ad hoc with stochastic fluctuations that both maintain equilibrium-like fluctuation dissipation relations and also assure the eventual descent to a global minimum of the Lyapanov functional. Thus, we once again appeal to the notion that microscopic details–while important for specific applications and small systems–are less important than maintaining macroscopic symmetries and qualitative behavior, hence allowing us to study phenomenological models.

In addition to their general kinship with archetypical relaxational models in equilibrium, the models with field-dependent coefficients introduced in [6] can be taken as simplified prototypes for a class of noise-induced phase transitions out of equilibrium. Because their analytical tractability affords an intuitive interpretation of the phase transition, these models are ideal for the study of a host of novel noise-induced spatial phenomena, including static pattern formation and global oscillatory behavior. We note that the models can be physically connected with inverted phase diagrams in polymer blends [6, 9], where the high temperature phase is macroscopically ordered and the low temperature phase disordered. However, our purpose is to elucidate novel noise-induced phenomena in these models, not specify the exact physical setting in which these phenomena will occur. Thus, we take these models as generic toy examples of complex phenomena and aim to study in depth the interplay between stochastic, nonlinear, and inhomogeneous spatial dynamics present even in these reduced schemes. Before continuing with specifics, we note here that the models in question which undergo continous

transitions reduce to a Ginzburg-Landau form upon expansion of the field–at least to the lowest (relevant) orders–and hence we do not focus on universality classes of these models. In fact, it has been shown [6] that the continous noise induced transitions do, indeed, belong to the expected Ising class associated with Ginzburg-Landau dynamics.

While several studies have settled on specific functional forms for the kinetic coefficients $\Gamma[\varphi]$ and the local potential $V[\varphi]$ and studied transitions to both homogenous [6] and spatially-ordered [8] phases, Buceta and Lindenberg [10] focused on homogenous phases but considered the case with general $\Gamma[\varphi]$ and $V[\varphi]$. Using a series of analytical and symmetry arguments, they show that four phase diagrams are possible depending solely on the geometric properties of $V[\varphi]$ and $\Gamma[\varphi]$ near the origin in φ-space. As such, [10] provides a comprehensive treatment of phase transitions to homogenous phases in these relaxational systems and offers the geometric architecture for studying other noise-induced phenomena occurring in this general class of models. In what follows we briefly review the analytical results from [10] and then extend the theory based primarily on numerical and steady-state analytical arguments to include general pattern-forming systems [11] (Chapter 7) and transitions to globally oscillating phases [12, 13] (Chapter 8). Finally, in Chapter 9, we develop a mean field analytical treatment capable of dealing with transient dynamics in these general models, thereby yielding a simplified dynamical description capable of dealing with time-dependent phenomena.

It is convenient to consider a discretized version of Eq. (6.1), defined on a d-dimensional cubic lattice as

$$\dot{\varphi}_i(t) = -\Gamma(\varphi_i)\frac{\delta\mathcal{F}(\varphi_i)}{\delta\varphi_i(t)} + \Gamma(\varphi_i(t))^{1/2}\xi_i(t) \tag{6.4}$$

where we take $\Gamma(\varphi) \geq 0$, $\phi_i \equiv \phi_1, ..., \phi_N$, $i = 1, ..., N$, the noise terms are uncorrelated Gaussian variables with correlation functions

$$\langle \xi_i(t)\xi_j(t')\rangle = \sigma^2\delta_{ij}\delta(t-t'), \tag{6.5}$$

and $\mathcal{F}$ depends on a local potential $V(\varphi_i)$ and a diffusive coupling

$$\mathcal{F}[\varphi] = \sum_i \left(V(\varphi_i) + \frac{K}{4d}\sum_{\langle ij\rangle}(\varphi_j - \varphi_i)^2 \right). \tag{6.6}$$

The leftmost sum in Eq. (6.6)runs over all lattice sites while the rightmost sum spans all nearest neighbors of site i on a d-dimensional hypercubic lattice. Following [10], we focus

on the coupling shown in Eq. (6.6) for the development of the analytic formalism, but later extend these results to deal with morphological instabilities giving rise to spatial structure (Chapter 7). To be explicit, we implement the functional derivative in Eq. (6.4) to arrive at

$$\dot{\varphi}_i(t) = \Gamma(\varphi_i)\left(-\frac{\partial V(\varphi_i)}{\partial \varphi_i} + \mathcal{L}\varphi_i\right) + \Gamma(\varphi_i(t))^{1/2}\xi_i(t), \tag{6.7}$$

with $\mathcal{L}$ the coupling operator which, given the form of Eq. (6.6), becomes a discrete diffusion operator,

$$\mathcal{L}\varphi_i = \frac{K}{2d}\sum_{\langle ij\rangle}(\varphi_j - \varphi_i). \tag{6.8}$$

Starting from a mean field treatment of Eq (6.7), Buceta *et al.* show that for functions $\Gamma(\varphi)$ and $V(\varphi)$ of even parity (a condition required to preserve the disordered $\langle\varphi\rangle = 0$ phase of the model), only four possible phase diagrams exist, each consisting of some combination of (stable) ordered ($\langle\varphi\rangle \neq 0$), (stable) disordered ($\langle\varphi\rangle = 0$), and multistable phases. While we do not repeat the details of these calculations, we briefly mention the results and stress that the nature of the phase diagram relies entirely on local geometric properties of the functions $\Gamma(\varphi)$ and $V(\varphi)$, specifically, on the balance of convexities near the origin. Consequently, only two generic types of each function exist, as shown in Fig 6.1, meaning that the qualitative panorama of potential phase diagrams is limited to four choices. A series of analytical and plausibility arguments lead in turn to four possible phase diagrams (given in [10], which are verified numerically in the mean field limit [10]. We delay until the subsequent chapter a detailed discussion of the phase diagrams, as we shall see formally identical examples when the focus turns to pattern forming systems.

A mean field treatment of Eq (6.7) involves replacing the sum over nearest neighbors with a uniform, mean field with must be chosen self-consistently. We have

$$\frac{1}{2d}\sum_{\langle ij\rangle}\varphi_j(t) \to \langle\varphi(t)\rangle \equiv \varphi_0(t), \tag{6.9}$$

a relation which strips the problem of its spatial dependence and leads to the following set of two equations, fully specifying the problem:

$$\begin{aligned}\dot{\varphi}(t) &= \Gamma(\varphi)\left(-\frac{\partial V(\varphi)}{\partial \varphi} + K(\varphi_0(t) - \varphi)\right) + \Gamma(\varphi(t))^{1/2}\xi(t),\\ \varphi_0(t) &= \int_{-\infty}^{\infty} d\varphi\rho(\varphi, t; \varphi_0)\varphi.\end{aligned} \tag{6.10}$$

Here $\rho(\varphi, t; \varphi_0)$ is the probability distribution for φ which, because of the mean field treatment, is parameterized by φ_0. The second equation in (6.10) assures that φ_0 is chosen self-consistently. For now we limit ourselves to the stationary distribution $\rho_{st}(\varphi; \varphi_0)$, easily found to be

$$\rho_{st}(\varphi; \varphi_0) = N(\varphi_0)\Gamma(\varphi)^{(\alpha-1)} e^{-(2/\sigma^2)(V(\varphi)+K/2(\varphi_0-\varphi)^2)}, \tag{6.11}$$

where $N(\varphi_0)$ is the normalization constant and $\alpha = 0$ ($\alpha = 1/2$) corresponds to the Itô (Stratonovich) interpretation of the noise. As the phase transition does not qualitatively rely on a particular interpretation of the noise, we typically choose $\alpha = 0$ for simplicity. The primary arguments for the structure of the phase diagrams, and the nature of the phase transitions between different phases, rely on a qualitative analysis of the possible solutions φ_0 predicated on a geometric interpretation of Eqs. (6.10). Further quantitative results can be obtained by analyzing the stability of the disordered solution ($\varphi_0 = 0$), which turns out to depend only on cumulants of the probability density $\rho_{st}(\varphi, 0)$. Combined with rigorous analysis in the large and small coupling limits and clever plausibility arguments in the intermediate regimes, this analysis yields the phase diagrams, which are verified numerically [10]. While we defer to [10] for the full details, we will utilize specific tools from this analysis in the subsequent extension of the work to pattern-forming systems (Chapter 7). For now, we stress only that four possible phase diagrams exist, and the nature of the phase diagram is wholly determined by the sign of the derivatives of $V(\varphi)$ and $\Gamma(\varphi)$ near the origin. The four diagrams contain regions of stable ordered, stable disordered, and multistable phases, and transitions between phases can be continuous or discontinuous. We provide specific examples in the context of pattern formation in the subsequent chapter.

6.4 Discussion

With a firm conceptual background in hand, we now consider relaxational models leading to a range of novel noise-induced phase transitions which include pattern-formation and time-dependent oscillatory dynamics. Chapter 7 utilizes the machinery developed in [10] and outlined above to explore noise-induced phase transitions to spatially structured, time-independent phases. Chapter 8 considers the emergence of noise-

induced oscillatory dynamics in systems with an added degree of freedom and finally, Chapter 9 includes a further analytical treatment capable of dealing with both transient and time-dependent phases. Taken together, these chapters represent an analytically and numerically complete view of known noise-induced phase transitions in prototype models of relaxational systems with field-dependent relaxational coefficients.

References

[1] C. W. Gardiner, *Handbook of Stochastic Methods* (Springer-Verlag, Berlin, 1983).

[2] N. G. van Kampen, *Stochastic Processes in Physics and Chemistry* (Elsevier, Amsterdam, 1992).

[3] J. García-Ojalvo and J. M. Sancho, *Noise in Spatially Extended Systems* (Springer, New York, 1999).

[4] W. Hosthemke and R. Lefever, *Noise Induced Transitions: Theory and Applications in Physics, Chemistry and Biology* (Springer, Berlin, 1984).

[5] C. Van den Broeck, J. M. R. Parrondo, and R. Toral, Phys. Rev. Lett. **73**, 3395 (1994); C. Van den Broeck, J. M. R. Parrondo, R. Toral, and R. Kawai, Phys. Rev. E **55**, 4084 (1997).

[6] M. Ibañes, J. García-Ojalvo, R. Toral, and J. M. Sancho, Phys. Rev. Lett. **87**, 020601 (2001).

[7] P.C. Hohenberg and B.I. Halperin. Rev. Mod. Phys. **49**, 435 (1977).

[8] J. Buceta, M. Ibañes, J. M. Sancho, and K. Lindenberg, Phys. Rev. E **67**, 021113 (2003).

[9] H.L. Snyder, P. Meakin, and S. Reich, Macromolecules **16**, 757 (1983).

[10] J. Buceta and K. Lindenberg, Phys. Rev. E **69**, 011102 (2004).

[11] K. Wood, J. Buceta, and K. Lindenberg, Phys. Rev. E **73**, 022101 (2006).

[12] J. Buceta, K. Wood, and K. Lindenberg, Phys. Rev. E **73**, 042101 (2006).

[13] F. J. Cao, K. Wood, and K. Lindenberg. "Noise-induced phase transitions in field-dependent relaxational dynamics: The Gaussian ansatz", cond-mat/0702524 (submitted for publication), 2007.

7

Comprehensive Theory of Pattern Formation in Relaxational Systems

7.1 Introduction

As discussed in Chapter 6, the study of the interplay between fluctuations and nonlinearities in spatially extended systems provides insight into the counterintuitive and yet essential role of noise in many ordering transitions [1, 2, 3, 4, 5, 6, 7, 8]. In these systems the intensity of the fluctuations serves as a control parameter dictating the emergence of spatio-temporal structure. While the seminal model of noise-induced phase transitions relied on the collective amplification of short-time instabilities and required the presence of the so-called Stratonovich drift [2], we focus our attention on members of another class of relaxational models (introduced in Chapter 6) which exhibit such transitions in the absence of short-time instabilities [5, 6] and do not require a Stratonovich drift. They rely instead on the existence of a noise dependent effective nonequilibrium potential in the steady state whose qualitative behavior is impervious to a particular interpretation of the noise.

In this chapter we extend to pattern formation phenomena the earlier comprehensive study of relaxational models for Ising-like phase transitions between homo-

geneous states [6]. In addition to providing a broad characterization of these systems, we offer here the first example (to our knowledge) of hysteresis and multistability in a system exhibiting noise-induced spatial pattern-formation. In particular, we demonstrate via a modulated mean-field approach that the phase diagram of the system can be described by one of only four generalized portraits depending on generic geometric properties of the local potential and field-dependent relaxational functions. In Sec. 7.2 we introduce the model and implement our modulated mean field theory, including a semi-analytical characterization of the nature of the phase transitions between various phases. In Sec. 7.3 the theory is complemented with numerical simulations to verify its qualitative accuracy. We conclude with a summary in Sec. 7.4.

7.2 The Model and Modulated Mean Field Theory

We begin with the now familiar (see Chapter 6) generic evolution model of a relaxational space and time dependent field $\varphi_i(t)$ with field dependent coefficients given in terms of the set of Langevin equations

$$\dot{\varphi}_i(t) = -\Gamma\left(\varphi_i(t)\right) \frac{\delta \mathcal{F}\left(\{\varphi\}\right)}{\delta \varphi_i(t)} + \left[\Gamma\left(\varphi_i(t)\right)\right]^{1/2} \xi_i(t). \tag{7.1}$$

Here i labels a lattice site, $(\{\varphi\}) \equiv (\varphi_1, \ldots, \varphi_N)$ denotes the entire set of fields, and the relaxational function $\Gamma(\varphi)$ and its square root $[\Gamma(\varphi)]^{1/2}$ are both positive. The fluctuations ξ_i are Gaussian white noises with zero mean and correlation functions $\langle \xi_i(t)\xi_j(t')\rangle = \sigma^2\delta_{ij}\delta(t-t')$. The functional $\mathcal{F}$ consists of a local potential $V(\varphi)$ and an interaction term, so that $\delta\mathcal{F}/\delta\varphi_i(t) = -V'(\varphi_i) + \mathcal{L}\varphi_i$. In the previous chapter, we discussed the work of Buceta et al. [6], where the operator $\mathcal{L}$ was a d-dimensional nearest neighbor interaction, that is, a discrete version of the Laplacian diffusion operator. Here we will show that if $\mathcal{L}$ introduces a morphological instability and for appropriate choices of V, Γ, the system undergoes noise-induced phase transitions between disordered, patterned, and multistable phases.

A key ingredient for pattern formation is a competition between length scales. In a nearest neighbor model there is only one scale (the nearest neighbor distance), and so one needs to modify the interaction to introduce a second scale. We focus on a discrete version of the Swift-Hohenberg operator [9, 10], $\mathcal{L} = -D\left(k_0^2 + \nabla^2\right)^2$, but stress that this

specific form is not important, so long as the coupling leads to a morphological instability associated with pattern formation. We focus on the particular discretized form [5, 7]

$$\mathcal{L} = -D\left[k_0^2 + \left(\frac{2}{\Delta x}\right)^2 \sum_{i=1}^{d} \sinh^2\left(\frac{\Delta x}{2}\frac{\partial}{\partial x_i}\right)\right]^2, \tag{7.2}$$

where Δx is the lattice spacing and $\partial/\partial x_i$ indicates a partial derivative with respect to component i of the position vector $\boldsymbol{r} = (x_1, x_2, \ldots, x_i, \ldots, x_d)$. This form arises naturally when one recalls the action of the translation operator $\exp(\delta x \partial/\partial x) f(x) = f(x + \delta x)$ on any function $f(x)$. We can obtain the discrete dispersion relation by applying the operator (7.2) to a plane wave $e^{i\boldsymbol{k}\cdot\boldsymbol{r}}$,

$$\omega(\boldsymbol{k}) = -D\left[k_0^2 - \left(\frac{2}{\Delta x}\right)^2 \sum_{i=1}^{d} \sin^2\left(\frac{\Delta x}{2}k_i\right)\right]^2. \tag{7.3}$$

Here k_i denotes component i of the wave vector $\boldsymbol{k} = (k_1, k_2, \ldots, k_i, \ldots, k_d)$.

The most unstable modes are those that maximize $\omega(\boldsymbol{k})$. These modes characterize the underlying spatial regularity indicative of pattern formation. In the continuum these are the modes with $k = k_0$. In the discretized system the magnitudes k^* of the most unstable modes are shifted from k_0 and depend on direction. If $k_0\Delta x \leq 1$, then the range of variation of these magnitudes is smaller than 3%. It is therefore only a mild approximation to neglect the directional dependence of the solutions as long as one keeps count of the number of modes that satisfy this condition. The count, detailed in [5, 7], leads to the number $\mathfrak{n}(k^*) = [d\pi^{d/2}/\Gamma(d/2+1)](Nk^*/2\pi)^{d-1}$.

To capture a spatial structure we must make an ansatz about the modulated behavior of the field at locations $\boldsymbol{r}'$ which are coupled to the focus point $\boldsymbol{r}$ by the operator $\mathcal{L}$ [5]:

$$\varphi_{\boldsymbol{r}'} = \mathcal{A}(k^*) \sum_{\{\boldsymbol{k}^*\}} \cos\left[\boldsymbol{k}\cdot(\boldsymbol{r} - \boldsymbol{r}')\right], \tag{7.4}$$

where the sum is over wavevectors of magnitude k^* and all modes are assumed to contribute with equal weight $\mathcal{A}(k^*)$. The action of the coupling operator on the ansatz state is detailed in [5], whence one arrives at the result $\mathcal{L}\varphi_{\boldsymbol{r}} = D_1\left[\mathfrak{n}(k^*)\mathcal{A}(k^*) - \varphi_{\boldsymbol{r}}\right]$, with

$$D_1 = D\left[\left(\frac{2d}{(\Delta x)^2} - k_0^2\right)^2 + \frac{2d}{(\Delta x)^4}\right]. \tag{7.5}$$

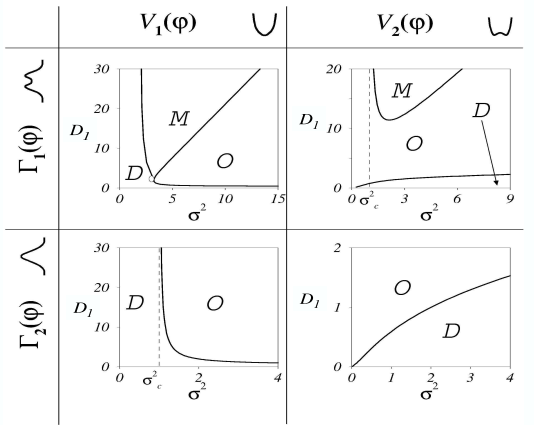

Figure 7.1: Mean-field phase diagrams as a function of the local potentials and field-dependent kinetic coefficients illustrated in Fig. 6.1. The labels D, O, and M within the diagrams respectively denote disordered, ordered (patterned), and multistable phases (in the latter, both the disordered and ordered phases are stable and can therefore in principle coexist). The small open circle in the phase diagram for Γ_1 and V_1 where the three phases merge indicates an isolated singular critical point (*triple* point) where a continuous phase transition between disordered and ordered phases occurs (see [6]).

This then leads to an equation for the field that depends only on a generic site index $\boldsymbol{r}$ that can simply be dropped:

$$\dot{\varphi} = \Gamma(\varphi)\left\{-\frac{\partial V(\varphi)}{\partial \varphi} + D_1\left[\mathfrak{n}^*\mathcal{A}^* - \varphi\right]\right\} + \left[\Gamma(\varphi)\right]^{1/2}\xi(t). \tag{7.6}$$

We have set $\mathfrak{n}(k^*) \equiv \mathfrak{n}^*$ and $\mathcal{A}(k^*) \equiv \mathcal{A}^*$. The noise $\xi(t)$ is zero-centered, Gaussian, and δ-correlated in time, $\langle \xi(t)\xi(t')\rangle = [\sigma^2/(\Delta x)^d]\delta(t-t')$. We set $\Delta x = 1$.

The mean amplitude $\mathcal{A}^*$ must be chosen self-consistently to complete the solution of the problem. The stationary probability density for our mean field stochastic process is

$$\begin{aligned}\rho_{\rm st}(\varphi; \mathfrak{n}^*\mathcal{A}^*) &= \mathcal{N}\left[\Gamma(\varphi)\right]^{(\alpha-1)} \\ &\times \exp\left\{-\frac{2}{\sigma^2}\left[V(\varphi) + \frac{D_1}{2}(\mathfrak{n}^*\mathcal{A}^* - \varphi)^2\right]\right\},\end{aligned} \tag{7.7}$$

where the normalization constant $\mathcal{N}$ depends on the amplitude. The constant α is 0 (1/2) for the Itô (Stratonovich) interpretation of the noise. Self-consistency is implemented

with the requirement that $\mathfrak{n}^*\mathcal{A}^*$ is the average value of the field at any point in space,

$$\mathfrak{n}^*\mathcal{A}^* = \int_{-\infty}^{\infty} \varphi\rho\left(\varphi; \mathfrak{n}^*\mathcal{A}^*\right) d\varphi, \tag{7.8}$$

which is appropriate if the distribution is even in φ and thus $\mathcal{A}^* = 0$, or if $\mathfrak{n}^*\mathcal{A}^*$ is much larger than the (appropriately phased) combined amplitudes of all the other modes. The latter occurs if there is an instability that leads to the formation of a pattern.

The structure of the mean amplitude problem as given in Eqs. (7.7) and (7.8) is formally identical to that obtained for the mean field problem with diffusive coupling, Eq. (6.10), discussed in Chapter 6, as is the analytic characterization of the self-consistent solutions. This realization serves as the primary analytical underpinning of our comprehensive study. In fact, while the mathematical structure is identical, the information provided by the solutions is of course different: in previous work the analysis led to the mean field that characterizes disordered and ordered global phases, whereas here it leads to the amplitude of the least stable modes. There is no need to repeat the entirety of that analysis, though we wish to reiterate the "bottom line" and further complement our study with numerical solutions to the mean field equation which reveal the analytical insight leading to these results. We limit ourselves to potentials $V(\varphi)$ and relaxation functions $\Gamma(\varphi)$ of even parity to ensure the existence of a disordered solution, and furthermore, without loss of generality, require that $V(0) = 0$ and $\Gamma(0) = 1$.

The entire phase space panorama is captured by considering the four generic combinations obtained by picking one of the two potentials and one of the two relaxation functions illustrated in Fig. 6.1. While the specific choices

$$V_1(\varphi) = \frac{\varphi^2}{2}, \qquad V_2(\varphi) = \frac{\varphi^4}{4} - \frac{\varphi^2}{2} \tag{7.9a}$$

$$\Gamma_1(\varphi) = \frac{1+\varphi^2}{1+\varphi^4}, \qquad \Gamma_2(\varphi) = \frac{1}{1+\varphi^2} \tag{7.9b}$$

have been made in the figure, only their general asymptotic behavior and their behavior around the origin is important, according to the detailed analysis in [6]. The four possible combinations then lead to phase diagrams of the form shown in Fig. 7.1. These are qualitatively identical to those considered in [6], though the numerical values differ. These particular ones have been calculated for the specific functions chosen for Fig. 6.1 with the Itô interpretation in Eq. (7.7). The Stratonovich interpretation would merely shift the boundaries between phases.

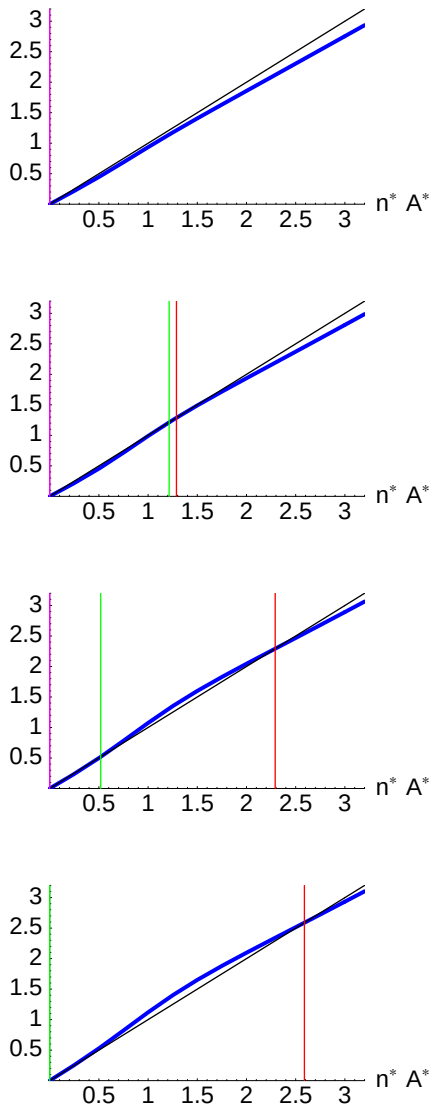

Figure 7.2: The mean field theory predicts a discontinuous transition for $V_1(\varphi)$, $\Gamma_1(\varphi)$ as σ^2 is increased at constant coupling. The figures show the intersections of $\mathfrak{n}^*\mathcal{A}^*$ (thin or black line) and the right-side of Eq. (7.8) (thick or blue curve). Vertical dark (red) lines show the points of intersection corresponding to stable solutions, while vertical light (green) lines correspond to unstable solutions. Notice that a stable solution exists at the origin for the top three figures. Noise is increased from $\sigma^2 \approx 0.75$ to $\sigma^2 \approx 6.0$, top to bottom. It is clear that a region of multistability exists in which both the stable disordered solution at the origin and the stable patterned solutions coexist.

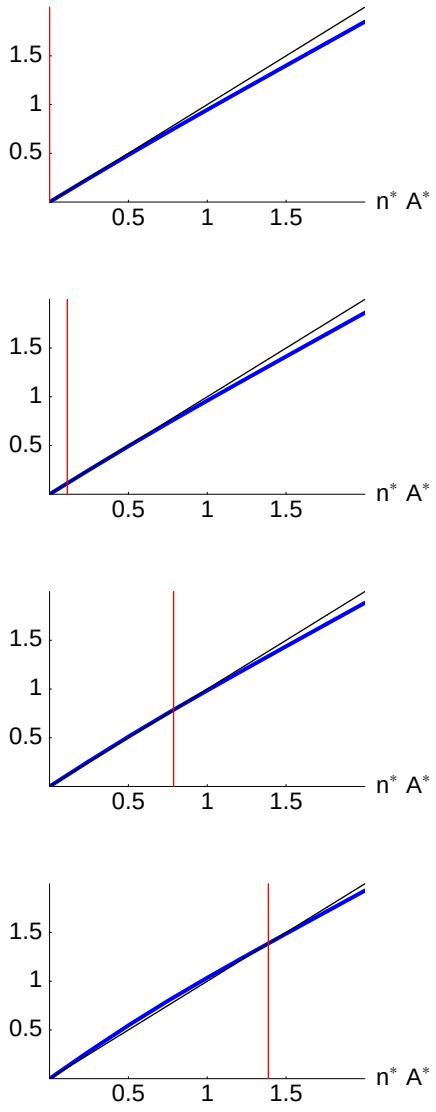

Figure 7.3: The mean field theory predicts a continuous transition for $V_1(\varphi)$, $\Gamma_2(\varphi)$ as σ^2 is increased at constant coupling. The figures show the intersections of $\mathfrak{n}^*\mathcal{A}^*$ (black) and the right-side of Eq. (7.8) (blue). Vertical red lines show the points of intersection corresponding to stable solutions. Noise is increased from $\sigma^2 \approx 0.85$ to $\sigma^2 \approx 3.0$, top to bottom. It is clear from the geometric relationships between the two curves that the transition is continuous.

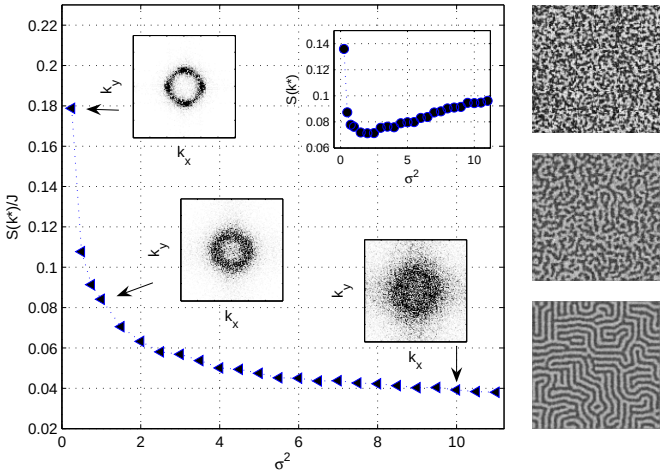

Figure 7.4: Relative power spectrum for the continuous disordering transition with $[V_2(\varphi), \Gamma_2(\varphi)]$ and $D = 0.5$. The snapshots on the right are steady-state configurations for $\sigma^2 = 10$, 1, and 0.25 from top to bottom. Insets show snapshots of the Fourier structure of the field. Upper right inset: power spectrum $S(k^*)$.

To reveal the nature of the phase transition taking place between different phases, we numerically calculate the expression given by the right hand side of Eq. (7.8), treating it as a function of the mean field parameter $\mathfrak{n}^*\mathcal{A}^*$. To ensure self-consistency, $\mathfrak{n}^*\mathcal{A}^*$ must be chosen so that Eq. (7.8) holds; geometrically speaking, the function given by the right hand side must intersect a line originating at the origin with slope 1. As shown in Figs. 7.2 and 7.3, increasing the noise intensity (top to bottom) qualitatively changes the nature of these intersections, leading to transitions which can be either discontinuous (to or from multistable phases) or continuous (between disordered and ordered phases). Fig 7.2 depicts a dicontinuous transition in which a stable solution emerges (other than the origin) for some finite, nonzero value of the noise. This manifests itself as a kink in the thick (blue) curve which intersects the thin (black) line. Notice that the origin is still a stable solution. As noise is further increased, this point of intersection splits into two points, one a stable (vertical dark (red) line) and one an unstable (vertical light (green) line) solution. Eventually, the noise becomes sufficiently large that the disordered solution–the solution at the origin–loses stability and only the large amplitude patterned phase exists. By contrast, a continuous transition appears in Fig 7.3, where

the intersection of the blue and black curves corresponding to a stable solution grows continously from zero, indicating an increasingly ordered phase as noise increases. These numerical portraits serve as the intuitive basis on which the the transitions between phases in Fig 7.1 should be viewed.

7.3 Numerical Simulations

To test the qualitative features of the mean field analysis via numerical simulations, we look for evidence of the three distinct transitions predicted by our theory: (1) $O \rightarrow D$ (continuous transition from order to disorder); (2) $D \rightarrow O$ (continuous transition from disorder to order); and (3) $D \rightarrow M$ (discontinuous transition from disorder to multistability). The distinction between transitions (1) and (2) is made so as to highlight the drastically different consequences of noise in the various phases. We do not separately consider the $M \rightarrow O$ transition since it is also marked by the destabilization of the zero amplitude solution and therefore closely resembles transition (2). To cover the three transitions we consider the three representative cases $[V_2(\varphi), \Gamma_2(\varphi)]$, $[V_1(\varphi), \Gamma_2(\varphi)]$, and $[V_1(\varphi), \Gamma_1(\varphi)]$, which should exhibit (1), (2), and (3), respectively, as noise intensity is increased for an appropriate coupling coefficient D_1 (see Fig. 7.1). The case $[V_1(\varphi), \Gamma_2(\varphi)]$ was considered in a previous work, but with the Stratonovich interpretation for the noise [5].

We perform our simulations on a lattice of size $L = N\Delta x = 128$ with $\Delta x = 1$, $k_0 = 1$, and $\Delta t = 0.005$. The magnitude of the least stable wavevectors is then $k^* \sim 1.035$. With one exception (noted later), we use Neumann-Dirichlet boundary conditions, that is, the field and its normal derivative are zero at the boundaries. We use an adapted Heun-like algorithm appropriate for an Itô interpretation of the noise [11], and in calculating order parameters we typically consider time averages obtained once the system has reached a steady state. Our results are essentially identical for different realizations of the noise, so that it is sufficient to present the time-averaged results for any single realization.

There are different ways to characterize pattern formation. For this purpose we introduce the Fourier transform $\widetilde{\varphi}_{\mathbf{k}}$ of the field $\varphi_{\mathbf{r}}$, $\widetilde{\varphi}_{\mathbf{k}} = (1/N^d) \sum_{\mathbf{r}} \varphi_{\mathbf{r}} \exp(-i\mathbf{k} \cdot \mathbf{r})$. One quantity commonly invoked for the characterization of patterns is the *power spec-*

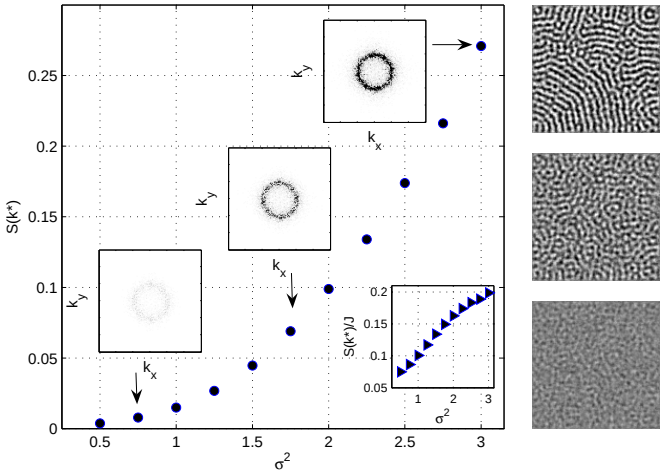

Figure 7.5: Power spectrum for the continuous disorder-order transition with $[V_1(\varphi), \Gamma_2(\varphi)]$ and $D = 3$. The snapshots on the right are the steady-state configurations for $\sigma^2 = 3$, 1.75, and 0.75 from top to bottom. Insets: Fourier transforms of the field.

trum at wavevectors of magnitude k, $S(k) = \sum_{\{\boldsymbol{k}^*\}} \widetilde{\phi}_{\mathbf{k}} \widetilde{\phi}_{-\mathbf{k}}$, where the sum runs over all modes of magnitude k (in our discretized system, the sum includes all wavevectors whose magnitude lies in a ring of width $2\pi/L$ centered on k). Another is the *flux of convective heat*, $J = (1/N^d) \sum_{\mathbf{r}} \phi_{\mathbf{r}}^2$. The functional relation between these two quantities is simply $J = \sum_k S(k)$, where the sum runs over the magnitudes of the modes. One order parameter is $S(k^*)$ (or, more accurately, the average of $S(k^*)$ over realizations of the noise but, as noted earlier, we find that different realizations of the noise lead to essentially identical results), which reflects the total contribution of the most unstable modes to the flux of convective heat. Our mean field theory provides the result $S(k^*) = \mathfrak{n}(k^*)\mathcal{A}^2(k^*)$ [8]. Another order parameter is the relative power spectrum $S(k^*)/J$, which measures the relative contribution of the least stable modes to the total flux. It provides information on the coherence of the pattern that the simple order parameter $S(k^*)$ can not provide. The mean field theory gives $J = S(k^*)$ since it only deals with the most unstable modes. A meaningful prediction of J would require the ability to determine the power spectrum for all wavevector magnitudes. We exhibit both order parameters as obtained from our numerical simulations.

Consider first the case (V_2, Γ_2). This is the least interesting case since it exhibits patterns only at small noise intensities with a transition to a disordered state as the noise intensity is increased. Nevertheless, this is a good example to illustrate the information in the two different order parameters and, for that matter, one where the limitations of the mean field theory become apparent. In the top right inset in Fig. 7.4 we see the initial decrease of $S(k^*)$ to zero and the associated disappearance of spatial structure, as predicted. While the mean field theory does not quantitatively predict the transition parameter values, it does lead to the correct qualitative behavior. The order parameter does not remain at zero after the transition, as the mean field theory would predict, instead increasing again for larger values of the noise. However, note that as seen in the insets showing the Fourier structure of the spatial configurations, in spite of this increase in the order parameter, the system does not again become ordered with increasing noise because modes other than those of magnitude k^* become unstable as well. The coherence of the pattern is seen to decrease as the ring of most unstable modes becomes thicker, effectively eliminating the spatial structure visible at low values of the noise. This incoherent configuration consisting of many modes is not captured by the mean field theory, which is valid only near the bifurcation point. The increasing incoherence with increasing noise is evident in the other order parameter, $S(k^*)/J$, which continues to decrease with increasing noise.

Next, consider the case (V_1, Γ_2), predicted to exhibit a continuous, pattern-forming transition with increasing noise. In fact, as evidenced in Fig. 7.5, increasing the noise for a given value of the coupling constant leads to increasingly visible spatial structure and an ever-intensifying ring of unstable wavevectors. As predicted, the transition is continuous and points to the ordering role of noise in the development of spatial structure.

Finally, we consider the more complex and interesting disorder-multistability transition predicted with the combination (V_1, Γ_1). Our theory predicts the occurrence of multistability and hysteresis characteristic of a first-order phase transition. To test for the requisite memory of initial conditions, we perform simulations in two directions. In one case, we start from a homogeneous zero field state and systematically increase σ^2. In the other, we start from the patterned steady state occurring for high noise intensity and decrease σ^2. In each instance, we use the steady state obtained for the

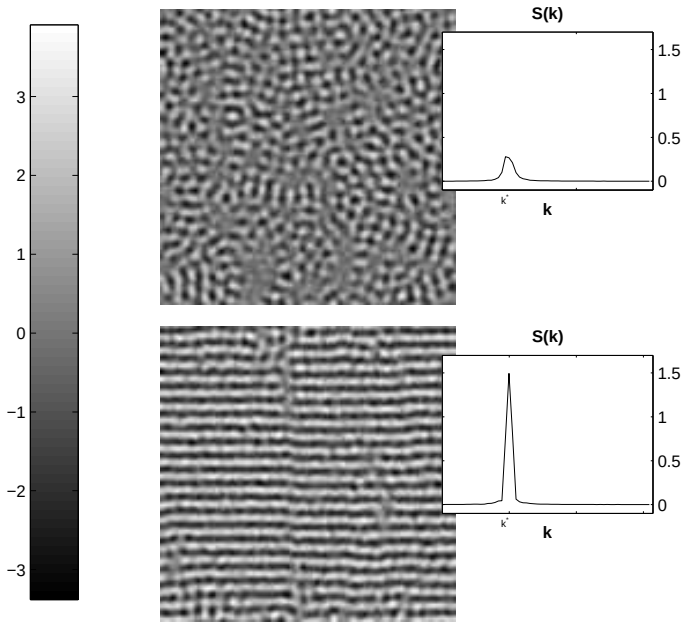

Figure 7.6: Snapshots of the field for $[V_1(\varphi), \Gamma_1(\varphi)]$ that illustrate hysteresis in the discontinuous disorder-order phase transition with $D = 5$ and $\sigma^2 = 3.10$. The initial condition is uniform in the top panel and a strongly patterned state in the bottom panel. Boundary conditions are periodic. See text for more detailed description of simulation sequence. The insets show the power spectrum $S(k)$ as a function of k.

previous value of σ^2 (either above or below the current one) as the initial state for the subsequent simulation. In order to insure the timely appearance of a clear pattern, in these simulations we have implemented periodic boundary conditions. Figure 7.6 demonstrates two clearly different states for the same values of the parameters depending on the initial condition. Hysteresis is also apparent in the marked dependence of $S(k^*)$ on the initial condition. We have ascertained this same behavior for various realizations of the noise, and have also ascertained that hysteresis is only observed in a limited range of parameter values. In particular, for fixed D the uniform solution becomes unstable with increasing noise and the system passes into the purely ordered phase.

7.4 Discussion

We have developed a comprehensive theory of noise-induced phase transitions to patterned states in single-field relaxational systems with field-dependent coefficients. Previous work on this subject focused on a particular system [5], which is here generalized to a broad classification of the geometric properties of the potential function and the relaxational function that lead to one of four possible phase diagrams. Pattern formation requires a length scale competition that we capture via a discrete version of the Swift-Hohenberg coupling. Our comprehensive theory parallels that developed for single field relaxational systems with nearest neighbor coupling [6]. The theoretical analysis is carried out via a mean field theory modified from the simplest form by the inclusion of spatial modulation. A linear stability analysis then yields the dispersion relation from which one extracts the most unstable modes. Semi-analytical arguments provide insight into the nature of transitions between various phases, and numerically generated phase portraits confirm the qualitative validity of the theory. Finally, lattice simulations agree with the mean field predictions, providing us evidence that a generalized characterization of pattern formation in this class of relaxational systems is fully in hand. Of particular interest are the transitions to ordered or multistable pattern states induced purely by noise, as they reveal the potentially counterintuitive role played by stochasticity in nonequilibrium systems characterized by relaxation to the minimum of an effective free-energy like functional. In closing this chapter, we also note that we have thus far implicated noise as the sole source of order induced phenomena, both spa-

tially uniform and spatially structured, in our generic class of relaxational models. The next chapter begins our exploration of a different type of ordering phenomenon in these systems, namely, the noise-induced oscillatory (and thus time-dependent) cooperativity.

Acknowledgements

Chapter 7 contains material which appears, in part, in K. Wood, J. Buceta, and K. Lindenberg, Phys. Rev. E **73**, 022101 (2006).

References

[1] J. García-Ojalvo and J. M. Sancho, *Noise in Spatially Extended Systems* (Springer, New York, 1999).

[2] C. Van den Broeck, J. M. R. Parrondo, and R. Toral, Phys. Rev. Lett. **73**, 3395 (1994); C. Van den Broeck, J. M. R. Parrondo, R. Toral, and R. Kawai, Phys. Rev. E **55**, 4084 (1997).

[3] M. Ibañes, J. García-Ojalvo, R. Toral, and J. M. Sancho, Phys. Rev. Lett. **87**, 020601 (2001).

[4] R. Kawai, X. Sailer, L. Schimansky-Geier, and C. Van den Broeck, Phys. Rev. E **69**, 051104 (2004).

[5] J. Buceta, M. Ibañes, J. M. Sancho, and K. Lindenberg, Phys. Rev. E **67**, 021113 (2003).

[6] J. Buceta and K. Lindenberg, Phys. Rev. E **69**, 011102 (2004).

[7] J. Buceta, J. M. R. Parrondo, and F. J. de la Rubia, Phys. Rev. E **63**, 031103 (2001).

[8] J. Buceta and K. Lindenberg, Phys. Rev. E **68**, 011103 (2003).

[9] M. C. Cross and P.C. Hohenberg, Rev. Mod. Phys. **65**, 851 (1993).

[10] J. Swift and P. C. Hohenberg, Phys. Rev. A **15**, 319 (1977).

[11] O. Carrillo, M. Ibañes, J. García-Ojalvo,J.Casademunt, and J. M. Sancho, Phys. Rev. E **67**, 046110 (2003).

8

Noise-induced oscillatory behavior in field-dependent relaxational dynamics

8.1 Introduction

Simple models of relaxational dynamics–particularly those with field-dependent kinetic coefficients–have been a subject of considerable recent interest [1, 2, 3, 4, 5, 6], and we have discussed in Chapters 6 and 7 two general types of ordering phenomena in these systems. Again, we remind the reader that such generic models have elicited significant scientific interest for a number of reasons. First, these particular relaxational flows may explain situations where inverted phase diagrams are obtained [5]. As in some polymer mixtures where phase separation increases with temperature, in these flows one can find phase diagrams where stronger noise leads to greater order. Second, and perhaps more appropriate to our studies, these models provide a mechanism for noise-induced phase transitions that neither require a Stratonovich drift [7, 8] nor depend entirely on short-time dynamic instabilities. In fact, the presence of noise-induced phase transitions in these systems does not depend on the noise interpretation and resembles, in some sense, an equilibrium phase transition where the primary features of an effective potential are altered through varying a control parameter, leading to qualitatively distinct macroscopic

phases. Third, in certain noise intensity regimes these systems may exhibit noise-induced multistability phenomena and the associated hysteresis, such that the system can settle into an ordered or a disordered state depending on the initial condition [9, 10]. The comprehensive studies discussed in Chapters 6 and 7 have revealed that the occurrence of these features simply depends on the balance of convexities between the relaxational coefficients and the local potential of the model, and not on the particular form of these functionals [9, 10]. In addition, we have provided the steady state mean field formulations for these systems and numerically obtained phase diagrams which entirely support the analytical arguments and match the results of lattice simulations.

Typically, these transitions between disordered and ordered or patterned states have been studied in systems described by a *single* field. More recently, however, the study of the constructive role of fluctuations in spatially extended systems has been applied to the case of two coupled fields [11]. It has been shown that in such systems, noise may induce macroscopic limit cycles via pure noise-induced phase transitions. Again, however, these studies specifically focused on dynamically induced phase transitions and therefore depend on the Stratonovich drift, i.e., on the interpretation of the noise.

In parallel with that idea, herein we consider such behavior in systems where the interpretation of the noise is irrelevant to the occurrence of the phenomenon. Thus, we consider the role of an additional field in a relaxational dynamics with field dependent coefficients. The additional field can be thought of as introducing inertial effects into the relaxational dynamics, cf. below, and leads to noise-induced collective oscillatory behavior. Moreover, our numerical simulations show that addition of an inertial contribution to a relaxational model that displays noise-induced stationary pattern formation also leads to oscillatory spatio-temporal structures.

In Sec. 8.2 we extend the models from previous chapters to include an additional degree of freedom or, equivalently, an inertial contribution at each lattice site, and describe the resulting expected oscillatory behaviors of the system. Numerical results that confirm this behavior are presented in Sec. 8.3. Finally, in Sec. 8.4 we summarize our main conclusions. We note that because the noise-induced phenomenon considered here involves an inherent time-dependence, we cannot resort to our static mean field theories for analytical treatment. However, we return to this problem in Chapter 9.

8.2 Two degrees of freedom per lattice site

A question posed in recent studies concerned the possibility of inducing collective oscillatory behavior in spatially extended systems that exhibit a purely noise-induced phase transition [11]. The question was answered in the affirmative for a system in which the transition is induced dynamically through a short-time instability that depends on the so-called Stratonovich drift. Specifically, the introduction of inertia in that system leads to a macroscopic limit cycle. Herein, we pursue a similar objective in systems with field-dependent relaxational dynamics where the noise interpretation is not a relevant component in the mechanism. As such, we depart from the generic relaxational models from the previous chapters, and we consider below both the case of diffusive coupling and the case leading to pattern-forming instabilities.

Before we begin, it should be noted that in this chapter, we make the particular choice

$$\Gamma(\varphi) = \frac{1+\varphi^2}{1+\varphi^4} \tag{8.1}$$

as a generic example of a relaxational coefficient with a minimum at the origin. Note that this form of the coefficient leads to a maximum relaxation rate when $|\varphi_i|$ is around 1, and that $\partial^2\Gamma(\varphi)/\partial\varphi^2\big|_{\varphi=0} > 0$. Note also the ordering role of the fluctuations as well as the noise-induced multistability when K is sufficiently large. Chapters 6 and 7 remind us that a number of different phase diagrams (and corresponding phase transitions) are possible depending on the choice of $\Gamma(\varphi)$; we here forego the full generality and settle on Eq. (8.1), which provides sufficient complexity to induce interesting behavior, namely noise-induced multistability and ordering phenomena.

Our starting point for the diffusive problem is our relaxational model with an additional degree of freedom z_i,

$$\begin{aligned} \dot{\varphi}_i &= -\Gamma(\varphi_i)\frac{\delta\mathcal{F}(\{\varphi\})}{\delta\varphi_i} + [\Gamma(\varphi_i)]^{1/2}\,\xi_i(t) - \omega z_i, \\ \dot{z}_i &= \omega\varphi_i, \end{aligned} \tag{8.2}$$

where ω is a frequency and the interactions in $\mathcal{F}$ are chosen to produce nearest-neighbor coupling. Equations (8.2) can be expressed as a single equation including an inertial term, $\ddot{z}_i$, as

$$\ddot{z}_i + \omega^2 z_i = \omega G(\{\varphi\}), \tag{8.3}$$

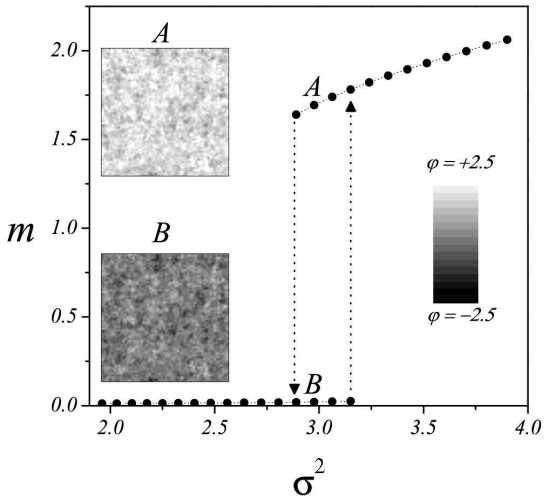

Figure 8.1: Order parameter $m = |\langle\varphi\rangle|$ obtained from numerical simulations of the single field model for $K = 10$ as a function of the intensity of the fluctuations. The insets show a density plot of the field for two different sets of initial conditions and $\sigma^2 \approx 3$, where the system presents multistabilty. From [9].

where

$$G(\{\varphi\}) = -\Gamma(\varphi_i)\frac{\delta\mathcal{F}(\{\varphi\})}{\delta\varphi_i} + [\Gamma(\varphi_i)]^{1/2}\xi_i(t). \tag{8.4}$$

In Eq. (8.3) it is understood that every φ_i on the right hand side is to be replaced by $\dot{z}_i/\omega$. Equation (8.3) is thus a closed second-order stochastic differential equation for the variable set $\{z_i\}$.

The mean field approximation description of the system reads

$$\begin{aligned}\dot{\varphi} &= G(\varphi;\langle\varphi\rangle) - \omega z,\\ \dot{z} &= \omega\varphi,\end{aligned} \tag{8.5}$$

where

$$G(\varphi;\langle\varphi\rangle) = -\Gamma(\varphi)\frac{\delta\mathcal{F}(\varphi;\langle\varphi\rangle)}{\delta\varphi} + [\Gamma(\varphi)]^{1/2}\xi(t). \tag{8.6}$$

Note that $\langle G(\varphi;\langle\varphi\rangle)\rangle = 0$ is the stationary state condition for the relaxational dynamics given by the globally coupled mean field equation. Moreover, if $\omega = 0$ then the system will reach a steady state since Eq. (8.2) becomes equivalent to the single field model, and

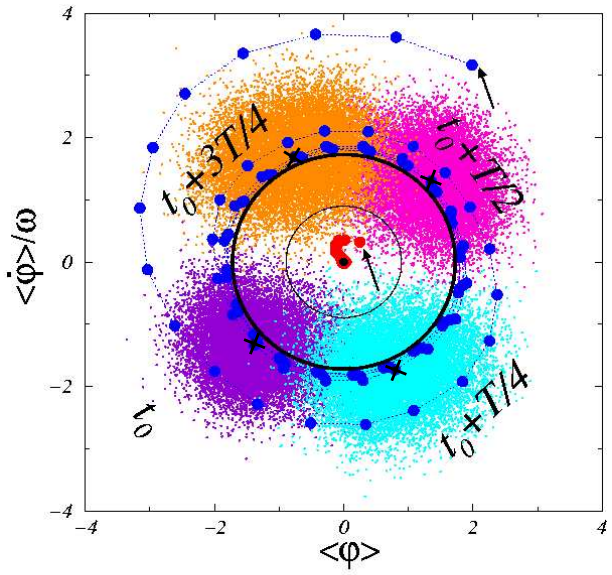

Figure 8.2: Shown in gray scale are simulation results: $\langle\varphi(t)\rangle$ vs $\langle\dot{\varphi}(t)\rangle/\omega$. Depending on the initial conditions, the system ends in a homogeneous state or in a limit cycle (see text). The central black circle indicates the stable fixed point. The wide solid black line is the stable limit cycle, and the thin black line the unstable limit cycle, obtained from Eq. (8.7). The numerical simulations for two sets of initial conditions indicated by arrows are plotted. The clouds of points indicate the values of $\varphi_i(t)$ and $\dot{\varphi}_i(t)/\omega$ at four times that cover a period of oscillation once the oscillatory stationary regime is reached. The average values $\langle\varphi(t)\rangle$ and $\langle\dot{\varphi}(t)\rangle/\omega$ of these clouds are given by the circles with a superimposed cross.

inertia plays no role. Without the contribution G, the set (8.5) behaves as the simplest possible oscillator, namely, the harmonic oscillator with frequency ω.

This mean field problem, while simple on the surface, proves remarkably challenging to solve in analytical detail. In particular, the interesting oscillations induced in this system are fundamentally time-dependent, precluding the typical steady-state self-consistent solution possible in the case of phase transitions to static states. While Chapter 9 provides a method for analytically studying the time-dependent dynamics of these phase transitions in certain limits, we first only describe the behavior that we observe on the basis of our numerical simulations (next section). We find that provided

the noise intensity is not too much greater than the critical value for the single-degree-of-freedom problem, the mean values of the fields are well described by the simple forms

$$\langle\varphi(t)\rangle = \langle\varphi(t)\rangle_{\omega=0}\cos(\omega t), \quad \langle z\rangle = \langle\varphi(t)\rangle_{\omega=0}\sin(\omega t) \tag{8.7}$$

where $\langle\varphi(t)\rangle_{\omega=0}$ is the mean value of the single-degree-of-freedom problem (see Chapter 6 and [9]). For simplicity, the phase has been set arbitrarily to zero. We thus find that the oscillations occur according to the harmonic oscillator nature of the problem in the absence of G in Eq. (8.5), with an amplitude determined by the relaxational dynamics in the absence of the oscillatory behavior. This then means that the trajectory in the space $(\langle\varphi(t)\rangle, \langle\dot{\varphi}(t)\rangle/\omega)$ is a circle of radius $\langle\varphi(t)\rangle_{\omega=0}$:

$$\left(\langle\varphi(t)\rangle^2 + \frac{\langle\dot{\varphi}(t)\rangle^2}{\omega^2}\right)^{1/2} = \langle\varphi(t)\rangle_{\omega=0}. \tag{8.8}$$

We also find that as the noise intensity increases, the trajectories remain periodic but that the circular shape becomes distorted so that there is an additional modulation of the amplitude.

Consider now the inclusion of a second degree of freedom in the case of Swift-Hohenberg coupling, when the single-degree-of-freedom system undergoes transitions to patterned states with increasing noise intensity. Our extended system in one dimension (to which we restrict our numerical simulations) reads

$$\begin{aligned}
\dot{\varphi}_i &= -\Gamma(\varphi)\left(\left[1 + K\left(1 + 4\sinh^2\left(\frac{1}{2}\frac{\partial}{\partial x}\right)\right)\right]\varphi_i\right) \\
&\quad + [\Gamma(\varphi)]^{1/2}\,\xi_i(t) - \omega z_i, \\
\dot{z}_i &= \omega\varphi_i.
\end{aligned} \tag{8.9}$$

We have again chosen a harmonic local potential. The particular form of the coupling operator arises from the discretization of the Swift-Hohenberg operator [8, 10] and the choice $k_0 = 1$. In this case we find from our numerical simulations with the relaxational function (8.1) that for noise intensities near the critical value the fields are now modulated in space and in time and are simply given by

$$\begin{aligned}
\langle\varphi(x,t)\rangle &= 2\mathcal{A}(k^*)\cos(k^*x)\cos(\omega t), \\
\langle\varphi(x,t)\rangle &= 2\mathcal{A}(k^*)\cos(k^*x)\sin(\omega t).
\end{aligned} \tag{8.10}$$

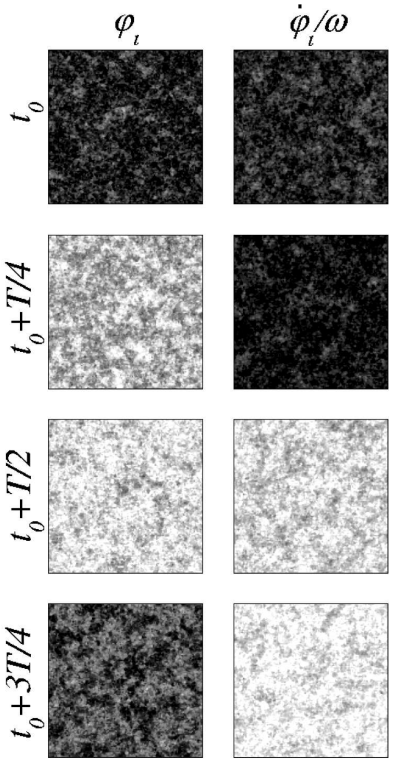

Figure 8.3: Spatial density plots of φ_i and $\dot{\varphi}_i/\omega$ at various times through a cycle for the clouds shown in Fig. 8.2. The grey scale is the same for all plots: black (-2) to white ($+2$). Note the oscillatory behavior and the phase difference between the two fields.

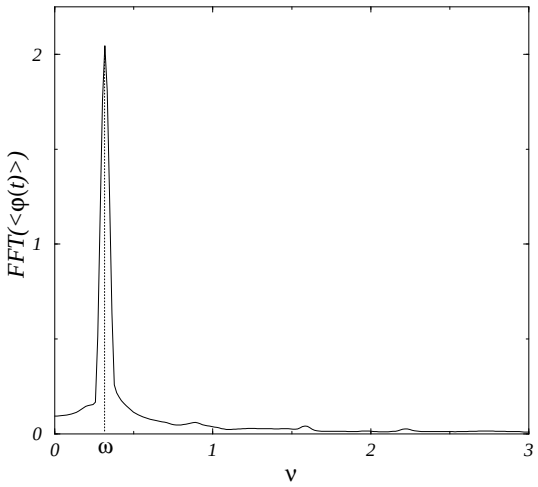

Figure 8.4: Fourier transform of $\langle\varphi(t)\rangle$ for the numerical simulation results shown in Fig. 8.2 in the case of oscillatory asymptotic behavior.

Again for simplicity we have set the spatial and temporal phases to zero.

Numerical simulations to illustrate these behaviors in detail are presented in the next section.

8.3 Numerical simulations

As an example of the qualitative behavior of the one-degree of freedom system with diffusive coupling, we show first in Fig. 8.1 numerical simulations implementing periodic boundary conditions in two-dimensional 128×128 lattices, choosing the parameter values in Fig. 8.1, which correspond to a point of multistability for the single field model. Here, as noise is increased, the disordered solution gives way to a multistable regime and finally a completely stable, ordered solution.

When including a second degree of freedom, we focus on the case $\sigma^2 = 3$ and $\omega^2 = 0.1$. Figure 8.2 shows $\langle\varphi(t)\rangle$ vs $\langle\dot{\varphi}(t)\rangle/\omega$ for two different sets of initial conditions. The initial conditions are indicated by arrows. For one set of initial conditions the system is driven toward the homogeneous state $\langle\varphi(t)\rangle = \langle\dot{\varphi}(t)\rangle = 0$, while the other leads to an oscillatory regime. Note how well the form (8.8) captures the behavior of the average behavior of these trajectories. In the same figure we show the entire distribution of

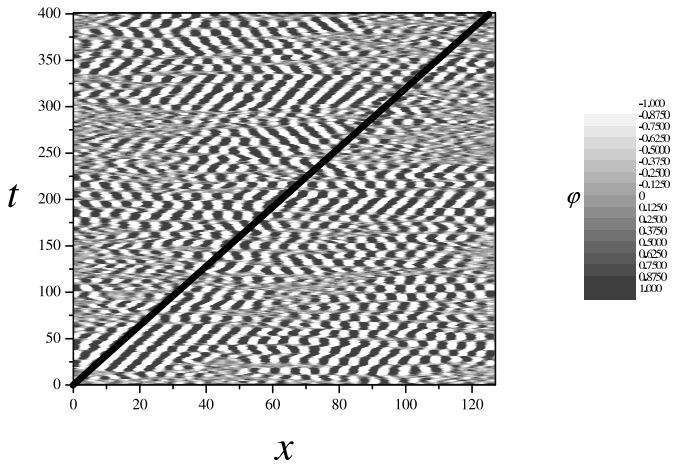

Figure 8.5: Density plot for $\varphi(x,t)$ obtained from a numerical simulation of Eq. (8.9) for a chain of 128 oscillators with periodic boundary conditions, $K = 10$, and $\sigma^2 = 3$. The diagonal solid line has a slope ω, and has been drawn to guide the eye. The spatial patterns are of length $2\pi k^*$ with $k^* \simeq 1.05$.

$(\varphi_i(t), \dot{\varphi}_i(t)/\omega)$ at four different times during a period of oscillation once a stationary oscillatory regime is reached. The average values are indicated by black circles with superimposed crosses. The noisy dynamics spreads the points around the average values. It is interesting to note that although some points fall within the attractor of the stable fixed point, they are nevertheless driven to the oscillatory orbit because they are driven by the average value and not by their individual dynamics.

In Fig. 8.3 we show spatial density plots for the values of $\varphi_i(t)$ and $\dot{\varphi}_i(t)/\omega$ at the centers of the clouds of points shown in Fig. 8.2. The oscillations of the field are represented by variations in time of the grey scale. Note the phase difference between the two fields.

In Fig. 8.4 we show the time Fourier transform of the field average $\langle\varphi(t)\rangle$ for the data shown in Fig. 8.2 for the case of the initial conditions leading to oscillatory behavior. As indicated in Eq. (8.7), the system presents the single frequency ω in its dynamics.

For the case of Swift-Hohenberg coupling we have carried out numerical simulations of Eq. (8.9) in a chain of $N = 128$ oscillators with periodic boundary conditions, with coupling coefficient $K = 10$, noise intensity $\sigma^2 = 3$, and $k_0 = 1$. Since $k^* \simeq 1.05$,

the so-called aspect ratio is $\Lambda = N/(2\pi/k^*) \sim 20$. That is, at any given time, we expect approximately 20 wavelengths of the pattern. Figure 8.5 shows $\varphi(x,t)$ by means of a density plot. The diagonal solid line has been drawn to guide the eye and has a slope ω. Note that in agreement with our earlier description, an oscillatory pattern develops with temporal and spatial modulations ω and k^* respectively.

Finally, we comment on the possibility of observing multistability. The phase diagram indicates that for the values of the parameters used in our simulation the system lies within a multistable region. We have explicitly shown this multistability in the single-degree-of-freedom problem [10] and would expect that an oscillatory pattern develops or not depending on the initial condition. While certain regions in Fig. 8.5 appear less ordered than others and this might provide an indication of multistability, we did not pursue this possibility in detail, our purpose here being mainly to present the nature of the noise-induced spatio-temporal pattern.

8.4 Discussion

In this chapter we have shown the effects of inertia in relaxational systems with field-dependent kinetic coefficients. As shown in previous studies of spatially extended systems with dynamically noise-induced phase transitions, inertia may induce oscillatory behavior in spatially extended systems driven by noise [11]. We have here introduced inertia in relaxational global order-disorder systems and in relaxational pattern-forming systems. These systems are particularly interesting (and different from those in which transitions are induced dynamically) because the transitions do not depend on the Stratonovich drift and thus occur regardless of the interpretation of the noise. They are also particularly interesting because there are multistability regimes where the initial conditions determine whether the system is locked in a homogeneous state or in an ordered or patterned state. In fact, we have shown that adding an additional degree of freedom does not interrupt the capacity for these unique phase transitions, but instead results in macroscopic oscillations whose radius closely mimics the order parameter used in the single field case. Thus, the interesting features of the transition remain–including noise-induced ordering, pattern formation, and multistability–but these macroscopic phases are no longer characterized by time-independent steady states,

but instead by cooperative, large-scale oscillations. We have supported our conclusions via numerical simulations. The challenge that remains is an analytic solution of the problem, even in the mean field case, and we pursue this objective in Chapter 9 in a more general setting.

Acknowledgments

Chapter 8 contains material which appears, in part, in J. Buceta, K. Wood, and K. Lindenberg, Phys. Rev. E **73**, 042101 (2006).

References

[1] P.C. Hohenberg, and B.I. Halperin, Rev. Mod. Phys. **49**, 435 (1977).

[2] J. García-Ojalvo and J.M. Sancho, *Noise in Spatially Extended Systems* (Springer, New York, 1999).

[3] R. Montagne, E. Hernández-García, and M. San Miguel, Physica D **96**, 47 (1996).

[4] M. Ibañes, J. García-Ojalvo, R. Toral, and J.M. Sancho, Phys. Rev. Lett. **87**, 020601 (2001).

[5] H.L. Snyder, P. Meakin, and S. Reich, Macromolecules **16**, 757 (1983).

[6] C. Van den Broeck, J.M.R. Parrondo, and R. Toral, Phys. Rev. Lett. **73**, 3395 (1994); C. Van den Broeck, J.M.R. Parrondo, R. Toral, and R. Kawai, Phys. Rev. E **55**, 4084 (1997).

[7] O. Carrillo, M. Ibañes, J. García-Ojalvo, J. Casademunt, and J.M Sancho, Phys. Rev. E **67**, 046110 (2003).

[8] J. Buceta, M. Ibañes, J.M. Sancho, and K. Lindenberg, Phys. Rev. E **67**, 021113 (2003).

[9] J. Buceta and K. Lindenberg, Phys. Rev. E **69**, 011102 (2004).

[10] K. Wood, J. Buceta, and K. Lindenberg, Phys. Rev. E **73**, 022101 (2006).

[11] R. Kawai. X. Sailer, L. Schimansky-Geier, and C. Van den Broeck, Phys. Rev. E **69**, 051104 (2004).

9

Dynamics of phase transitions in field-dependent relaxational models

9.1 Introduction

As we have seen in the previous chapters, the interplay of stochasticity and nonlinearity often leads to a wide range of interesting and often counterintuitive behaviors, particularly in the form of nonequilibrium phase transitions in spatially extended systems. We have focused specifically on "purely-noise-induced" transitions, which include the emergence of periodic spatial structures and pattern formation in increasingly noisy systems [2] (see Chapter 7), and purely noise-induced collective oscillatory behavior in multi-field systems [4] (see Chapter 8). The transitions arise from a class of generic nonequilibrium models whose dynamics arise entirely from an energy functional-like relaxational dynamics, and not from short-time dynamic instabilities which become strengthened and sustained by spatial coupling. As such, these models represent systems that, while decidedly nonequilibrium and potentially time-dependent in nature, nevertheless maintain certain parallels with equilibrium statistical models, namely the evolution towards the minimum of a (possibly time-dependent) effective potential. Our focus in this chapter is on an analytical characterization of the dynamics underlying phase

transitions in systems with field dependent relaxational dynamics, thus completing our characterizations from Chapters 7 and 8.

Analytic work on these models has been fairly limited, with most of the information coming from numerical simulations. We are not aware of solvable analytic theories for locally coupled (e.g. nearest neighbor) noisy extended systems in which any sort of ordering transition is observed as the system or noise parameters are varied. Globally coupled arrays have been more amenable to mean field theories based on the analytic solution of a Fokker-Planck equation in the stationary state. This approach has been successfully applied to systems that achieve a time-independent steady state. Such mean field theories provide information about the nature of the steady state and the conditions that lead to disordered vs ordered states. Thus, while quite useful for ascertaining asymptotic properties, these static theories provide no insight into the dynamical evolution toward a steady state. Such insight is particularly important in multistable systems.

Most strikingly, these theories fail to provide even a reasonable asymptotic description of phase transitions to collective time-dependent behavior, when the complexity of the corresponding Fokker-Planck equation prohibits a self-consistent analytical treatment [4] even in globally coupled arrays. The complicated behavior seen, for example, in the transition to noise-induced limit cycles thus requires different methods for analytic study [3].

Our purpose here is to provide an approximate analytical method supplementary to the mean field approach for studying the dynamics of noise-induced phase transitions in relaxational systems inspired by a related quantum field method [5]. By introducing a Gaussian ansatz and a series expansion about the (time-dependent) mean field values, we develop a time-dependent theory which captures the dynamics of these systems in the limit of strong spatial coupling. In addition to providing new analytical insight into the evolution to the steady state in one-field systems, this treatment yields a set of simple approximate ordinary differential equations detailing the oscillatory dynamics and the approach to these dynamics in two-field systems. We note that an alternative approach to the one adopted in this chapter is to generalize the procedure developed in [3]–while also including a large coupling ansatz–that gives a set of differential equations for the central moments.

The chapter is organized as follows. In Sec. 9.2 we briefly recall the one- and two-field relaxational models. The mean field equations and the Gaussian ansatz for their solution are presented in Sec. 9.3. In Sec. 9.4 we analyze the one-field system and test our Gaussian ansatz results in the steady state and in the dynamical approach to the steady state, including regimes of multistability. The two-field system is examined in Sec. 9.5, where we show that our theory captures the collective oscillatory behavior, including regimes of multistability. In both Secs. 9.4 and 9.5 we explore approximate solutions to the differential equations obtained with the Gaussian ansatz to successfully reduce the problems to quadrature in some regimes. We conclude with a short summary in Sec. 9.6.

9.2 The models

Again, we embark from the one-field and two-field relaxational models discussed at length in the previous chapters. In the one-field case we introduced the Langevin equation defined on a lattice [1],

$$\dot{\varphi}_i = -\Gamma(\varphi_i)\frac{\delta\mathcal{F}(\{\varphi\})}{\delta\varphi_i} + [\Gamma(\varphi_i)]^{1/2}\xi_i(t), \tag{9.1}$$

where φ_i is the value of the scalar field at site i, $\Gamma(\varphi_i)$ is the field-dependent kinetic coefficient, $\mathcal{F}(\{\varphi\})$ is an energy functional, and $\xi_i(t)$ is a spatio-temporal white noise with zero mean and intensity σ^2, $\langle\xi_i(t)\xi_j(t')\rangle = \sigma^2\delta_{ij}\delta(t-t')$. As the choice of noise interpretation does not qualitatively affect the dynamics [1, 2, 4], we again choose the Itô interpretation for convenience. The energy functional includes local potentials $V(\varphi_i)$ and a simple harmonic coupling between sites [1, 4]:

$$\mathcal{F}(\{\varphi\}) = \sum_{i=1}^{N}\left[V(\varphi_i) + \frac{K}{4n}\sum_{\langle ij\rangle}(\varphi_j-\varphi_i)^2\right]. \tag{9.2}$$

Here N is the number of lattice sites and K is the coupling strength. The sum $\sum_{\langle ij\rangle}$ runs over all n sites j coupled to site i. For nearest neighbor coupling $n = 2d$ while for global coupling $n = N-1$. As we have seen, other forms of coupling can also be considered [2] (see Chapter 7) but the structure of the mean field problem, following simplification, remains identical in each case. As such, although the following formalism is presumably

generalizable to the pattern-forming case, we restrict ourselves to the simpler diffusive system given by Eq. (9.2). We have already seen that it is possible to analyze the steady states for these systems analytically within a mean field approximation, and this leads to a Fokker-Planck equation that can be solved in the steady state. As such, we were able to establish the phase diagram detailing the steady state behavior, but we have thus far obtained no dynamical information. In the case of phase transitions to static phases, this does not preclude at least a semi-analytical treatment of the system; however, when phases are time-dependent, the steady state formalism provides insufficient means for any analysis beyond numerical simulation, including the determination of the phase diagram.

The addition of a second field to this problem was introduced in [4] (see Chapter 8), where

$$\begin{aligned} \dot{\varphi}_i &= -\Gamma(\varphi_i)\frac{\delta\mathcal{F}(\{\varphi\})}{\delta\varphi_i} + [\Gamma(\varphi_i)]^{1/2}\xi_i(t) - \omega z_i, \\ \dot{z}_i &= \omega\varphi_i, \end{aligned} \tag{9.3}$$

and ω is a frequency. This system undergoes a noise-induced phase transition to collective oscillatory behavior when the noise exceeds a critical intensity. The mean field Fokker-Planck equation for this two-field system can not be solved analytically because it remains time dependent for all time. While substantial numerical work has been devoted to the problem and a qualitative understanding of the system obtained based on these lattice simulations, no analytical approximations have thus far been given for exploring the dynamics critical to the phase transition.

Since our Gaussian ansatz method relies on the mean field evolution equations, in the next section we briefly reemphasize the conceptual framework for the mean field approximation, whose steady state solution was discussed at length in Chapters 6, 7. We highlight here the role of the time-dependent Fokker-Planck equation and the associated time-dependent probability density function, not merely its steady state form. As such, the problem is easily generalized to include the two degree of freedom case (reminiscent of Chapter 8) and the formulation provides a natural setting for introducing our Gaussian ansatz. Ultimately, this ansatz can be combined with a large coupling approximation to yield information on the dynamics underlying phase transitions in both one and two field systems.

9.3 The mean field and the Gaussian ansatz

In the mean field approximation the sum over neighbors connected to site i in the derivative of the energy functional appearing in Eq. (9.1) or Eq. (9.3),

$$\frac{\delta \mathcal{F}(\varphi_i)}{\delta \varphi_i} = \frac{\partial V(\varphi_i)}{\partial \varphi_i} - K\left(\varphi_i - \frac{1}{n}\sum_{\langle ij \rangle} \varphi_j\right), \tag{9.4}$$

is replaced by the mean field value,

$$\frac{1}{n}\sum_{\langle ij \rangle} \varphi_j(t) \longrightarrow \langle \varphi(t) \rangle \equiv \varphi_0(t). \tag{9.5}$$

Since all the sites are then equivalent, the lattice index can be dropped and the set of field equations reduces to a single equation (one-field system),

$$\dot{\varphi}(t) = a(\varphi; \varphi_0(t)) + [\Gamma(\varphi)]^{\frac{1}{2}}\, \xi(t), \tag{9.6}$$

or to two coupled equations (two-field system),

$$\begin{aligned} \dot{\varphi}(t) &= a(\varphi; \varphi_0(t)) + [\Gamma(\varphi)]^{\frac{1}{2}}\, \xi(t) - \omega z, \\ \dot{z} &= \omega \varphi, \end{aligned} \tag{9.7}$$

where

$$a(\varphi; \varphi_0(t)) \equiv -\Gamma(\varphi)\left\{\frac{\partial V(\varphi)}{\partial \varphi} - K[\varphi_0(t) - \varphi]\right\}. \tag{9.8}$$

The unknown mean field $\varphi_0(t)$ must be determined self-consistently,

$$\varphi_0(t) = \langle \varphi(t) \rangle_\rho. \tag{9.9}$$

Here $\langle \cdot \rangle_\rho$ stands for the statistical average with respect to the probability density ρ associated with Eq. (9.6) or Eq. (9.7).

The Fokker-Planck equation for the probability density $\rho(\varphi, t; \varphi_0(t))$ in the one-field case follows immediately from the Langevin equation (9.6),

$$\frac{\partial}{\partial t}\rho = -\frac{\partial}{\partial \varphi}\left[a(\varphi; \varphi_0(t))\rho\right] + \frac{\sigma^2}{2}\frac{\partial^2}{\partial \varphi^2}\left[\Gamma(\varphi)\rho\right]. \tag{9.10}$$

We explicitly note the dependence of ρ on the unknown mean field $\varphi_0(t)$, which must be determined via Eq. (9.9) using the solution of the Fokker-Planck equation. The time

dependent probability density has not been found analytically. In the stationary state the left side of Eq. (9.10) is set to zero and the equation can be solved, to yield the steady state probability density

$$\begin{aligned} \rho_{\rm st}(\varphi;\varphi_0) &= N(\varphi_0)\Gamma(\varphi)^{-1}e^{-(2/\sigma^2)\left[V(\varphi)+\frac{K}{2}(\varphi_0-\varphi)^2\right]} \\ &= N(\varphi_0)e^{-(2/\sigma^2)V_{eff}(\varphi)}, \end{aligned} \tag{9.11}$$

where

$$V_{eff}(\varphi) \equiv V(\varphi) + \frac{K}{2}(\varphi_0-\varphi)^2 + \frac{\sigma^2}{2}\ln\Gamma(\varphi) \tag{9.12}$$

and $N(\varphi_0)$ is the normalization constant. The mean field φ_0 can then be found from Eq. (9.9), which typically must be solved numerically and provides the phase diagrams shown in previous chapters. A disordered stationary phase is associated with the solution $\varphi_0 = 0$, while a solution $\varphi_0 \neq 0$ corresponds to an ordered stationary phase. The phase boundaries for different forms of $V(\varphi)$ and $\Gamma(\varphi)$ are detailed in [1, 2] for phase transitions to homogeneous and patterned states, respectively, as we saw in Chapters 6 and 7. Note that this procedure leads to a complete mean field stationary state analysis but does not provide information about the dynamics of the approach to the steady state.

For the two-field case the Fokker-Planck equation for the probability density $\rho(\varphi, z, t; \varphi_0(t), z_0(t))$ follows from the Langevin equation (9.7),

$$\begin{aligned} \frac{\partial}{\partial t}\rho &= -\frac{\partial}{\partial\varphi}\left[\left(a(\varphi;\varphi_0(t)) - \omega z\right)\rho\right] \\ &\quad -\omega\varphi\frac{\partial}{\partial z}\rho + \frac{\sigma^2}{2}\frac{\partial^2}{\partial\varphi^2}\left[\Gamma(\varphi)\rho\right]. \end{aligned} \tag{9.13}$$

This equation has not been solved analytically. Furthermore, since we know from numerical simulations (Chapter 8) that the system supports collective oscillations, it is necessary to solve the time-dependent problem even to find the long-time behavior.

To obtain time-dependent solutions to the one-field and two-field models, we will assume a Gaussian form for the evolving probability density with time-dependent parameters to be found self-consistently from the associated Fokker-Planck equation. Thus, for the one-field problem we take

$$\rho(\varphi, t) = e^{A(\varphi-\varphi_0)^2+C}, \tag{9.14}$$

where the time dependent mean field $\varphi_0(t)$ and inverse width parameter $A(t)$ are to be determined. The parameter $C(t)$ is found from the normalization condition

$$\int d\varphi \rho(\varphi) = 1 \tag{9.15}$$

to be given by

$$C(t) = \frac{1}{2} \ln \left(\frac{-A(t)}{\pi} \right). \tag{9.16}$$

It is immediately evident from a comparison of Eqs. (9.14) and (9.11) that (9.14) is at best an approximate solution, but we will subsequently show that for sufficiently strong coupling K this in fact provides an excellent approximation for the mean value and width of the distribution. Note that Eq. (9.11) implies that in the mean field approximation $A = -V''_{eff}(\varphi_0)/\sigma^2$ for the stationary state. For the two-field case we posit the form

$$\rho(\varphi, z, t) = e^{A(\varphi-\varphi_0)^2 + E(\varphi-\varphi_0)(z-z_0) + M(z-z_0)^2 + C}, \tag{9.17}$$

where now $z_0(t)$, $E(t)$ and $M(t)$ are also to be determined. The normalization condition

$$\int d\varphi dz \rho(\varphi, z, t) = 1 \tag{9.18}$$

fixes $C(t)$,

$$C = \frac{1}{2} \ln \left(\frac{4MA - E^2}{4\pi^2} \right). \tag{9.19}$$

Note that the Gaussian only has finite norm for $4MA - E^2 > 0$.

We expect these forms to work best for strong coupling. If coupling is too weak, then there is no transition to collective behavior and a Gaussian ansatz is not appropriate. As coupling becomes extremely strong, the distribution approaches a δ-function. This provides the motivation for a narrow distribution, whose mean and width we assume to be well captured by a Gaussian when coupling is strong. The Gaussian ansatz thus rests on the observation that $\varphi_0(t) \sim z_0(t) \sim A\langle(\delta\varphi)^2\rangle \sim E\langle\delta\varphi\delta z\rangle \sim M\langle(\delta z)^2\rangle \sim O(K^0)$ together with the assumption that the second order moments $\langle(\delta\varphi)^2\rangle \sim \langle(\delta z)^2\rangle \sim O(1/K)$ and the expectation that higher order moments are subleading for large K. Here $\delta\varphi \equiv \varphi - \varphi_0$ and $\delta z \equiv z - z_0$. In the following sections we show that these assumptions lead to consistent results.

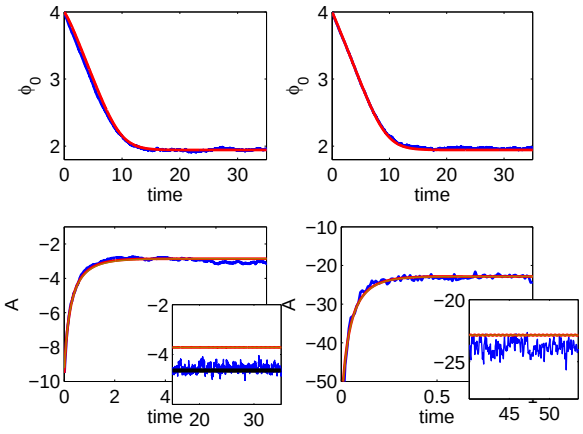

Figure 9.1: The time evolution of φ_0 (top panels) and A (bottom panels), that give the mean and the inverse width of the distribution, is shown for simulations of *globally coupled* arrays of $N = 4000$ sites and compared to the numerical solution of Eqs. (9.20) and (9.21). The left column represents modest coupling, $K = 10$, while the right column shows $K = 80$; $\sigma^2 = 3.5$ for all plots. The initial values $-A(0)$ are chosen to be $\gtrsim K/\sigma^2$; specifically, $A(0) = -9.7$ in the left column and $A(0) = -58$ in the right column. The dark (blue) lines show data from lattice simulations, while the light (red) lines represent theoretical predictions. The very light (brown) curves in the lower right panel and inset represent the uncoupled dynamics given by Eq. (9.23) and the Riccati equation (9.22). The lower left inset shows the simulation results and the prediction of the mean field theory (solid black line) in the stationary state, which is exact when $N \to \infty$. The inset in the bottom right figure shows a close up of the late time evolution. Note the different horizontal and vertical scales in the various panels.

9.4 Single field

We start with Eqs. (9.14) and (9.16), substitute the Gaussian into the Fokker-Planck equation (9.10), and implement a large-K expansion considering the previous comments. We also recognize that the relaxation function and its derivatives, as well as the local potential and its derivatives, are independent of K. The contributions to leading orders in K then result in the set of equations

$$\dot{A} = 2A\Gamma_0(K + \sigma^2 A), \tag{9.20}$$

$$\dot{\varphi}_0 = -\Gamma_0 V_0' - \left(\frac{3\sigma^2}{2} + \frac{K}{A}\right)\Gamma_0', \tag{9.21}$$

For each function $f(\varphi)$ we have adopted the notation $f_0 \equiv f(\varphi_0)$, $f_0' \equiv [df(\varphi)/d\varphi]_{\varphi=\varphi_0}$, etc. Note that it is clear from these two equations that the system evolves towards $A \sim O(K)$ and $\varphi_0 \sim O(1)$. We also point out that the normalization condition (9.16) is consistent with the evolution equation one obtains for $C(t)$, namely, $\dot{C} = \Gamma_0(K + \sigma^2 A)$. The set of equations (9.20) and (9.21) is of course nonlinear and can not be solved exactly, but it is merely a set of two ordinary differential equations whose numerical solution is trivial.

Even so, we can make further analytic progress by noting that for large K, and provided the initial value of A is of (negative) $O(K)$, the evolution of A toward its stationary state is clearly faster than that of φ_0, thus allowing us to consider Γ_0 as nearly constant during the relaxation of A. In this approximation Eq. (9.20) is a Riccati equation with solution

$$A(t) = \frac{-K}{\sigma^2}\frac{1}{1 - \left(1 + \frac{K}{\sigma^2 A(0)}\right)e^{-2\Gamma_0 K t}}. \tag{9.22}$$

After the stationary state for A is reached, the evolution of $\varphi_0(t)$ is governed by

$$\dot{\varphi}_0 = -\Gamma_0 \frac{dV_{eff}(\varphi_0)}{d\varphi_0}. \tag{9.23}$$

Before comparing the results of the theory with those of numerical simulations, we note that in the stationary state where $\dot{A} = \dot{\varphi} = 0$ we find from Eq. (9.20) or Eq. (9.22) that $A = -K/\sigma^2$, and that φ_0 obtained from Eq. (9.21) or (9.23) is the solution of the condition $dV_{eff}(\varphi_0)/d\varphi_0 = 0$. The latter is exactly the mean field solution to the

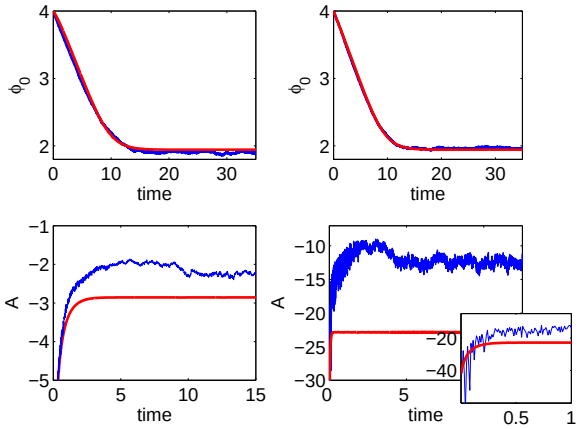

Figure 9.2: The time evolution of the mean (top panels) and inverse width (bottom panels) is shown for simulations of *locally coupled* two-dimensional arrays of $N = 64 \times 64$ sites and compared to the numerical solution of Eqs. (9.20) and (9.21). The left column represents modest coupling, $K = 10$, while the right column shows results for $K = 80$; $\sigma^2 = 3.5$ for all plots. The dark (blue) lines show data from lattice simulations, while the light (red) lines represent theoretical predictions. The initial values are $A(0) = -9.2$ (left column) and -42 (right column). The inset in the bottom right panel shows a close up of the early time evolution.

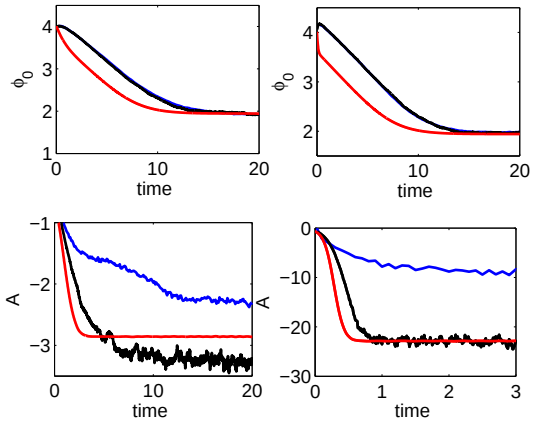

Figure 9.3: The time evolution of the mean field (top panels) and the inverse width of the distribution (bottom panels) is shown for both locally (dark or blue) and globally (black) coupled simulations and compared to the numerical solution (light or red) of the large K theory. Again, the left column is for $K = 10$ and the right for $K = 80$. Here we choose $|A(0)| < 1$ (specifically, $A(0) \sim -0.1$), and the transient dynamics are not well-described for early times. The theory accurately captures the steady-state behavior of the globally coupled simulations in the large K regime. $N = 4000$ (globally coupled) and 64×64 (locally coupled), and $\sigma^2 = 3.5$ for all panels.

problem, which is thus recovered from the Gaussian ansatz. The former differs from the exact inverse width of the distribution (9.11) by contributions of $O(1)$.

However, the ansatz takes us beyond the stationary solution to provide information about the dynamics of the system as it approaches the steady state. In Fig. 9.1 we show four sets of results for the mean field $\varphi_0(t)$ and the inverse width parameter $A(t)$. One is the outcome of the direct simulation of globally coupled arrays for moderate and for strong coupling K. The second is the result of integrating Eqs. (9.20) and (9.21), the third is the outcome of Eqs. (9.22) and (9.23) that assume different relaxation rates, and the fourth is the outcome of the mean field distribution (9.11). In these and all subsequent figures we have made the representative choices

$$V(\varphi) = \frac{\varphi^2}{2}, \quad \Gamma(\varphi) = \frac{1+\varphi^2}{1+\varphi^4}, \tag{9.24}$$

which were also used in our earlier work [1, 2, 4].

The first conclusion is that the time scale of relaxation and the steady state

value of φ_0 are correctly predicted by the large coupling theory, even for modest values of K. The agreement is spectacular during the approach to steady state. In addition, we note that the time scale separation between A and φ_0 is quite evident for large K and is a reasonable assumption also for modest values, $K \approx 10$. Further discussion of the results in this figure requires that we take note of the different horizontal and vertical scales in the different panels. A small but consistent discrepancy between the Gaussian theory results for A and simulation results for the inverse width of the distribution arises at long times owing to neglected higher order contributions in the theory. In the lower left panel we have expanded the vertical scale to make the difference clear, but note that it is extremely small for large K (see lower right inset). The lower left inset confirms that the simulation and mean field theory stationary widths are in fact identical, as they should be for sufficiently large arrays. While we only show results for two values of K and one lattice size, the results for a range of values of K ($K = 20$, 40, 60), of lattice sizes ($N = 250$ up to $N = 16000$), and of initial conditions in which $A(t = 0) \sim -K$ follow the patterns described above. We thus conclude that the Gaussian ansatz theory gives quantitatively excellent results for the evolution of the globally coupled system toward the steady state and for the steady state itself when the coupling is strong and the width of the initial distribution is of the same order as that of the steady state.

Our theory is based on a mean field theory, and so the appropriate comparison with simulations is as we have shown in Fig. 9.1, with a globally coupled array. However, mean field theories are often used to describe locally coupled systems, and so we compare our theoretical results with simulation results in which the units in a two-dimensional array are connected only to their nearest neighbors. The results are shown in Fig. 9.2. The theory accurately captures the behavior of φ_0, including both the transient and steady state dynamics, in the large and modest K regimes. However, the inverse width of the distribution (as given indirectly by A) is underestimated by the theory, as it is by the original mean field theory in this model. A discrepancy of this sort is a ubiquitous feature of mean field theories, which are principally designed to capture the mean field value.

The comparisons so far have relied on the initial value $A(t = 0)$ being of (negative) $O(K)$, that is, an initial distribution whose width is of the same order as that of the steady state. When the initial width of the distribution is much larger than that of

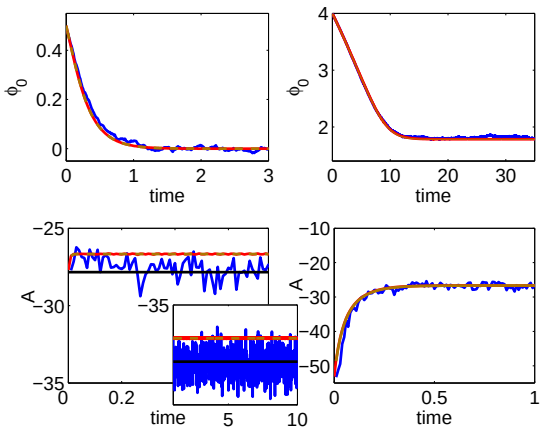

Figure 9.4: Multistability is captured by the large K theory. The left panel shows the dynamics of the mean field and the inverse width of the distribution for initial conditions leading to a disordered state ($\varphi_0(0) \approx 0.5$, $A(0) = -29$). The right panel shows the corresponding plots for initial conditions leading to an ordered phase ($\varphi_0(0) \approx 4$, $A(0) = -55$). The inset in the bottom left shows a close up of the steady state behavior. Dark (blue): globally coupled simulations; light (brown): Gaussian ansatz theory; black: mean field theory. In all plots, $K = 80$, $\sigma^2 = 3.0$.

the steady state, i.e., when $A(t = 0)$ is very different from (much smaller in magnitude than) K, it becomes more problematic to capture the transient dynamics, although the steady state behavior is still predicted accurately. This is shown in Fig. 9.3.

Finally and importantly, we note that the large coupling theory accurately captures the multistable nature of the dynamics (Fig. 9.4). This is a new feature of this theory that provides dynamical information not provided by the usual mean field theory. In our earlier work we had established this multistability only through direct numerical simulations of the array. For large K, the agreement between theory and simulations both in the dynamical regime and in the steady state is quite remarkable for initial conditions leading to the ordered state (right panel). While the mean field theory of course predicts the width of the distribution exactly, the Gaussian ansatz slightly overestimates the width for initial conditions leading to a disordered phase (left panel). The disordered state is marked by a relatively broad distribution, and, not surprisingly, given the underlying requirements stated earlier, the theory does not exactly capture this prediction.

9.5 Two fields

The more stringent test of the theory lies in the two-field system, where there are only numerical simulation results. Now we begin with Eqs. (9.17) and (9.19), substitute the assumed distribution into the two-variable Fokker-Planck equation (9.13), and again implement a large-K expansion. This results in the set of equations for the coefficients in the Gaussian,

$$\begin{aligned} \dot{A} &= 2A\Gamma_0(K+\sigma^2 A), \\ \dot{M} &= \left(\frac{\sigma^2}{2}\Gamma_0 E+\omega\right)E, \\ \dot{E} &= \Gamma_0(K+2\sigma^2 A)E+2\omega(A-M), \end{aligned} \tag{9.25}$$

along with those for the mean values

$$\begin{aligned} \dot{\varphi}_0 &= -\Gamma_0 V_0' - \left(\frac{3\sigma^2}{2}+\frac{K}{A}\right)\Gamma_0' - \omega z_0, \\ \dot{z}_0 &= \omega\varphi_0. \end{aligned} \tag{9.26}$$

Again, it is easy to ascertain that the normalization condition (9.19) is consistent with the evolution equation obtained for $C(t)$.

The solution we are interested in is a collective oscillatory mode, which of course requires the time-dependent solution of the coupled sets of ordinary differential equations (9.25) and (9.26), a task which is vastly simpler than the solution of the time-dependent Fokker-Planck equation. However, as in the single field case, we can further simplify the problem of finding the oscillatory long-time behavior of the mean values φ_0 and z_0 by exploring the regime where the coefficients A, M, and E have reached a steady state, that is, by setting the left hand sides in Eq. (9.25) equal to zero. There are two stationary solutions, one of which is

$$A=\frac{-K}{\sigma^2}, \quad E=0, \quad M=A. \tag{9.27}$$

The other solutions, $(A,\, E,\, M) = (0,\, 0,\, 0)$, $(A,\, E,\, M) = (-K/\sigma^2,\, -2\omega/(\sigma^2\Gamma_0),\, 0)$, and $(A,\, E,\, M) = (0,\, -2\omega/(\sigma^2\Gamma_0),\, -K/\sigma^2)$ do not satisfy the condition $4MA - E^2 > 0$ necessary for proper normalization, cf. Eq. (9.19), and are hence unphysical.

For the long-time behavior, it now remains to substitute the stationary A into Eq. (9.26) and solve the coupled set of just two equations,

$$\begin{aligned} \dot{\varphi}_0 &= -\Gamma_0 \frac{dV_{eff}(\varphi_0)}{d\varphi_0} - \omega z_0, \\ \dot{z}_0 &= \omega \varphi_0. \end{aligned} \tag{9.28}$$

We note that this set has two stationary solutions, the disordered state $(\varphi_0, z_0) = (0, 0)$, and another solution, $(\varphi_0, z_0) = (0, -\Gamma_0 V'_{eff}(0)/\omega)$. This second solution is easily seen to be unstable. We can go even further toward the analytic oscillatory solution by implementing a multiscale perturbation theory [6]. For this purpose we combine (9.26) into a single second-order differential equation,

$$\begin{aligned} \ddot{z} + \omega^2 z &= \omega G(\varphi), \\ G(\varphi) &= -\Gamma(\varphi) \frac{dV_{eff}(\varphi)}{d\varphi}, \end{aligned} \tag{9.29}$$

with $\varphi \equiv \dot{z}/\omega$. It is understood that the variables are the mean fields and should therefore carry the 0 subscript, which we have omitted for economy of notation. We treat G as a perturbation and write

$$\ddot{z} + \omega^2 z = \epsilon \omega G(\dot{z}/w), \tag{9.30}$$

where ϵ is a small parameter. The solution is then expressed in terms of different time scales, $(T_0, T_1, \dots)$,

$$z(t) = Z(T_0, T_1, \cdots) = Z_0(T_0, T_1) + \epsilon Z_1(T_0, T_1) + O(\epsilon^2), \tag{9.31}$$

where $T_n \sim O(\epsilon^n T_0)$. For the time derivatives we have

$$\begin{aligned} \frac{dz}{dt} &= \frac{\partial Z}{\partial T_0} + \epsilon \frac{\partial Z}{\partial T_1} = \frac{\partial Z_0}{\partial T_0} + O(\epsilon), \\ \frac{d^2 z}{dt^2} &= \frac{\partial^2 Z}{\partial T_0^2} + \epsilon \frac{\partial^2 Z}{\partial T_0 \partial T_1} + O(\epsilon^2) \\ &= \frac{\partial^2 Z_0}{\partial T_0^2} + \epsilon \frac{\partial^2 Z_1}{\partial T_0^2} + \epsilon \frac{\partial^2 Z_0}{\partial T_0 \partial T_1} + O(\epsilon^2) \end{aligned} \tag{9.32}$$

The evolution equation at zero order in ϵ is

$$\frac{\partial^2 Z_0}{\partial T_0^2} + \omega^2 Z_0 = 0, \tag{9.33}$$

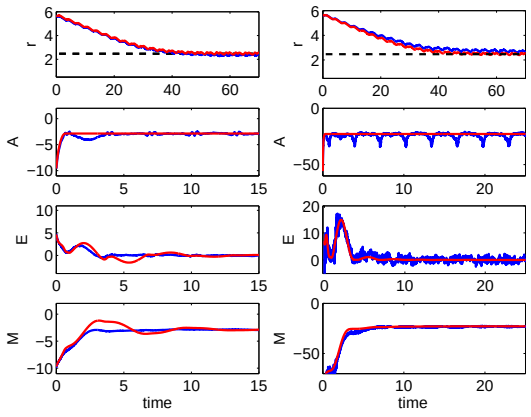

Figure 9.5: The time evolution of the limit cycle radius, r (top panels) and of the Gaussian ansatz coefficients (three subsequent panels). The dark (blue) curves are appropriate moment results from simulations of globally coupled arrays ($N = 4000$ sites), and the light (red) curves are obtained from the solution of Eqs. (9.25) and (9.26). $K = 10$ in the left column and $K = 80$ in the right column. Initial values for left column: $(A, E, M) = (-9.6, 4.7, -9.7)$; right column: $(A, E, M) = (-56, 7, -79)$. The noise intensity $\sigma^2 = 3.5$ in all panels. The dashed line in the top panels is the steady state radius predicted by multiscale analysis.

which has a solution

$$Z_0(T_0, T_1) = R(T_1)\cos(\omega T_0) + S(T_1)\sin(\omega T_0). \tag{9.34}$$

The coefficients $R(T_1)$ and $S(T_1)$ are determined by considering the evolution equations at first order in ϵ,

$$\frac{\partial^2 Z_1}{\partial T_0^2} + Z_1 = -\frac{\partial^2 Z_0}{\partial T_0 \partial T_1} + \omega\, G\left(\frac{1}{\omega}\frac{\partial Z_0}{\partial T_0}\right). \tag{9.35}$$

As always in multiscale perturbation theory, in order to avoid secular terms in the solution R and S must be chosen in such a way that resonant terms do not appear in the right hand side of Eq. (9.35), i.e.,

$$\begin{aligned}
\int_{-\infty}^{\infty} dT_0\, \cos(\omega T_0)\left[-\frac{\partial^2 Z_0}{\partial T_0 \partial T_1} + \omega\, G\left(\frac{1}{\omega}\frac{\partial Z_0}{\partial T_0}\right)\right] = 0, \\
\int_{-\infty}^{\infty} dT_0\, \sin(\omega T_0)\left[-\frac{\partial^2 Z_0}{\partial T_0 \partial T_1} + \omega\, G\left(\frac{1}{\omega}\frac{\partial Z_0}{\partial T_0}\right)\right] = 0,
\end{aligned} \tag{9.36}$$

where from (9.34) it follows that

$$\frac{\partial^2 Z_0}{\partial T_0 \partial T_1} = -\frac{\partial R}{\partial T_1}\,\omega\sin(\omega T_0) + \frac{\partial S}{\partial T_1}\,\omega\cos(\omega T_0). \tag{9.37}$$

This immediately leads to the equations for R and S,

$$\begin{aligned}
\frac{\partial R}{\partial T_1} &= -\frac{\int_{-\infty}^{\infty} dT_0\, \sin(\omega T_0) G\left(\frac{1}{\omega}\frac{\partial Z_0}{\partial T_0}\right)}{\int_{-\infty}^{\infty} dT_0\, \sin^2(\omega T_0)}, \\
\frac{\partial S}{\partial T_1} &= \frac{\int_{-\infty}^{\infty} dT_0\, \cos(\omega T_0) G\left(\frac{1}{\omega}\frac{\partial Z_0}{\partial T_0}\right)}{\int_{-\infty}^{\infty} dT_0\, \cos^2(\omega T_0)}.
\end{aligned} \tag{9.38}$$

The quotients can be computed by introducing a cutoff Λ in the integrals, $\int_{-\Lambda}^{\Lambda} dT_0 \cdots$, and subsequently taking the limit $\Lambda \to \infty$.

We thus have theoretical predictions at three levels of approximation. The most detailed is the five-equation set (9.25) and (9.26). This set of equations contains the dynamical approach to the long time behavior. The second level is contained in Eqs. (9.27) and (9.28). This yields the long-time oscillatory behavior of the mean field and the width parameters of the distribution at long times. Finally, Eq. (9.27) together

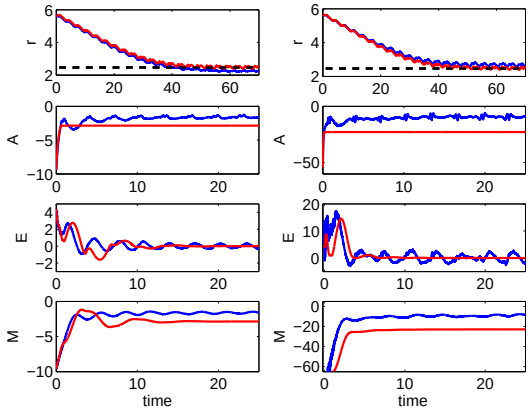

Figure 9.6: Same as Fig. 9.5, but now the simulations are for locally coupled arrays. Initial values for left column: $(A, E, M) = (-9.4, 4.4, -9.6)$; right column: $(A, E, M) = (-55, 5, -76)$.

with (9.35) and (9.38) (along with the second equation in (9.26)) provide a full long-time solution in terms of quadrature. Note that this explicit solution presents a circular limit cycle of the form $z = S_0 \sin(\omega t)$ with S_0 constant [$Z_0 = S_0 \sin(\omega T_0)$], provided we have $\partial R/\partial T_1 = 0$ [directly satisfied for the choice in (9.24)] and $\partial S/\partial T_1 = 0$, i.e., if

$$0 = I(S_0) = \int_{-\infty}^{\infty} dT_0 \, \cos(\omega T_0)\, G(S_0 \cos(\omega T_0)). \tag{9.39}$$

Since our numerical simulations [4] indicate an essentially circular limit cycle near the onset of multistability, we expect that Eq. (9.39) may provide an accurate prediction of the onset in the strong coupling limit.

We now proceed to test our multi-level theoretical predictions against direct numerical simulations of the array. Again, we adopt the representative choices (9.24) for the potential and relaxational functions. We concentrate on the multistability onset regime by fixing the value of the noise intensity appropriately.

Figure 9.5 compares the results of simulations for globally coupled arrays with those of our theory. The agreement is clearly excellent for the limit cycle radius as well as the width parameters for all times. The time scale separation required for the validity of the large K equations is clearly satisfied for $K \sim 80$ and even for modest values, $K \sim 10$. Note that the width parameters reach the steady state very quickly

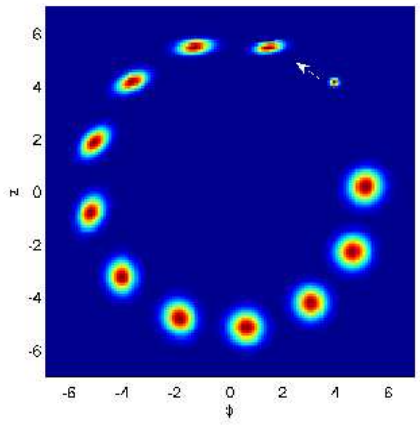

Figure 9.7: Evolution of the theoretical probability distribution function as obtained by substituting the numerical solution of Eqs. (9.25) and (9.26) into Eq. (9.17). The distribution becomes symmetrical (circular) in φ_0 and z_0 prior to reaching its steady state radius. The evolution is only shown for the short time leading up to relaxation of the distribution shape. Over longer times, the distribution will continue a circular trajectory whose radius eventually reaches its steady state value (see Fig. 9.8). $K = 10$ and $\sigma^2 = 3.5$.

even when E is initially chosen to be of $O(K)$. The theory very slightly overestimates the steady state radius $r \equiv \sqrt{\dot{z}^2/(2\omega^2) + z^2/2}$ for modest $K = 10$, and very slightly underestimates the radius for large $K = 80$ (neither visible on the scale of the figures). Again as expected, the agreement with the simulations for the locally coupled array is less spectacular (Fig. 9.6), but the limit cycle radius is still captured very accurately for all times. For visualization purposes, we also show the early time evolution of the theoretical probability distribution function in Fig. 9.7.

Figure 9.8 confirms that the phase portrait of the limit cycle from the globally coupled lattice simulations corresponds reasonably well to that predicted by the large K equations, and that the frequency of the oscillations is also accurately predicted. The dynamic evolutions of the simulation and of the theory do not match exactly because the small error in the frequency implies an increasing dephasing with time. The figure shows the case $K = 80$, but the results are only representative, and again the theory holds well even for more modest values of K and for a range of initial conditions leading to limit cycle behavior.

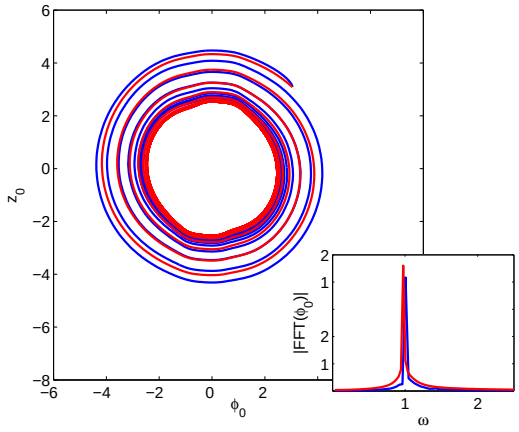

Figure 9.8: The phase space portraits of lattice simulations (dark or blue) and the large K equations (9.25) and (9.26) (light or red) show good agreement in terms of the steady state limit cycle radius, though the theory slights underestimates r. Inset: oscillation frequency. $K = 80$, $\sigma^2 = 3.5$, and $\omega = 1$.

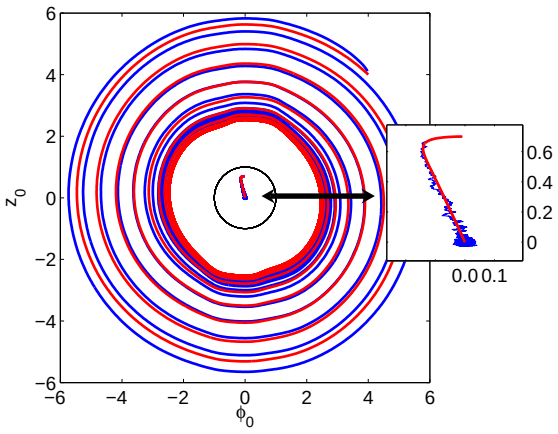

Figure 9.9: Comparison of the phase space portraits of lattice simulations (dark or blue) and the large K equations (light or red) show that the latter correctly predict multistable behavior. The right inset shows a close up of the indicated portion of the phase portrait. The black curve is the unstable limit cycle obtained from the multiscale analysis. $K = 80$, $\sigma^2 = 3.5$, and $\omega = 1$.

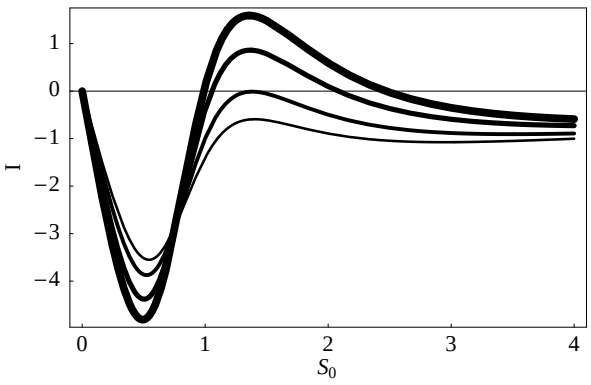

Figure 9.10: The multiscale analysis predicts the onset of bistability to occur at $\sigma^2 \approx 2.4$. Curves are, from thickest to thinnest, $\sigma^2 = 3.5$, 3.0, 2.4, 2.0.

Finally, as in the single field problem, the large coupling theory predicts the occurrence of multistable regions in parameter space. In our earlier work [4] we noted the expectation of multistability, but did not explicitly pursue it in our simulations, nor did we have a predictive theory as we now do. In Fig. 9.9 we show that the multistable nature of the phase transition is fully captured by the large coupling theory. In particular, different initial conditions lead to either a disordered phase or a limit cycle. To test whether the theory correctly predicts the onset of multistability is more cumbersome, but we can at least do it easily in the multiscaling (large K) regime on the basis of Eq. (9.39). The value of the noise for onset of multistability in general depends on coupling strength [1, 4], but this dependence greatly weakens with increasing K. For example, our simulation results indicate that at $K = 10$ multistability first occurs at roughly $\sigma^2 \approx 3$, with the noise value decreasing ever more slowly with increasing K (e.g., $\sigma^2 \approx 2.6$ for $K = 20$, $\sigma^2 \approx 2.5$ for $K = 40$). At $K = 80$ the transition occurs at $\sigma^2 \approx 2.4$. Equation (9.39) is in fact independent of K. The function $I(S_0)$ is shown explicitly in Fig. 9.10. The first zero is the disordered state and the second first appears when $\sigma^2 = 2.4$. As noise increases, an intermediate unstable solution also appears, illustrated explicitly in Fig. 9.9. The multiscaling result thus accurately predicts not only the radius $r = S_0$ of the limit cycle but the noise for onset of multistability when coupling is strong, and the increase in the limit cycle radius with increasing noise strength.

9.6 Discussion

We have presented an analytical theory for the dynamics of relaxational systems with field dependent coefficients. Based on a Gaussian ansatz and an expansion about the mean field values, we derive ordinary differential equations detailing the time evolution of the field distribution means and widths. In the limit of large coupling, the Gaussian ansatz equations provide a consistent, normalized approximation of the relevant probability distributions which agrees with numerical lattice simulations. In particular, our method allows us to study the dynamics of both one- and two-field relaxational systems, including those with oscillatory collective states previously beyond the reach of the static mean field theories. This also provides an analytic access to initial-condition-dependent multistable regimes for noise-induced phase transitions in spatially extended systems.

Acknowledgments

Chapter 9 contains material which appears, in part, in F. Cao, K. Wood, and K. Lindenberg, (2007).

References

[1] J. Buceta and K. Lindenberg, Phys. Rev. E **69**, 011102 (2004).

[2] K. Wood, J. Buceta, and K. Lindenberg, Phys. Rev. E **73**, 022101 (2006).

[3] R. Kawai, X. Sailer, L. Schimansky-Geier, and C. Van den Broeck, Phys. Rev. E **69**, 051104 (2004).

[4] J. Buceta, K. Wood, and K. Lindenberg, Phys. Rev. E **73**, 042101 (2006).

[5] S. Habib, Y. Kluger, E. Mottola, and J.P. Paz, Phys. Rev. Lett. **76**, 4660 (1996); F. J. Cao and H. J. de Vega, Phys. Rev. D **63**, 045021 (2001); D. Boyanovsky, F.J. Cao, and H. J. de Vega, Nucl. Phys. B **632**, 121 (2002); F. J. Cao and H. J. de Vega, Phys. Rev. D **65**, 045012 (2002).

[6] L-Y. Chen, N. Goldenfeld, and Y. Oono, Phys. Rev. E **54**, 376 (1996).

10

Conclusion

We have seen that macroscopic cooperation arises in a number of inherently nonequilibrium settings. While it is clear that a myriad of physical systems consist of entities whose dynamics range from largely independent to strikingly collective, the mechanisms dictating such behavior can be quite distinct. In Part I, we explored time-dependent synchronization in populations of phase-coupled, discrete oscillators and observed the competing roles of statistical disorder (both quenched and time-dependent) and coupling strength in dictating the dominant macroscopic behavior of the system. By contrast, Part II provided a detailed analysis of systems exhibiting macroscopic ordering facilitated entirely by the constructive interplay between coupling and noise. It is exactly this diversity–and perhaps also the counterintuitive behavior commonplace in these systems–which assures the continued interest of the physics community in nonequilibrium phase transitions. Combined with the tremendous natural ubiquity of large scale cooperativity–particularly that arising away from equilibrium–these findings underscore the importance and utility of simple models in reproducing and understanding the highly complex behavior arising in systems with many degrees of freedom.